

PARTICLE ENGINEERING FOR HIGH DOSE DRY POWDER
INHALATION OF ITRACONAZOLE

Dissertation
zur
Erlangung des Doktorgrades (Dr. rer. nat.)
der
Mathematisch-Naturwissenschaftlichen Fakultät
der
Rheinischen Friedrich-Wilhelms-Universität Bonn

vorgelegt von
Ann-Cathrin Willmann
aus
Osnabrück

Bonn, 2022

Angefertigt mit Genehmigung der Mathematisch-Naturwissenschaftlichen Fakultät der
Rheinischen Friedrich-Wilhelms-Universität Bonn

Gutachter: Prof. Dr. Karl G. Wagner

Gutachter: PD Dr. Herbert Wachtel

Tag der Promotion: 08.11.2022

Erscheinungsjahr: 2022

Für meine Familie

Parts of this work have been published elsewhere:

Willmann, A.-C.; Boeck, G.; Wachtel, H.; Berkenfeld, K.; Wagner, K. G.

Particle engineering of itraconazole by spray drying of nanosuspensions for high dose dry powder inhalation

Poster presentation

13th Worldmeeting on Pharmaceutics, Biopharmaceutics and Pharmaceutical Technology 2022,
Rotterdam, The Netherlands

Willmann, A.-C.; Berkenfeld, K.; Faber, T.; Wachtel, H.; Boeck, G.; Wagner, K. G.

Itraconazole nanosuspensions via dual centrifugation media milling: impact of formulation and process parameters on particle size and solid-state conversion as well as storage stability

Pharmaceutics 2022, 14(8), 1528; <https://doi.org/10.3390/pharmaceutics14081528>

Table of contents

1	Introduction and Background.....	1
1.1	Introduction.....	1
1.2	Theoretical background.....	3
1.2.1	Respiratory tract.....	3
1.2.2	Lung deposition.....	4
1.2.3	Dry powder inhalation.....	6
1.2.3.1	Devices.....	6
1.2.3.2	Particle interactions.....	8
1.2.4	Nanoization.....	9
1.2.5	Spray drying.....	10
1.3	Objectives.....	14
2	Material and methods.....	15
2.1	Materials.....	15
2.1.1	Devices.....	15
2.1.1.1	HandiHaler®.....	15
2.1.1.2	GyroHaler®.....	16
2.2	Methods.....	17
2.2.1	Manufacturing processes.....	17
2.2.1.1	Jet-milling.....	17
2.2.1.2	Suspension preparation.....	17
2.2.1.3	Nano milling.....	18
2.2.1.4	Spray drying.....	20
2.2.1.5	Filling of dry powders.....	21
2.2.2	Analytical methods.....	23
2.2.2.1	Dynamic light scattering (DLS).....	23

2.2.2.2	Zeta potential	23
2.2.2.3	X-ray powder diffraction (XRPD).....	23
2.2.2.4	Differential scanning calorimetry (DSC)	24
2.2.2.5	Determination of ITZ assay	24
2.2.2.6	Saturation solubility	24
2.2.2.7	Loss on drying (LoD).....	25
2.2.2.8	Laser diffraction	25
2.2.2.9	Densities	26
2.2.2.9.1	Particle density	26
2.2.2.9.2	Bulk and tapped density.....	26
2.2.2.10	SEM images	27
2.2.2.11	Dynamic vapor sorption (DVS).....	27
2.2.2.12	Reconstitution of the nanoparticles.....	27
2.2.2.13	Aerosol analysis	27
2.2.3	Statistics & Data visualization.....	30
3	Results & Discussion.....	31
3.1	Nanoization of ITZ [83].....	31
3.1.1	Stabilizer assessment	32
3.1.2	Evaluation of process parameters	34
3.1.2.1	Influence of milling temperature	35
3.1.2.2	Influence of milling speed	35
3.1.2.3	Influence of bead size	36
3.1.3	Impact of stabilizer concentration on critical material attributes	40
3.1.3.1	Particle size, zeta potential, PDI.....	40
3.1.3.2	Solid-state	42
3.1.3.3	Morphology	47
3.1.3.4	Storage stability.....	48

3.1.4	Conclusion of the nanoization of ITZ.....	54
3.2	Spray drying process.....	56
3.2.1	Process development.....	56
3.2.1.1	Impact of nozzle flow and feed rate on droplet size	57
3.2.1.2	Properties of spray dried MAN particles.....	59
3.2.1.3	Influence of outlet temperature and stabilizers on modification and morphology of mannitol.....	61
3.2.1.4	Dispersibility of MAN particles by pressure titration	64
3.2.2	Manufacturing of nano-in-microparticles.....	66
3.2.2.1	Physicochemical characterization.....	68
3.2.2.2	Solid-state analysis.....	71
3.2.2.3	Impact of relative humidity on solid-state stability	73
3.2.2.4	Dispersibility of ITZ dry powder particles by pressure titration	76
3.2.2.5	Reconstitution of spray dried nanoparticles in water	78
3.2.3	Conclusion of the spray drying process.....	80
3.3	In-vitro aerodynamic assessment	82
3.3.1	Filling of nano-in-microparticles into primary packaging materials.....	82
3.3.2	Overview of cascade experiments and impact of inhalation device.....	84
3.3.3	Impact of nanoization	92
3.3.4	Impact of ITZ:MAN ratio	93
3.3.5	Conclusion.....	94
4	Overall conclusion.....	96
5	Outlook	98
6	Summary.....	100
7	References.....	103
8	Appendix	116
8.1	Additional figures.....	116

Table of contents

8.2	List of Abbreviations and Acronyms	117
8.3	List of Figures.....	121
8.4	List of Tables.....	126
9	Acknowledgements.....	128

1 Introduction and Background

1.1 Introduction

Over one billion people suffer from fungal infections of the respiratory tract. These pathogens are the reason for more than 1.5 million deaths per year worldwide [1,2]. Most people who suffer from fungal infections of the respiratory tract are immunocompromised (such as HIV patients) or co-morbid with lung diseases such as tuberculosis or cystic fibrosis [3,4]. These patients often show infections of their respiratory tract caused by e.g., *Aspergillus* spp. Infections with *Aspergillus* may manifest differently, depending on the immune status of the patients [1,5]. A hypersensitivity reaction causes allergic bronchopulmonary aspergillosis (ABPA), whereas *Aspergillus* can also lead to life-threatening invasive pulmonary aspergillosis (IPA) [1,2]. The conidia of the fungal species have a particle size of 2-5 μm and are described to be able to reach the alveoli [6]. Itraconazole (ITZ) is considered as first-line therapy against ABPA and also used against IPA [6,7]. To date, only systemic treatments with ITZ exist, which are either orally or intravenously administered. This treatment is often associated with tolerability and safety issues such as side effects, high pharmacokinetic variability, or drug-drug interactions [6]. Therefore, local treatment of these infections is regarded beneficial as it might reduce systemic side effects and other issues. One pulmonary ITZ formulation has been in clinical development (Pulmazole® by Pulmatrix against ABPA), but phase II has been discontinued due to Covid-19 [6].

As for many infectious diseases, medication with ITZ demands significantly higher doses compared to those applied in asthma or COPD therapy. As there is no clear definition of “high-dose” for respiratory treatment, it was suggested by Sibum et al. (2018) that an inhaled dose of more than 2.5 mg active pharmaceutical ingredient (API) is considered as high-dose [8]. Drug delivery to the lower respiratory tract is conducted with devices for aerosolization such as pressurized metered dose inhalers (pMDIs), nebulizers or dry powder inhalers (DPIs). The focus will be on the DPI here as pMDIs are not able to deliver high doses and nebulizers often require extensive inhalation times [9]. High doses cannot be achieved by conventional powder formulations as they usually have very low drug loads (typically up to 2% [9]) and use coarse carrier excipients to facilitate the airborne release of the micronized API. In conventional dry powder formulations, the micronized API is typically formulated with so-called coarse carrier particles (e.g., lactose) to enable sufficient flowability and dispersibility. Carrier-based formulations show several disadvantages considering the dose limitation as the most important one. In order to achieve a high dose with a carrier-based formulation

a large amount of powder would need to be inhaled because of the low drug loading. However, there is an upper limit, as high amounts of inhaled powder can cause local tolerability issues (e.g., coughing) [9].

Therefore, particle engineering with the aim of developing a carrier-free, high dose powder formulation with excellent dispersibility is required [10]. Over the last years, particle engineering has gained increasing interest with some marketed high dose formulations such as Exubera® (insulin for systemic delivery, discontinued), TOBI® Podhaler® (tobramycin against infections with *Pseudomonas aeruginosa*), Bronchitol® (mannitol for cystic fibrosis patients) or Colobreathe® (colistin against infections with *Pseudomonas aeruginosa*) [11]. Various techniques can be applied for particle engineering, for instance nanoization, spray drying, freeze drying, high-pressure homogenization or 3D-printing. Several authors have already published exhaustive reviews [11–16], so only some of these techniques will be presented in more detail. The Pulmosphere® technique enables the production of sponge-like, light porous, ultra-low-density particles with small diameters (< 5 µm), so-called small porous particles [17]. An emulsion-based spray drying process is used for Tobramycin. A phospholipid is dispersed with perflubron in water to obtain an emulsion. The API is added to the water phase (together with stabilizers) and the emulsion is spray dried. Perflubron forms pores in the particles during evaporation [17]. This technique is used for the TOBI® Podhaler®. The so-called Technosphere® technology utilizes fumaryl diketopiperazine in solution together with the API for the production of self-assembling particles, which are later freeze-dried [18]. This technique has been used for the production of Afrezza®, another inhalable insulin. Certain engineered particles, despite having a high geometric diameter, exhibit a small aerodynamic diameter due to a low density (so-called large porous particles) [19–21]. The production of those particles with a very low density can easily be facilitated through spray drying as this process allows the combined control of the particle morphology and density. In general, spray drying provides a huge potential for particle engineering. Most of the marketed high dose formulations are produced by spray drying such as the previously mentioned TOBI® Podhaler®, Bronchitol® and Colobreathe® [11].

Another particle-engineering approach are nanoparticles. Nanoparticles enable the delivery of high doses and might improve bioavailability, however, they are extremely cohesive due to their unfavorable mass/surface ratio [22]. To transfer nanoparticles into a suitable particle size for inhalation, spray drying is the method of choice as spherical particles with tailored sizes and morphologies can be obtained [23]. There are several nanoization techniques, such as precipitation, bead milling or

high-pressure homogenization, which produce amorphous or crystalline API nanoparticles. Poorly soluble compounds like ITZ are well suited for the production of nanocrystals (nanosuspensions containing crystalline API, usually obtained by media milling or high-pressure homogenization). The combination of spray drying nanocrystals, to obtain so-called nano-in-microparticles (see Figure 1), provides several advantages: The API remains crystalline hence solid-state stability is expected to be high. As mentioned above, spray drying enables the manufacturing of tailored spherical particles with low density in a desired particle size range and with a defined surface structure.



Figure 1: Schematic illustration of examples of (engineered) dry powder particles. ■ API, ■ matrix former

Furthermore, organic solvents will be avoided as aqueous systems can be used for ITZ. The approach of using bead milling to obtain crystalline ITZ nanoparticles followed by spray drying for the generation of well dispersible dry powder particles is therefore considered as valid approach for high dose delivery of ITZ and is investigated in this study.

1.2 Theoretical background

1.2.1 Respiratory tract

The main function of the respiratory system is the gas exchange meaning supply of oxygen and removal of carbon dioxide. The respiratory tract can be divided into two parts: the upper respiratory tract (comprising nasal cavity, pharynx, and larynx) and the lower respiratory tract with trachea, bronchi, and alveoli [24]. A schematic illustration is given in Figure 2.

The airways are often described as respiratory tree with the trachea being the tree trunk: The trachea divides into the primary bronchi which each subdivides into two other branches (also called generation) and so on. It is proposed that the respiratory tract consists of 24 airway generations in total [25].

After inhalation and deposition, inhaled particles will either dissolve in the lining fluid followed by cellular uptake or will be cleared via various mechanisms. The epithelium of the upper airways is

covered by mucus secreting cells. Together with ciliated cells, the mucus forms the so-called mucociliary transport, which is the main clearance mechanism in the trachea and bronchi [24,26]. The alveoli are coated with a surfactant layer and clearance is mainly mediated by macrophages [24,26] there.

1.2.2 Lung deposition

The effectiveness of the inhalation therapy depends on the successful deposition of the aerosol particles in the target respiratory region, which is a complex interaction between the lung anatomy and physiology, the inhalation device, the formulation of the API and other factors [24]. Only particles with a specific aerodynamic size, (i.e., the aerodynamic diameter), will be effectively deposited in the respiratory tract. The aerodynamic diameter is directly related to the particle density, shape and the geometric diameter and is defined as the diameter of a sphere with unit density that has the same settling velocity as the relevant particle [27]. It can be calculated as follows:

$$d_{ae} = \sqrt{\frac{\rho_p}{\rho^* \cdot \chi}} * d_g \quad \text{Eq. (1)}$$

With ρ_p being the particle density [g/cm^3], ρ^* being the density of a reference particle with $1 \text{ g}/\text{cm}^3$, χ being the dynamic shape factor with 1 for spheres [-] and d_g being the geometric diameter [μm].

The particle density has only a minor impact, but it is of importance if the density is significantly low (so-called "large porous particles") [16,28]. In general, particles with an aerodynamic diameter between 1-5 μm are regarded as suitable to reach the lower respiratory tract [29]. However, different aerodynamic diameters may be required to target different areas in the respiratory tract. For example, API particles with an intended systemic exposure via the lung should be small to reach the alveoli (due to the large surface area), whereas APIs for the treatment of e.g., asthma would need a larger aerodynamic diameter to target the bronchi and bronchioles [30].

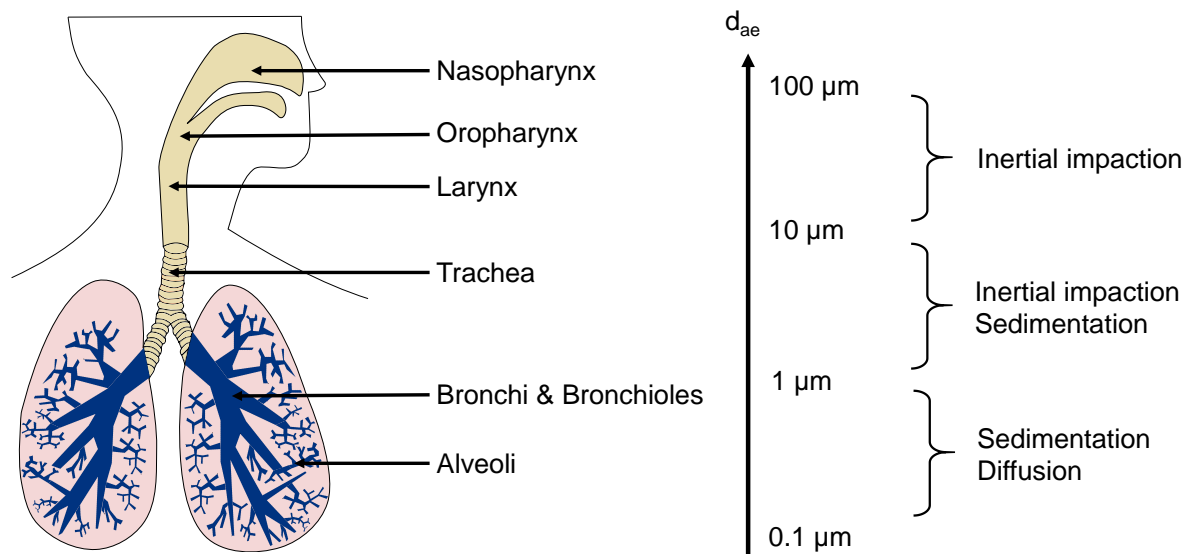


Figure 2: Schematic illustration of the respiratory tract, the aerodynamic diameters (d_{ae}) and the related main impaction mechanisms. Modified from [30].

The deposition of aerosol particles in the respiratory tract is mainly governed by five mechanisms [25]:

- inertial impaction
- sedimentation
- diffusion
- interception
- electrostatic precipitation

The first three mechanisms are the most important ones [31]. During the inhalation process the air (and the aerosol particles) undergo a series of direction changes. *Inertial impaction* is the phenomenon of particles exhibiting a high velocity and not being able to follow the direction of the airstream due to inertia. The particles will impact on the airway walls and deposit there. This mechanism is prevalent in the upper respiratory tract, where the air velocity is high, and the flow is turbulent [24]. *Sedimentation* occurs mostly in the smaller airways and the alveolar region, where flow velocities are low [31]. The aerosol particles undergo sedimentation due to gravitational forces. Brownian motion is the reason for the *diffusion* process of submicron particles (typically below 0.5 μm). Brownian motion is dependent on the particle size and the airflow velocity and increases with decreasing size and airflow rate. The airway conditions that promote sedimentation also promote diffusion [31]. *Interception* comes into play for particles with a high aspect ratio (elongated shape like fibers). These particles do not deviate from their airstream and deposit as soon as they have

contact with the airway wall. Due to their low aerodynamic diameter, they usually impact in the lower airways [24]. A charged particle can induce an opposite charge in the airway walls and can become electrostatically attracted (*electrostatic precipitation*) [25].

These mechanisms often occur simultaneously, depending on the aerodynamic particle size (see Figure 2).

1.2.3 Dry powder inhalation

Respiratory drug delivery to the lung as a dry powder formulation provides several advantages but also challenges [32]. Dry powders show a high chemical stability compared to liquid formulations (e.g., such as formulations to be nebulized). Furthermore, DPIs are portable and require only short administration times compared to nebulizers [9]. There is no synchronization of inhalation maneuver and inspiration required as the so-called passive devices enable aerosolization of the formulation by the patient's airflow [18]. The last aspect can also be challenging as there may be high variabilities between the patients' inspiratory flow rates. As DPIs show a specific airflow resistance, the generation of the required flow rate could be challenging, especially for patients with obstructive diseases.

1.2.3.1 Devices

Nearly all currently marketed DPIs rely on the patient's airflow to deagglomerate the formulation (so-called *passive* devices) [33]. Some devices, which actively de-agglomerate the formulation (so-called *active* devices), are under development but not yet marketed or have been discontinued [14]. An exception is the Staccato® device, which utilizes electric energy for vaporization of a drug film for the delivery of loxapine (marketed as Adasuve®) [33]. However, Adasuve® is not a typical dry powder formulation as the inhaled particles consist of droplets with condensed loxapine vapor. DPIs can be classified through the number of doses they contain and the metering principle (see Figure 3) [18]. Single-dose DPIs are usually operated with the formulation filled into capsules. For some APIs, the inhalation of multiple capsules is required for one therapeutic dose (e.g., TOBI® Podhaler®).

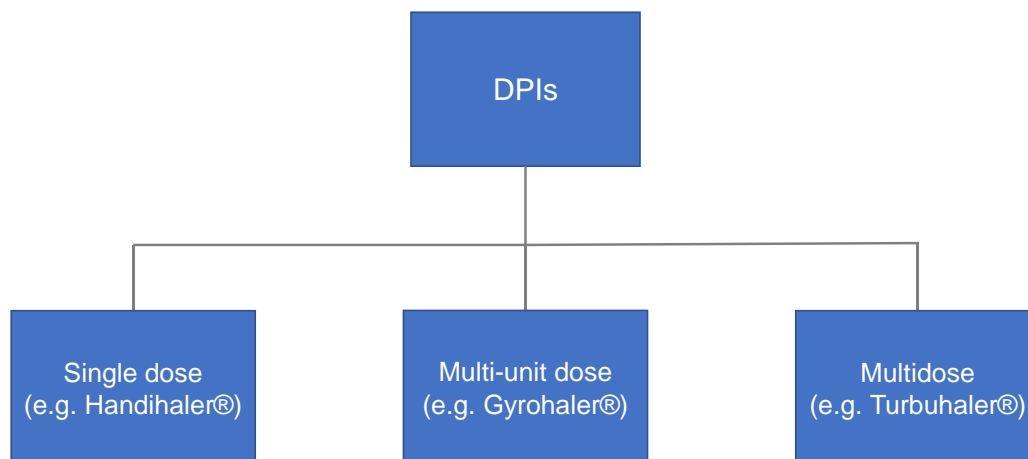


Figure 3: Classification of DPIs (dry powder inhalers) with regard to number of doses and dosing principle.

Multidose devices can either have multi-unit (pre-metered) doses or have a reservoir or cartridge with the formulation that will be metered by the device. The latter principle requires a well flowing powder and might be sensitive to environmental humidity which might cause dosing errors. Therefore, pre-metered doses filled into aluminum blisters or discs typically are favored.

DPIs can also be classified according to their intrinsic resistance. For powder dispersion, devices are designed with e.g., certain orifices or swirl chambers, which show varying resistance to the airflow passing the device [34]. The correlation between device resistance and flow rate is expressed in the following equation [35]:

$$\sqrt{\Delta P} = Q * R \quad \text{Eq. (2)}$$

With $\sqrt{\Delta P}$ being the square root of the pressure drop [kPa], Q being the flow rate [l/min] and R being the intrinsic device resistance [$\text{kPa}^{1/2}/\text{L} * \text{min}^{-1}$].

For instance, the HandiHaler® is characterized as high resistance device, meaning a lower flow rate is required for a certain pressure drop to occur than for the GyroHaler®, which is a medium/low resistance device [36,37]. High flow rates can increase the impaction in the upper respiratory tract, which result in a lower deposited dose in the lower respiratory tract [34,38]. The device poses a resistance to the inspiratory flow of the patient. Different inspiratory flow rates may lead to different deposited amounts of an API (so-called flow rate dependency). Both the GyroHaler® and the HandiHaler® show a low flow rate dependency [36,39]. Nevertheless, the dependency of the flow rate is not only affected by the device, but also by the formulation [40].

Blister-based devices might be beneficial for humidity-sensitive compounds as aluminum shows low vapor permeability. Furthermore, aluminum is not hygroscopic in contradiction to hydroxypropyl methylcellulose (HPMC) as a capsule material [41]. In addition, multidose devices with a powder reservoir or multi-unit devices with pre-metered blisters might be easier to handle for the patients and therefore might enhance patients' adherence. However, they might be disadvantageous for the delivery of high dose compounds as capsules might support the dispersibility of the powder.

1.2.3.2 Particle interactions

The key parameter for effective deposition of a dry powder formulation in the respiratory tract is the dispersion of the powder particles. Dry powder particles for inhalation show high cohesion and agglomeration, which is due to their small geometric particle size. For powder dispersion the cohesion of the particles, that is governed by particle interaction, needs to be overcome. There are four main forces of interaction [32]:

- Van der Waals forces
- Electrostatic forces
- Capillary forces
- Mechanical interlocking

"*Van-der-Waals forces* arise due to dipole–dipole interactions between atoms and molecules of adjacent surfaces and depend on material properties" [42]. The dependency on the material attributes is expressed by material specific Hamaker constants. Assuming a spherical particle, the van der Waals forces are directly proportional to the geometric particle diameter and the respective Hamaker constant [16]. Van der Waals forces between two particles decrease rapidly with increasing separation distance of the surfaces [31]. *Electrostatic forces* arise by particle contacts. In case two solids come in contact with each other, a contact potential is generated. This is enhanced via charges by particle collisions and triboelectric charging [29]. *Capillary forces* arise between a particle and a surface by the surface tension of the liquid drawn into the capillary space at the contact [31]. *Mechanical interlocking* can occur for particles with a rough surface and large asperities [32]. Capillary forces and van der Waals forces are the most relevant interaction forces for particles below 10 μm and they are dependent on the size of the particles [42]. At ambient conditions, Van der Waals forces usually dominate the other cohesive forces for particles smaller than 10 μm [16,29,43].

At relative high humidity, capillary forces dominate, whereas at low humidity values electrostatic forces are dominant [44].

There are several approaches to overcome the cohesive forces in dry powders for inhalation. Reducing the free energy of the API by mixing with coarse carrier particles (e.g., lactose) is one of them. The API and the carrier form a so-called interactive mixture. The adhesion force must be strong enough that the API particles adhere to the coarse carrier during manufacturing, filling and storage. On the other hand, the adhesive force must be weak enough to enable aerosolization of the API and detachment from the carrier during the inhalation process [32]. Another approach is particle engineering with the aim of avoiding carrier-based formulations in order to increase the drug load, as discussed in chapter 1.1. Several attempts have been made to alter the particle density, the surface energy, the morphology and much more [11,16] to obtain high dose formulations.

1.2.4 Nanoization

For the manufacturing of dry powder formulations for high dose drug delivery, spray drying is the most suitable operation. To obtain spherical, crystalline particles with a low density, API nanoparticles need to be spray dried. For poorly soluble APIs as ITZ, nanoparticles provide certain benefits such as a potential increase in bioavailability: As an increase in surface area leads to a faster dissolution rate and a potentially higher kinetic solubility [45], one approach to enhance dissolution and therefore bioavailability of poorly soluble APIs is the reduction of particle size to nanoparticles.

For the manufacturing of nanosuspensions, two different approaches, known as bottom-up (e.g., precipitation) or top-down (e.g., milling) processes, can be used. Common top-down approaches are high-pressure homogenization and media milling. Media milling, which is also known as “wet stirred media milling” or “bead milling”, decreases the size of particles suspended in a liquid by means of milling beads.

In the course of milling, two different processes are occurring concurrently: the suspended particles are breaking down due to mechanical stress and in parallel might also agglomerate due to hydrophobic interparticulate forces (i.e., van der Waals forces) [46]. A decrease in particle size results in an increased surface area. Consequently, the Gibbs free energy is increased, which leads to a thermodynamically unstable system that tends to reduce the free energy by particle agglomeration, flocculation or crystal growth [47], also known as Ostwald ripening [48,49].

To overcome these issues, a suitable stabilizer system is needed [50]. There are two main approaches to stabilize nanosuspensions, the steric stabilization by forming a physical barrier, e.g., by polymers, and/or the electrostatic stabilization by electrostatic repulsion. The latter mechanism is applicable for ionic stabilizers e.g., sodium dodecyl sulfate. According to the DLVO theory [51,52], the ionic surfactant enables the formation of an electric double layer on the surface of the nanoparticles resulting in repulsive forces if particles approach each other [47]. The group of non-ionic stabilizers comprises polymers such as cellulose derivatives (e.g., hydroxy propyl cellulose) and non-ionic surfactants, for example polysorbates. These stabilizers adsorb onto the surface of the particles and form a physical barrier towards the other particles in the suspension. The combined stabilization approach of both principles is often beneficial and known as electrosteric stabilization [46]. The composition and concentration of the stabilizer system is of utmost importance during the development of a nanosuspension formulation. APIs are typically used in a concentration mass ratio of 1:3 to 50:1 (API to stabilizer) [53,54].

Besides the particle size, there are several other attributes that are considered crucial for the development of nanosuspensions, like particle shape and morphology, solid-state properties, chemical and physical stability. To increase the long-term stability or for further processing into a solid dosage form (e.g., a dry powder formulation for respiratory drug delivery) nanosuspensions are being dried by e.g., spray drying or freeze-drying.

1.2.5 Spray drying

Most of the marketed engineered particles for high dose respiratory delivery are produced by spray drying such as TOBI® Podhaler® or Bronchitol®. As described in chapter 1.1, spray drying provides great advantages for manufacturing of inhalable particles. Usually spherical particles are obtained, that show a suitable particle size with a low density and excellent dispersibility [22]. Even the particle morphology can be tailored [27]. As the nanoparticles cannot be inhaled as such due to their high cohesiveness, spray drying offers the opportunity to transfer them into an inhalable powder.

Spray drying describes the process of drying a solution, suspension, or emulsion, which is atomized into droplets and dried in a hot gas (air or nitrogen) stream. The process has widely been used for many years [55].

A spray dryer consists (among other parts) of a drying chamber (where the main drying takes place, 5), a nozzle (which atomizes the formulation, 2) and a cyclone (10) for particle collection, see Figure 4).

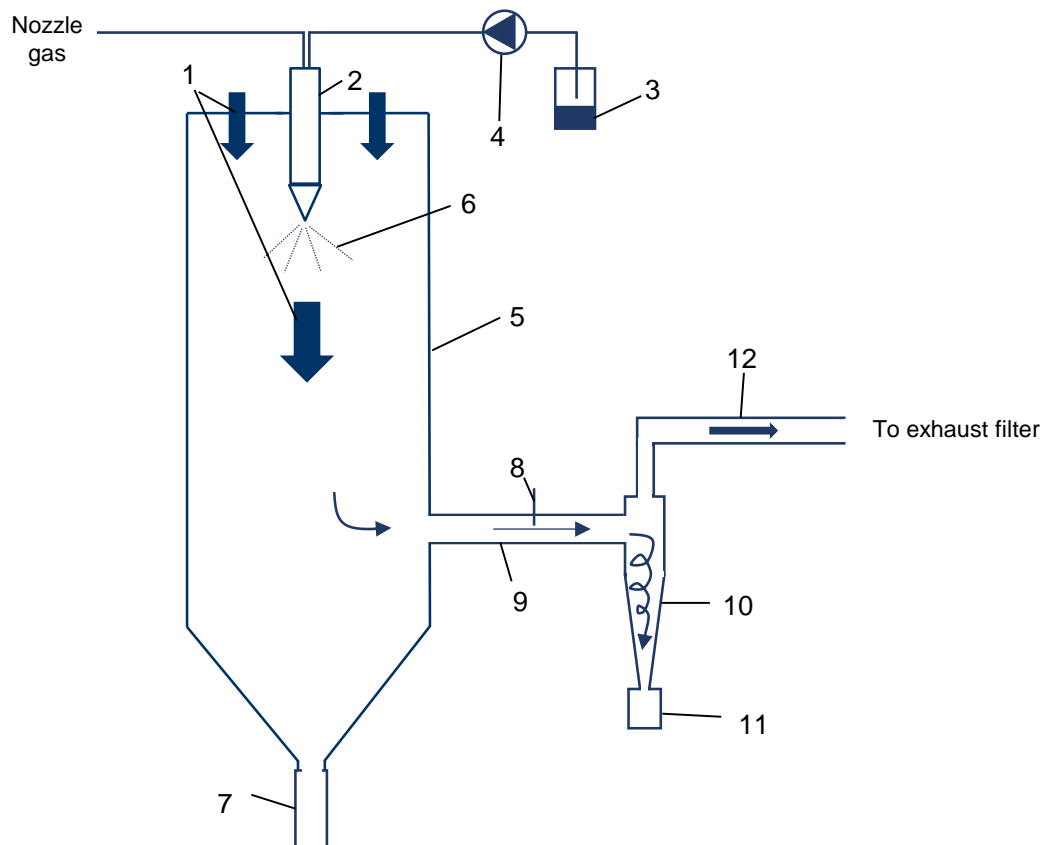


Figure 4: Schematic illustration of a laboratory-scale spray dryer. The feed solution/suspension (3) is pumped with a peristaltic pump (4) into the nozzle (2). The feed liquid is atomized into droplets by the nozzle gas (6). The droplets are dried in the hot gas stream (1) in the drying chamber (5). The dried particles follow the gas stream into the connection (9) of drying chamber and cyclone (10). The particles are then collected in a glass (11), whereas the process gas stream with residual small particles enters the connection (12) to the exhaust filter. Particles, which are too large to follow the process gas stream will get deposited in a glass below the drying chamber (7). The outlet temperature is measured (8) in the connection between the drying chamber and the cyclone.

Laboratory spray dryers often use pneumatic two-fluid nozzles for atomization, where the formulation is atomized by a gas (air or nitrogen). Several spray drying parameters impact the properties of the dried particles like particle size, morphology, surface roughness or solid-state. Some of these parameters are

- feed rate of the formulation
- outlet temperature (which is the temperature measured at the connection between drying chamber and cyclone (8) and can be regarded as product temperature)
- atomization rate (nozzle gas flow)
- formulation composition.

The outlet temperature is the result of the interplay between inlet temperature (temperature of the drying gas), feed rate, type of solvent, drying gas rate and the concentration of total solids.

As described in chapter 1.2.2, the aerodynamic diameter is highly dependent on the geometric diameter of the particle. The geometric diameter itself is affected by the feed solution concentration and the droplet diameter [27]. Therefore, the droplet size during spray drying is of great importance. For pneumatic nozzles, the droplet size can be described by the complex Kim-Marshall-equation [56]: It is affected by the surface tension of the formulation, the viscosity, the density, the orifice diameter of the nozzle and the gas/liquid mass ratio [56]. Regarding the formulation, it is assumed that surface tension has a minor impact compared to viscosity, especially for spray drying with high atomization rates and low feed rates [56–58]. Increasing the viscosity of the feed solution leads to larger droplets during atomization [55,56].

As soon as a droplet is atomized and encounters the hot gas in the drying chamber the drying process starts. The drying process of a droplet with solutes, a coupled heat and mass transfer, can be regarded as a two-step process [59]. Solvent evaporation takes place “with the difference between the vapor pressure of the solvent in the droplet and its partial pressure in the gas phase being the driving force” [23]. At the beginning, solvent evaporation happens at the droplet surface with a constant evaporation rate (controlled by the heat transfer to the droplet’s surface) leading to decreasing droplet diameters [58,59]. The temperature of the droplet is equal to the so-called wet-bulb temperature [56]. This is considered as the constant-rate stage [58]. Once the surface of the droplet is enriched with the solute, the solute diffuses towards the center of the droplet caused by a concentration gradient [58]. During further drying, this diffusion will become lower than the reduction of droplet diameter resulting in crust formation. This is the start of the second stage, the so-called falling-rate stage with decreasing drying rate [58]. The drying rate is now governed by diffusion of the solvent through the crust or pores of the crust [23,60]. Crust thickening leads to a reduction in the drying rate. The droplet’s surface temperature will increase to the so-called dry-bulb temperature at the end of the drying process [58].

The Peclet number describes the ratio of the evaporation rate of the solvent and the diffusion coefficient of the solute in the liquid phase [61]. The formation of particles differs depending on the Peclet number and results in various particle morphologies, more details were described by Vehring (2008) [27]. The Peclet number can be calculated according to Equation 3:

$$Pe = \frac{K}{8 D_i} \quad \text{Eq. (3)}$$

with Pe being the Peclet number [-], K being the solvent evaporation rate and D_i being the diffusion coefficient of the solute in the liquid phase.

If the Peclet number is smaller than 1, the diffusion of the solutes is faster than the evaporation of the solvent and shrinkage of droplets, leading to small and dense particles. If the diffusion of the solute is slower than the droplet evaporation, this will result in Peclet numbers greater than 1 and larger, hollow particles [62].

1.3 Objectives

The purpose of this work was to develop a dry powder formulation for high dose respiratory drug delivery of ITZ that could potentially be used within the context of an experimental ABPA or IPA therapy. A combination of media milling, and spray drying was applied as particle engineering technique to manufacture nano- in microparticles showing suitable properties for respiratory deposition. The aerodynamic performance of the dry powder formulations was investigated with regard to drug load, the impact of nanoization and the effect of the inhalation devices used.

Chapter 3.1 describes the development of a suitable nanoization process using a special type of mill. Process parameters (being the milling speed and the diameter of the milling beads) as well as formulation parameters (such as stabilizer concentration or critical material attributes) were evaluated. The impact of the stabilizer concentration on the critical material attributes (such as particle size, zeta potential, morphology or solid-state) of the suspensions was evaluated in depth and optimized.

Chapter 3.2 reports a suitable spray drying method to transform the nanosuspensions into respirable microparticles as well as the optimization of the process parameters thereof. The influence of the feed rate and gas flow rate on the primary droplet size obtained from the two-fluid nozzle, as well as the impact of the outlet temperature and stabilizing agents on the material attributes of the spray dried particles were investigated. The ITZ nanosuspensions were then spray dried under optimized conditions using varying amounts of mannitol, which acts as a stabilizing agent (matrix former) for the microparticles.

A fast screening tool (pressure titration) as well as full resolution cascade impaction analysis were used to evaluate the aerosol performances of the formulations obtained, which is presented in chapter 3.3. The impact of the drug load and particle engineering were investigated with regard to the fine particle dose. Two different devices - the capsule-based HandiHaler® und the blister-based GyroHaler® - were compared with focus on their de-aggregation performance by assessing their delivered fine particle doses.

2 Material and methods

2.1 Materials

The following API and excipients were used for the experiments:

Table 1: Overview of used API and excipients. BCS: Biopharmaceutics classification system

Name	Abbr.	LOT	Supplier	Comment
Itraconazole	ITZ	20170106	Wuhan Atomole Chemicals Co., Ltd, China	BCS class II compound: low solubility of ~ 1 ng/ml in water (neutral pH) and high lipophilicity (logP ~ 6) [63]
Hydroxypropyl cellulose, Type SL	HPC-SL	NEA-1431	Nippon Soda Co., Ltd, Tokyo, Japan	Steric stabilizer, known for stabilization of nanosuspensions [53]
Polysorbate 80 (<i>Tween® 80</i>)	PS80	1/2412672	Kolb Distribution AG, Hedingen, Switzerland	Non-ionic surfactant, known for stabilization of nanosuspensions [53], approved for inhalation [64]
Sodium dodecyl sulfate (<i>Kolliphor® SLS fine</i>)	SDS	13665368	BTC Europe GmbH, Monheim am Rhein, Germany	Ionic surfactant, known for stabilization of nanosuspensions [53]
Mannitol (<i>Pearlitol® 50 C</i>)	MAN	E842L	Roquette, Lestrem, France	Known as matrix former for inhalable nanoparticles [23], approved for inhalation [13]

2.1.1 Devices

2.1.1.1 HandiHaler®

The HandiHaler® (see Figure 5) was developed by Boehringer Ingelheim and is a capsule-based single-dose device. It is marketed for the delivery of tiotropium as a carrier-based formulation. For the inhalation maneuver, the mouthpiece (1) has to be tilt back and a capsule is placed in the capsule compartment (3). The mouthpiece is then tilt back. The capsule is pierced twice (2) by pushing the turquoise button.

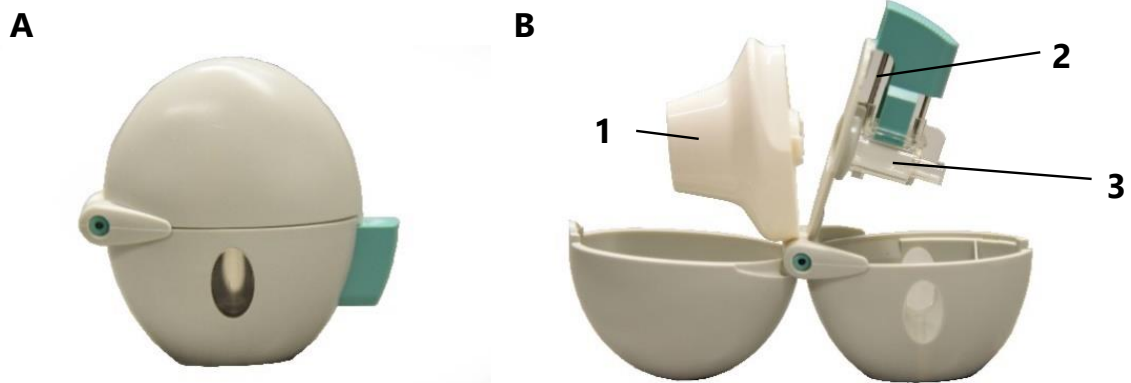


Figure 5: HandiHaler® closed (A) and opened (B). This capsule-based device consists of a mouthpiece (1), a capsule-piercing element (2) and a capsule compartment (3). It was developed by Boehringer Ingelheim. © Boehringer Ingelheim

During inhalation the capsule axially vibrates and enables the support of deagglomeration of the formulation in the capsule [65,66]. The capsule is pushed up against a stainless-steel mesh and remains in the capsule compartment. The HandiHaler® is characterized as high-resistance device with an intrinsic resistance of $0.049 \text{ kPa}^{1/2}/\text{L} \cdot \text{min}^{-1}$ [67]. The HandiHaler® were obtained from Boehringer Ingelheim Pharma GmbH & Co. KG, Germany.

2.1.1.2 GyroHaler®

The GyroHaler® was developed by Vectura Group Ltd and is a multi-dose device with pre-metered doses. Currently, it is marketed as AirFluSal® Forspiro® by Novartis for the delivery of a combination of salmeterol and fluticasone as a carrier-based formulation [68]. The formulation is filled into aluminum foil blister strips (see Figure 6 (4)), which are pierced for inhalation with the piercing element (2). The formulation is aerosolized by the airstream coming vertically from the mouthpiece (1) to the blister cavity (3).

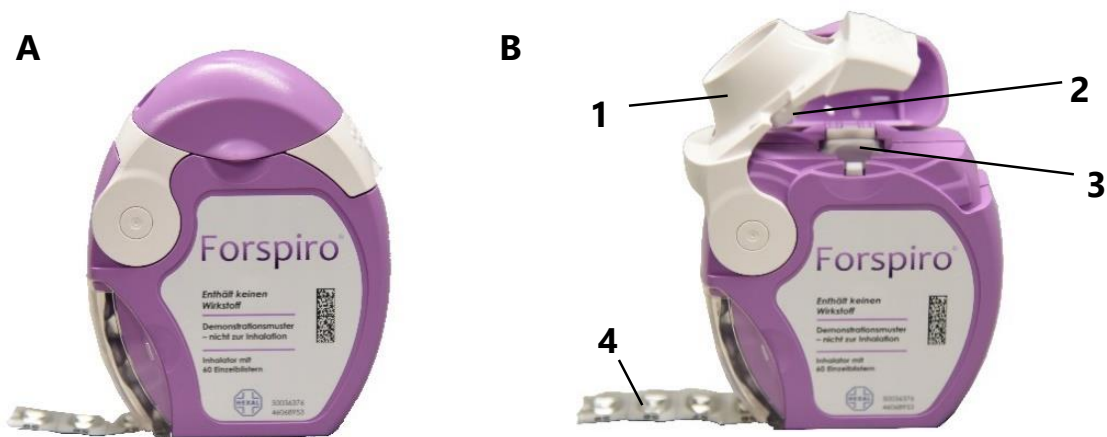


Figure 6: Multi dose inhalation device developed by Vectura Group Ltd. It consists of a mouthpiece (1), a blister piercing element (2) and the blister cavity (3). After inhalation the empty blister cavities are released (4). The used blister-based device is licensed to Novartis and marketed as Forspiro® (© Boehringer Ingelheim)

For the next inhalation maneuver, the mouthpiece needs to be tilt to the side, which moves the emptied blister cavity forward and a new cavity arises. Once the mouthpiece is tilt back, the new cavity will be pierced. As mentioned before, the GyroHaler® is a low/medium-resistance device, showing an intrinsic resistance of approximately $0.026 \text{ kPa}^{1/2}/\text{L} \cdot \text{min}^{-1}$ [68]. The GyroHaler® were obtained from a local pharmacy as training devices.

2.2 Methods

2.2.1 Manufacturing processes

2.2.1.1 Jet-milling

Prior to use, ITZ starting material was sieved with a preparative sieve (mesh size $315 \mu\text{m}$) to remove agglomerates. The sieved material was jet-milled with a Food Pharma Systems Pilot Mill 2 (Food Pharma Systems, Como, Italy) at 7 bars grinding pressure using nitrogen as process gas. Milling was conducted with a batch size of 400 g and at a feed rate of 50 g per hour. The milled powder was filled into twist-off glasses and sealed into aluminum bags with a desiccant for storage.

2.2.1.2 Suspension preparation

For the stabilizer solution, SDS and PS80 were dissolved in demineralized water, HPC-SL was added, stirred overnight at 200 rpm with a magnetic stirrer to enable complete dissolution, and filtered ($0.2 \mu\text{m}$, cellulose acetate membrane). To ensure a homogeneous suspension, 4.2 g of the jet-milled ITZ and 42 g of the stabilizer solution were pre-suspended and mixed in a 100 ml duran glass bottle

(filling level approximately 40% v/v) with an acoustic mixer LabRAM™ II (Resodyn Acoustic Mixers, Butte, MO, USA) at 50 times gravitational acceleration for two cycles of 45 seconds each. The mixer combined low oscillation frequencies at a resonant condition (approximately 60 Hz) with a relatively large displacement amplitude (up to 14 mm) to a high mixing energy which is measured in acceleration of gravity [69,70]. After the first 45 sec the bottle is gently shaken to destroy powder agglomerates. The suspension was then stirred on a magnetic stirrer for 60 minutes to remove foam.

2.2.1.3 Nano milling

Nano milling was performed using a ZentriMix 380R (Andreas Hettich GmbH & Co. KG, Tuttlingen, Germany) dual centrifuge. The rotor holds four 10 ml PP processing vials, filled with 5.5 g of the homogenized suspension and 5 g of milling beads (zirconium oxide, yttrium stabilized, VMA Getzmann GmbH, Reichshof, Germany, various sizes) each. Figure 7 shows the rotation principle of the dual centrifuge.

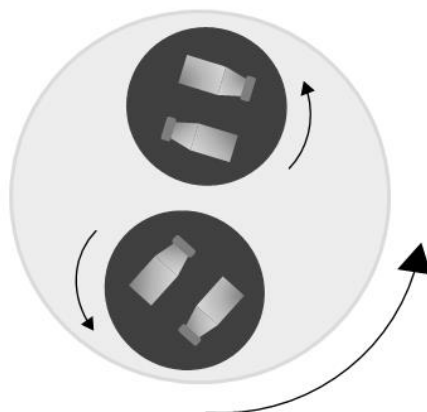


Figure 7: Schematic illustration of nano milling with the ZentriMix. The rotor enables both a rotation around the longitudinal axis (big black arrow) and a secondary rotation around each vial holder (small black arrows). The combined dual rotation facilitates the creation of a high kinetic energy with four vials being milled at the same time.

During milling, A rotation around the longitudinal axis of the rotor is combined with a secondary rotation around each vial holder, which enables a high kinetic energy. Further details concerning the ZentriMix can be found in an article by Hagedorn et al. (2017) [71]. Compared to conventional media milling, the potential of this novel type of mill has been evaluated to accelerate early formulation development for nanosuspensions and successful upscaling to larger agitator bead mills has been demonstrated [72].

Table 2: Overview of the parameters during evaluation of the milling process

Purpose	Bead size [mm]	Stabilizer concentration w/w	Speed [rpm]	Temperature inside the milling chamber [°C]
Speed evaluation	0.3 – 0.4	0.9% HPC-SL, 0.14% SDS, 0.14% PS80	500	4
			1500	
Temperature Evaluation	0.3 – 0.4	0.9% HPC-SL, 0.14% SDS, 0.14% PS80	1500	4
				-10
Bead size evaluation	0.1 – 0.2	0.9% HPC-SL, 0.28% SDS, 0.28% PS80	1500	4
	0.3 – 0.4	0.9% HPC-SL, 0.14% SDS, 0.14% PS80		
	0.4 – 0.6			
	0.6 – 0.8			
	0.8 – 1.0			
	1.2 – 1.4			
	1.6 – 1.8			
	2.0 – 2.5			
	2.6 – 3.3			
Stabilizer impact on CMA	0.3 – 0.4	0.9% HPC-SL, 0.14% SDS, 0.14% PS80	1500	4
		0.9% HPC-SL, 0.07% SDS, 0.07% PS80		

Table 2 shows the varying and constant parameters for evaluation of the nanoization process. As stabilizers hydroxy propyl cellulose SL (HPC-SL), sodium dodecyl sulfate (SDS) and polysorbate 80 (PS80) were used.

For all bead sizes, the mass of beads is kept constant. The theoretical number n of units in 5 g of beads (e.g., diameter 0.3 - 0.4 mm; assuming a mean diameter of 0.35 mm) can be calculated according to Equation 4:

$$n = \frac{V_{5g}}{V_{0.35}} = \frac{833.33 \text{ mm}^3}{0.022449 \text{ mm}^3} = 37121 \quad \text{Eq. (4)}$$

V_{5g} is volume of 5 g beads calculated with the bead density of 6 g/cm^3 and $V_{0.35}$ is the volume of one bead assuming a mean diameter of 0.35 mm.

An overview of the bead diameters and resulting numbers is given in Table 9, chapter 3.1.2.3.

2.2.1.4 Spray drying

A lab-scale spray dryer Büchi B290 Advanced (Büchi Labortechnik AG, Flawil, Switzerland) was used. The spray dryer was equipped with a high-performance cyclone and a 0.5 mm nozzle with a 1.5 mm nozzle cap. An in-house made sample collector was used to minimize product loss. The aspirator was set to 100% and the flow rate of the nozzle gas (pressurized air) was determined with an Omega FMA-1611A mass airflow sensor (Omega Engineering Inc., Stamford, CT, US, as standard liters per minute [SL/min], meaning the flow rate at standard conditions for pressure and temperature: 1 bar and 273.15 K). The impact of different feed rates, nozzle gas flow rates (6-12 bar) and outlet temperatures were evaluated during process development (as shown in Table 3). Further details can be found in chapter 3.2.1. For evaluation of the droplet size, water (H_2O) with stabilizers for the nano-suspension (hydroxypropyl cellulose SL (HPC-SL), sodium dodecyl sulfate (SDS) and polysorbate 80 (PS80)) was used.

Table 3: Overview of the spray drying parameters used for process evaluation and for the manufacturing of engineered ITZ particles. Nozzle gas flow rate is given in standard liters per minute (SL/min, flow rate at standard conditions for pressure and temperature: 1 bar and 0°C).

Response parameter	Solid	Medium	Solution composition [%w/w]	Nozzle gas flow rate [SL/min]	Outlet temperature [°C]	Feed rate [g/min]
Droplet size	MAN	H_2O + stabilizers	0.7% HPC-SL 0.1% SDS 0.1% PS80 4.1% MAN 95.0% H_2O	13, 18, 23, 28, 33	N/A	2.5, 5, 10
Particle size, solid-state, morphology	MAN	H_2O	5.0% MAN 95.0% H_2O	23	60, 80, 100	5
		H_2O + stabilizers	0.7% HPC-SL 0.1% SDS 0.1% PS80 4.1% MAN 95.0% H_2O	23	60, 80, 100	5

The nanosuspensions were mixed under constant stirring with a magnetic stirrer with mannitol at defined concentrations (25:75, 50:50, 75:25 and 100:0 [% w/w]) and sufficient amounts of demineralized water were added to adjust to a total solids fraction of 5 %. All spray drying experiments were conducted with the optimized parameters. As a control, one sample was spray dried without nanoization and without MAN (same composition as 100:0, JM SD). All spray dried powders were sieved (preparative sieve with a diameter of 150 μm) after spray drying and stored in a desiccator over molecular sieve. A formulation overview is given in Table 4.

Table 4: Overview of samples with regard to preparation method and ITZ:MAN ratio [% w/w]

Sample name	Jet Milling (JM)	Nanoization (NS)	Spray drying (SD)	ITZ:MAN ratio w/w [%]
25:75	X	X	X	25:75
50:50	X	X	X	50:50
75:25	X	X	X	75:25
100:0	X	X	X	100:0
JM SD	X		X	100:0
JM	X			100:0

2.2.1.5 Filling of dry powders

An in-house made filling unit (BI drum filler) was used for loading of the GyroHaler® and the HandiHaler® with a powder dose of 13 mg \pm 0.5 mg (limited volume of blister cavities). The individual elements are shown in Figure 8. The filling principle is volume-based: 60 μl cavities were filled with 150 mbar negative pressure and powder was released in blister cavity/capsules with 150 mbar pressurized air. To load the GyroHaler®, blister cavities made of aluminum were formed (2) under positive pressure and filled with powder afterwards (3). The powder was filled into the cavities of the drum by negative pressure and the powder pellet was released into the blister cavity. Following, the filled cavities were sealed (4) and cut into the suitable dimensions (5). For experiments with the HandiHaler® only the filling element (3) was used. Size 3 HPMC capsule halves were placed under the drum and the powder pellet was released directly into the capsule with the help of a stainless-steel adapter.

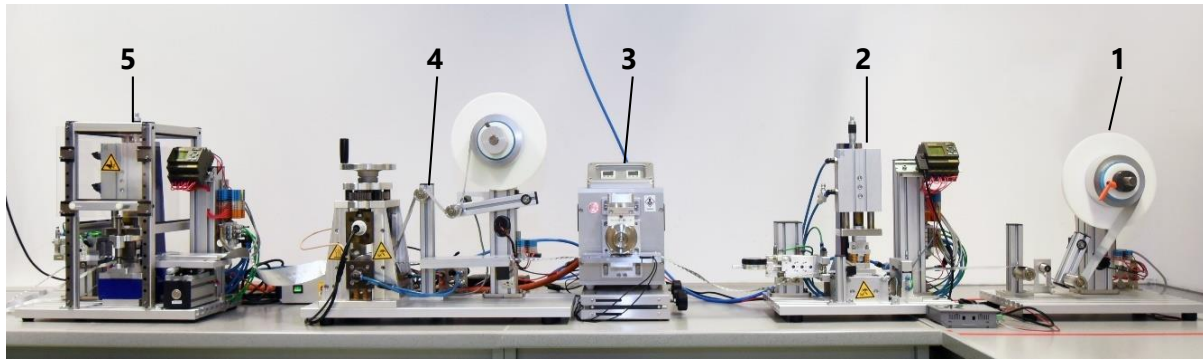


Figure 8: BI drum filler. From right to left: Foil holder (1), blister former (2), filling element (3), sealing element (4), cutting element (5). © Boehringer Ingelheim

Samples JM SD and JM were filled manually as no successful automated filling with the filling unit was possible, as also described in chapter 3.3.1.

The detailed construction of the filling element is depicted in Figure 9. The formulation was filled into the powder reservoir (1) and dosed into the cavity of the drum (3) with the help of an impeller (2) and negative pressure. Afterwards, the powder in the cavity was released into the preformed cavity of the aluminum foil (4) using pressured air.

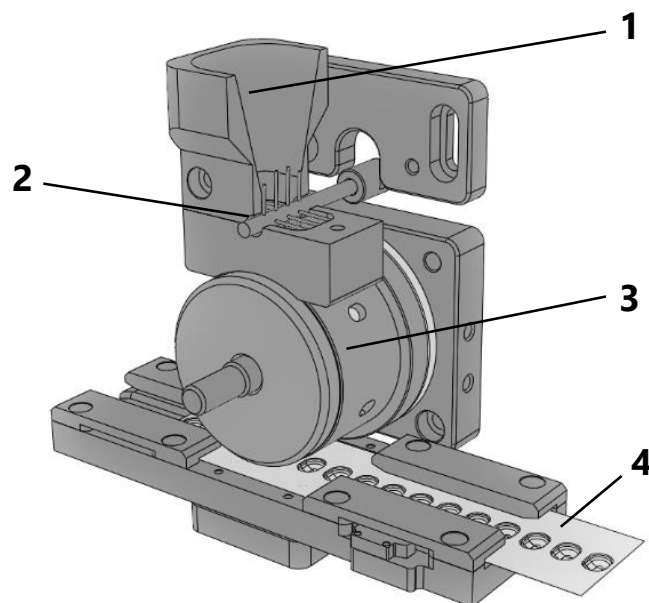


Figure 9: Filling element of in-house made blister machine in detail. (1) Powder reservoir, (2) Powder feeding impeller, (3) drum with powder cavities, (4) blister foil with preformed cavities. Image was created with SolidWorks®

The volume-based drum filling principle used is commercially available (Omnidose® by Harro Höfliger). For the drum filling principle, upscaling should be possible and has been proven to be feasible from the Omnidose TT to Omnidose DF1 [73].

2.2.2 Analytical methods

2.2.2.1 Dynamic light scattering (DLS)

A Zetasizer® Nano S (Malvern Panalytical Herrenberg, Germany) was used to determine the particle size distributions of the nanoparticles using dynamic light scattering. The nanosuspensions were diluted with filtered (0.2 µm, cellulose acetate membrane) saturated ITZ solution in demineralized water at a ratio of 1:500 [74]. The measurement was carried out with disposable semi-micro polymethyl methacrylate cuvettes at 25 °C. Detection angle was fixed at 173°. 10 measurements were performed per experiment and each sample was measured in triplicate. The particle size and size distribution were displayed as Z-average and polydispersity index (PDI), respectively. Particle size data of the nanoparticles were processed with the Zetasizer® Software Version 7.12 (Malvern Panalytical, Herrenberg, Germany).

2.2.2.2 Zeta potential

Zeta potential was determined with a SZ-100 nanoPartica analyzer (Horiba Europe GmbH, Oberursel, Germany). A 6 mm cuvette with a carbon electrode was used. The conductivity of the samples was adjusted as described in [75] and the temperature was kept at 25 °C. The sample was diluted 1:100 with filtered (0.2 µm, cellulose acetate membrane) demineralized water. The zeta potential was calculated based on the electrophoretic mobility using the Helmholtz-Smoluchowski equation with the software Horiba NextGen Project V 2.40.

2.2.2.3 X-ray powder diffraction (XRPD)

Nanosuspension:

After milling, the samples were centrifuged at 20817 relative centrifugation force/g for 15 minutes and the residue was used to investigate the solid-state properties. The diffraction patterns were obtained using a Bruker AXS D8 Discover DAVINCI diffractometer (Bruker Corporation, Billerica, MA, USA) using Cu-K α radiation (40 kV voltage and 40 mA current). All scans were performed at 0.5 s/step with a step size of 0.02° from 5° to 40° 2 Theta angles. Measurements were carried out in reflection mode (coupled two Theta/Theta).

Dry powder particles:

The diffraction patterns were obtained using STOE Powder Diffraction System StadiP (STOE & Cie GmbH, Darmstadt, Germany) using Cu-radiation (1.5406 Å, 40 kV voltage and 40 mA current). All scans were performed at a step size of 0.4° and 3 s/step from 3° to 40° 2 Theta angles. Measurements were carried out in transmission mode. Physical blends were prepared by mixing all components with the LabRAM II at 50 times acceleration for 60 seconds. Reference materials for α -MAN and δ -MAN were prepared according to the procedure described in [76].

Raw XRPD data were converted to American Standard Code for Information Interchange (ASCII) format with Bruker DIFFRAC 7.5 and processed using Origin Pro® 2017 (Origin Lab® Corporation, Northampton, MA, USA).

2.2.2.4 Differential scanning calorimetry (DSC)

The thermal behavior of the nanosuspensions was investigated with a DSC2500 Discovery (TA Instruments®, New Castle, DE, USA). The samples used for X-ray diffraction were dried at 40 °C under vacuum for 1 h to remove any residual water. 3-5 mg were weighed into aluminum pans with perforated lids and compacted gently with a punch in order to ensure a homogeneous heat transfer. Nitrogen was used as a purging gas at a flow rate of 50 ml/min. Samples were heated at 10 C°/min from 25 °C to 200 °C. DSC data were analyzed using TA Instruments TRIOS software (TA Instruments, New Castle, DE, USA).

2.2.2.5 Determination of ITZ assay

ITZ content after nanoization and after spray drying as well as content uniformity of the spray dried powders was measured via HPLC (all components Agilent 1200 series): an Inertsil® ODS-3 (3 μ m, 4.6 x 150 mm, GL Sciences Inc., Tokyo, Japan) HPLC column was used. The mobile phase consisted of 75 % acetonitrile and 25 % phosphate buffer (7.6 mmol) pH 6.4. Analysis was carried out at a flow rate of 1 ml/min and a detection wavelength of 263 nm (photodiode array detector). DMSO was used as solvent. HPLC data were analyzed with Empower 3 Pro software (Waters Corporation, Milford, USA).

2.2.2.6 Saturation solubility

The saturation solubility was determined after 24 h shaking at room temperature in a Thermo-Mixer® (Eppendorf SE, Hamburg, Germany). The suspension was centrifugated with 20817 rcf for

10 min and the supernatant was filtrated with a 0.2 μm cellulose acetate filter before analysis by HPLC using the method described above.

2.2.2.7 Loss on drying (LoD)

A halogen moisture analyzer HG 63 from Mettler Toledo GmbH (Gießen, Germany) was used for the determination of the residual moisture after spray drying. About 500 mg of the sample were heated to 105 °C for 15 min.

2.2.2.8 Laser diffraction

Droplet size generated with the Büchi nozzle:

The size distribution of the droplets generated with the Büchi nozzle was determined with a Helos H1411 (Sympatec GmbH, Clausthal-Zellerfeld, Germany) laser diffractometer using the R3 lens (0.9-175 μm). Due to practical reasons, the peristaltic pump of the Büchi was operated with a stand-alone peristaltic pump (Ismatec model ISM596D, Cole-Parmer GmbH, Wertheim, Germany). The settings of the peristaltic pump were comparable to the conditions that occurred during the spray drying. Droplet sizes were evaluated at five different nozzle gas flow rates (13, 18, 23, 28, 33 SL/min) and three different pump rates (5, 10, 15 g/min), see also Table 3. The distance between the nozzle tip and the laser beam was kept constant at 7 cm and the focal length was adjusted to 10 mm. Nozzle gas used was pressurized air. In order to mimic the spray drying runs, mannitol in stabilizer solution was used for this investigation: MAN was added to the stabilizer medium at a ratio of 4:1, which is equivalent to the intermediate ratio of the ITZ nanosuspension samples to be spray dried using the optimized process parameters. The concentration of total solids was kept at 5% (w/w). Data were analyzed with Windox 5 software using Mie theory with refractive index of 1.33. The Fraunhofer approximation of the Mie theory is commonly used for evaluation of particle sizes in micrometer range due to its wide applicability as no information on optical properties are necessary. The Fraunhofer approximation is valid under certain conditions e.g., for particles much larger than the wavelength of the laser. However, for transparent particles (such as water droplets) the Fraunhofer approximation predicts the false existence of small particles due to secondary scattering [77]. Therefore, the Mie theory is applied here.

Dry powder dispersibility (Pressure Titration):

For assessing the deagglomeration ability of the powders, the mean particle size (d_{50}) was evaluated using different dispersion pressures (so-called "pressure titration"). A detailed description of this method can be found in [78]. The particle size of the powder samples was determined at increasing

dispersion pressures from 0.1 bar to 3.5 bars with the Mastersizer 2000™ equipped with a Scirocco dry dispersion unit (Malvern Panalytical Herrenberg, Germany). 3-5 mg of the sample were placed in the hopper, which was operated with 30% vibration. Each sample was measured in triplicate with pressurized air as dispersion medium. Particle refractive index for calculation of particle sizes was set to 1.64 [79].

2.2.2.9 Densities

2.2.2.9.1 Particle density

Particle density was determined with a AccuPyc II 1340 helium gas pycnometer (Micromeritics Instrument Corporation, Norcross, GA, USA). The measurements were conducted under controlled temperature to ensure constant conditions for analysis. The fill pressure was set to 1.34 bar with an equilibration rate of 0.00034 bar/min. The particle density is reported as the average of 10 cycles.

2.2.2.9.2 Bulk and tapped density

Bulk and tapped densities were evaluated as described in Ph. Eur. 10.1, chapter 2.9.34, method 1 [80]. using SVM tapped density tester/settling device (Erweka GmbH, Langen, Germany) and approximately 1 g of each formulation was weighed into a 10 ml measuring cylinder. Calculations for the bulk and tapped densities according to Ph. Eur. are shown in Equation 5 and Equation 6, respectively:

$$\rho_0 = \frac{m}{V_0} \quad \text{Eq. (5)}$$

$$\rho_f = \frac{m}{V_f} \quad \text{Eq. (6)}$$

with ρ_0 being the bulk density, m being the mass of the powder, V_0 being the unsettled apparent volume, ρ_f being the tapped density and V_f being final tapped volume.

The Carr index (or compressibility index according to the Ph. Eur.) is an indicator of flowability, which is given by the ratio of bulk and tapped volumes (Equation 7):

$$\text{Carr index} = \frac{100 * (V_0 - V_f)}{V_0} \quad \text{Eq. (7)}$$

2.2.2.10 SEM images

The nanosuspensions were diluted 1:500 (same dilution as for DLS) with demineralized water and dried over night at room temperature on a coverslip. A Helios™ G4 CX Dualbeam™ (Thermo Scientific™ Inc, Waltham, MA, USA) microscope was used in secondary electron mode at 2 kV and 3 mm working distance. Samples were sputter coated with platinum.

For SEM investigations of the dry powder samples settings were changed to 1.5 kV with a working distance of 2 mm.

2.2.2.11 Dynamic vapor sorption (DVS)

To investigate relative moisture sorption and solid-state stability, dynamic vapor sorption was carried out with IGAsorp vapor sorption analyzer (Hiden Isochema Ltd, Warrington, UK). Samples of about 20 mg were placed into the instrument. An equilibration step (25°C, 30% relative humidity (rH) for 120 min) was conducted at the beginning. Measurements were taken at 25 °C with increments of 10 % rH (0-90% rH) for one cycle. Once the sample weight is stable, it is at equilibrium with the surrounding atmosphere. The measurement is then continued at the next humidity step (lower or higher relative humidity). The mass change is calculated relative to the mass obtained after an initial conditioning step. Further XRD measurements were run with the samples after DVS measurement.

2.2.2.12 Reconstitution of the nanoparticles

To investigate the reconstitution of the nanoparticles after spray drying, the powders were reconstituted in a volume yielding a concentration similar to the one of the nanosuspensions used for spray drying (i.e., a total solids fraction of 5 % w/w). The powder was weighed into vials, mixed with demineralized water and stirred with a magnetic stirrer for 24 h. The reconstituted nanoparticles were evaluated via dynamic light scattering with the method described above. Samples were taken after 1 h, 2 h, 4 h, 8 h, 12 h and 24 h and each formulation was measured in triplicate.

2.2.2.13 Aerosol analysis

The assessment of fine particles was done according to the requirements of the European Pharmacopoeia 10.2, chapter 2.9.18 [80]. A vacuum pump was connected by vacuum tubing (1) with the Next Generation Impactor NGI, resp. Apparatus E (Copley Scientific Ltd, Nottingham, UK). A timer controlled the two-way solenoid valve (2), which was attached to a flow control valve (4) with a metal coupling (3). The absolute pressure on both sides of the flow control valve (4) was determined

with two pressure gauges (5) to ensure a critical flow. Measurements were conducted in controlled environmental conditions: $22.5\text{ }^{\circ}\text{C} \pm 1.0\text{ }^{\circ}\text{C}$ and $55\text{ \% rH} \pm 10\text{ \% rH}$.

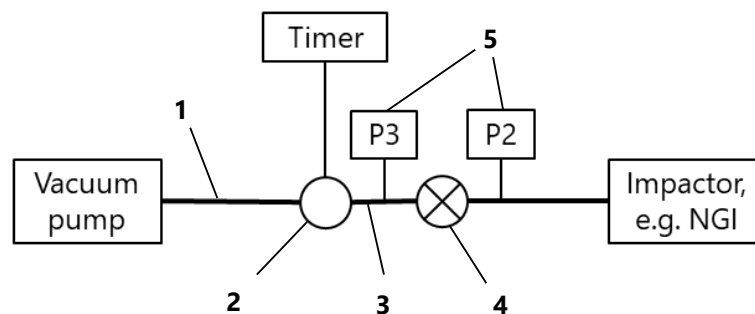


Figure 10: Experimental set-up for the assessment of fine particles according to the Ph. Eur. The vacuum pump is connected by vacuum tubing (1) with the impactor. A timer controls the two-way solenoid valve (2) which is attached to the flow control valve (4) with a metal coupling (3). Pressure before and after the flow control valve is determined with two pressure gauges (5). The scheme was modified from [80]

The construction of the NGI is depicted in Figure 11:



Figure 11: NGI (Apparatus E) for the assessment of fine particles according to the Ph. Eur [80]. The lid consists of a steel body with nozzles of a defined number and diameter (e.g., Stage 1 nozzle (1) or micro-orifice collector (MOC) (4)) and interstage pathways. The bottom frame comprises a tray with removable impaction cups (e.g., 2) and a connection to the vacuum pump (3). © Boehringer Ingelheim

NGI cups and the preseparator insert were coated with an ethanolic solution of Brij 35 in glycerol. 10 ml of the solvent DMSO were placed into the central preseparator cup. To achieve the required pressure drop of 4 kPa, measurements were conducted at a flow rate of 42.4 l/min for the Hand-iHaler® and 78.6 l/min for the GyroHaler®, respectively. As the cut-off diameters of the NGI are flow rate dependent, they differ for both devices, which is shown in Table 5.

Table 5: Cut-off diameters for the devices at the respective flow rates for 4 kPa pressure drop

NGI stage	Cut-off diameters for the HandiHaler® at 42.5 l/min [μm]	Cut-off diameters for the GyroHaler® at 78.6 l/min [μm]
Stage 1	9.71	6.97
Stage 2	5.34	3.88
Stage 3	3.35	2.46
Stage 4	1.95	1.46
Stage 5	1.13	0.81
Stage 6	0.68	0.47
Stage 7	0.43	0.28
MOC		

Flow rates were determined using an inhouse-made dose unit sampling apparatus according to the European Pharmacopoeia with a TSI flowmeter, model 4040E (TSI Inc., Shoreview, USA). The devices were tested after three discarded actuations prior to the actual measurement to simulate in-use conditions as the HandiHaler® should be cleaned once monthly [81] and the GyroHaler® cannot be cleaned at all [82]. Each formulation was evaluated in triplicate. The deposited dry powder was dissolved in DMSO and the amount of ITZ at each stage was analyzed via HPLC with the method described above. The fine particle dose (i.e., the API dose with an aerodynamic diameter below 5 μm , FPD), the mass median aerodynamic diameter (aerodynamic diameter that represents the median of a mass-based particle size distribution, MMAD) and the geometric standard deviation (measure for particle size distribution width, GSD) were calculated according to the European Pharmacopoeia. Cumulative masses for S1-MOC were plotted against the stage cut-offs and interpolated to calculate the FPD. Probit-transformed cumulative relative mass fractions were plotted against linearized (log-transformed) stage cut-offs and a linear regression model was used to calculate MMAD and GSD. The fine particle fraction (FPF) was calculated by dividing the FPD by the

dose recovered from the NGI stages including the standard induction port (SIP) and the preseparator (i.e., the emitted dose, ED).

2.2.3 Statistics & Data visualization

Results are expressed as mean \pm one standard deviation (SD), unless otherwise stated.

The effect of process parameters (bead size, temperature, speed) on the nanoparticle size was investigated by a one-way ANOVA with post-hoc Tukey test. A paired-sample t-test was applied for the investigation of storage stability. Comparison of the two selected formulations in terms of particle size, PDI and zeta potential at specific time points was conducted using a two-sample t-test.

Statistical evaluation of the stabilizer concentration for the nanosuspension was done using MODDE® 12.1 software (Sartorius Stedim Biotech GmbH, Göttingen, Germany). A response surface model (RSM) was applied and planned as a full factorial design with two factors (k: SDS and PS80) at three concentration levels. The resulting number of experiments is $3^k = 9$. Three repetitions per experiment resulted in a total number of 27 experiments. As three combinations did not yield a stable suspension only $27 - 3 \cdot 3 = 18$ trials were evaluated.

Two sample t-test with welch correction was applied for reconstitution of ITZ nanoparticles, powder sample characteristics, pressure titration and aerodynamic assessment.

All statistical investigations (except for the assessment of the stabilizer concentration) and data processing were carried out with Origin Pro® 2017 (Origin Lab® Corporation, Northampton, MA, USA). $P < 0.05$ was considered to represent a significant difference.

3 Results & Discussion

3.1 Nanoization of ITZ [83]

For the manufacturing of ITZ nanocrystal suspensions with the ZentriMix, formulation and method development were necessary. The evaluation of process parameters was performed at fixed formulation compositions, except for the smallest bead size. Vice versa, experiments to assess the formulation impact on critical material attributes of the nanosuspension were carried out at fixed process parameters (Table 6). The grinding limit (i.e., particle size that does not decrease with further energy input during milling [84]) was chosen to be the lead parameter. As stabilizers hydroxypropyl cellulose SL (HPC-SL), sodium dodecyl sulfate (SDS) and polysorbate 80 (PS80) were used.

Table 6: Overview of the parameters during evaluation of the milling process

Purpose	Bead size [mm]	Stabilizer concentration w/w	Speed [rpm]	Temperature inside the milling chamber [°C]
Speed evaluation	0.3 – 0.4	0.9 % HPC-SL, 0.14 % SDS, 0.14 % PS80	500	4
			1500	
Temperature evaluation	0.3 – 0.4		1500	4
				-10
Bead size evaluation	0.1 – 0.2	0.9 % HPC-SL, 0.28 % SDS, 0.28 % PS80	1500	4
	0.3 – 0.4	0.9 % HPC-SL, 0.14 % SDS, 0.14 % PS80		
	0.4 – 0.6			
	0.6 – 0.8			
	0.8 – 1.0			
	1.2 – 1.4			
	1.6 – 1.8			
	2.0 – 2.5			
	2.6 – 3.3			
Stabilizer impact on CMA	0.3 – 0.4		1500	4

3.1.1 Stabilizer assessment

To optimize the composition of the suspension binary and ternary stabilizer mixtures of HPC-SL, SDS and PS80 were evaluated by means of a design of experiments approach. A response surface model (RSM) was applied and planned as a full factorial design with two factors (k: SDS and PS80) at three concentration levels. The resulting number of experiments is $3^k = 9$. Three repetitions per experiment resulted in a total number of 27 experiments. As three combinations did not yield a stable suspension only $27 - 3 \times 3 = 18$ trials were evaluated. The trials were conducted with the following parameters: bead size 0.3-0.4 mm, milling temperature 4 °C and centrifugation speed of 1500 rpm.

Table 7: Input variables and response parameters of the statistical evaluation of the stabilizer concentrations after 8 h of milling. HPC-SL concentration was kept constant in all experiments (0.9% (w/w)).

Formulation	Input		Response	
	SDS concentration [%]	PS concentration [%]	Z-Average [nm]	PDI [-]
F1	0	0.14	1443	0.19
			1465	0.30
			1378	0.28
F2	0.07	0.07	4935	0.73
			5447	0.79
			5609	1.00
F3	0.07	0.14	2254	0.29
			2201	0.58
			2464	0.24
F4	0.14	0	221	0.24
			232	0.26
			226	0.31
F5	0.14	0.07	162	0.22
			168	0.22
			167	0.22
F6	0.14	0.14	165	0.23
			165	0.22
			166	0.22

The concentration of HPC-SL was kept constant at 0.9% (w/w) for all formulations (F1 – F6), as previous tests showed no improvement when using higher concentrations. ITZ concentration was also kept constant at 7.4% (w/w) for this evaluation (resulting ITZ concentration after sampling: Subsequent sampling during the analysis led to a decrease in the concentration of ITZ from 9.1% (w/w) to 7.4% (w/w) after 8 h of milling as suspension samples withdrawn were replaced with fresh stabilizer medium).

The input variables and the response parameters are reported in Table 7. The primary response parameter (particle size), as shown in Figure 12, was obtained after 8 hours of milling. The hatched areas represent compositions resulting in inhomogeneous nanosuspensions, which were neglected for statistical evaluations. All suspensions with a SDS concentration of 0.07% (w/w) or less (F1 – F3) were neither homogeneous nor of a particle size below 289 nm.

The smallest Z-average in the steady range of 160 - 170 nm was found with 0.14% (w/w) SDS and 0.07 to 0.14% (w/w) PS80 (F4 - F6).

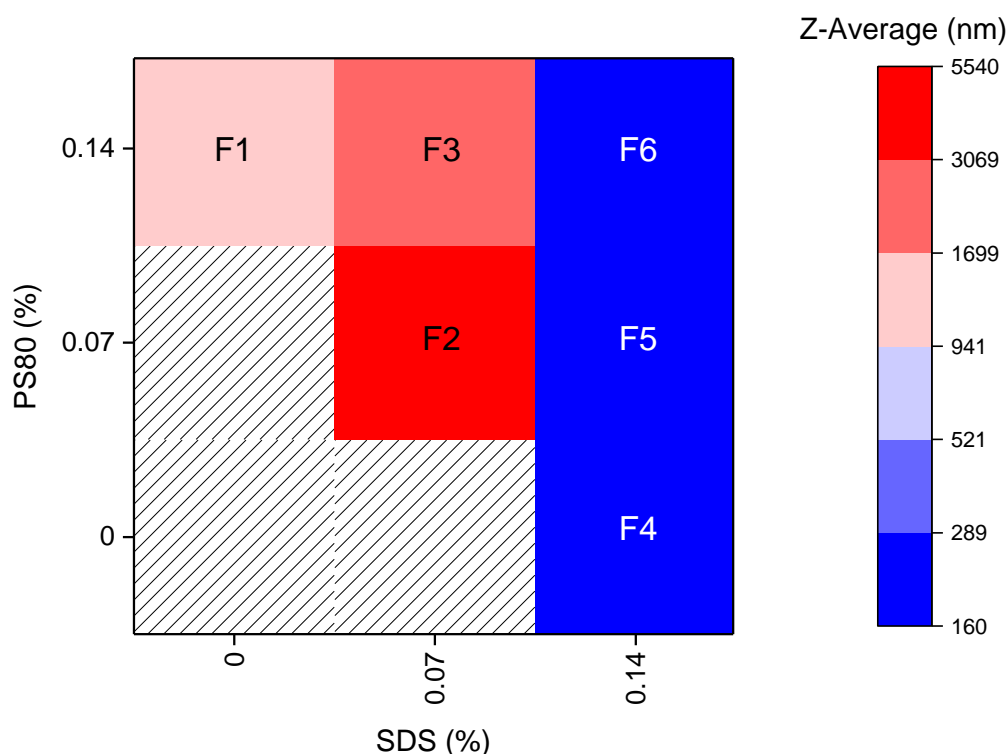


Figure 12: Z-average after 8 h of milling with different stabilizer solutions. Composition is given in % (w/w), and HPC-SL concentration was kept constant at 0.9%. Milling was carried out at 4°C with 1500 rpm and milling beads sized 0.3 – 0.4 mm. Hatched area: No stable nanosuspension was obtained. Value ranges are given as mean of three measurements.

The summary of fit for the model is given in Table 8. Analysis of the coefficients showed that the concentration of SDS had the highest significant impact on the particle size, i.e., lead to a smaller particle size ($p < 0.001$). The PS80 concentration also had a significant effect on the particle size ($p < 0.001$) but to a lower extent when compared to the concentration of SDS.

Table 8: Summary of fit for the applied model. R²: measure of fit, Q²: estimation of precision for the prediction

R ²	R ² Adj.	Q ²	N	Model validity	Reproducibility
0.9953	0.9938	0.99	18	0.94	0.99

Furthermore, a weak interaction between the concentration of SDS and PS was observed. With the unscaled coefficients, the resulting particle size can be calculated depending on the SDS and PS80 concentration, as shown in Equation 8 (applicable in a concentration range of 0 % - 0.14 % each).

$$\begin{aligned} Z\text{-Average} &= K + c_{\text{SDS}} * k_{\text{SDS}} + c_{\text{PS80}} * k_{\text{PS80}} + (c_{\text{SDS}})^2 * k_{\text{SDS*SDS}} + k_{\text{SDS}} * c_{\text{PS80}} * k_{\text{SDS*PS80}} \\ &= 13463.2 + c_{\text{SDS}} * (-51352.6) + c_{\text{PS80}} * (-85962.2) + (c_{\text{SDS}})^2 * (-309054) + c_{\text{SDS}} * c_{\text{PS80}} * 610912 \end{aligned} \quad \text{Eq. (8)}$$

K is a constant, c_{SDS} is the concentration of SDS [% w/w], k_{SDS} is the coefficient for concentration of SDS, c_{PS80} is the concentration of PS80 [% w/w], k_{PS80} is the coefficient for concentration of PS80, $k_{\text{SDS*SDS}}$ is the coefficient for concentration of SDS in a quadratic term and $k_{\text{SDS*PS80}}$ is the coefficient for the interaction between the concentration of SDS and the concentration of PS80.

The SDS concentration had a higher impact on the ITZ particle size than that of PS80. Although PS80, as a non-ionic stabilizer was not as potent as the ionic stabilizer SDS, it nevertheless was still necessary, especially for higher ITZ concentrations (see Figure 47 in the appendix). This could presumably be attributed to the differences in HLB values as also described in literature [85]. PS80 shows a lower HLB value (15) compared to the HLB value of SDS (40) [86].

F6 with 0.9% (w/w) HPC-SL, 0.14% (w/w) SDS and 0.14% (w/w) PS80 was chosen as the optimum composition to stabilize the ITZ nanosuspension and for process evaluation.

3.1.2 Evaluation of process parameters

To determine the most suitable parameters for the manufacturing of a ITZ nanosuspension, the milling temperature, the speed and the diameter of the milling beads were examined.

3.1.2.1 Influence of milling temperature

The effect of the temperature of the grinding chamber, respectively of the vial temperature, can play an important role during the formation of nanoparticles [87] and has not been reported so far in the context of dual centrifugation [71,72]. Lower temperatures (<10 °C in the vial) might be advantageous for very thermolabile APIs but could not be tested with the ZentriMix due to equipment inherent limitations.

Two milling temperatures (set in milling chamber) were tested: 4 °C (which was the manufacturer's recommendation) and -10 °C, which was the lowest temperature supported by the centrifuge. The above-mentioned temperatures were set for the milling chamber whereas the temperatures inside the vials were higher because of the process heat, yet still constant during the milling process; at 25.6 °C ± 0.2 °C for milling at 4 °C and 16.3 °C ± 0.4 °C for milling at the set temperature of -10 °C, respectively. No chemical degradation occurred during milling at 4 °C (determined via HPLC, data not shown). The particle sizes obtained at different vial temperatures were similar with 166 nm ± 1 nm after 3 hours at a vial temperature of approximately 26 °C and 169 nm ± 2 nm for a vial temperature of approximately 16 °C, respectively. In conclusion, no temperature effect was observed for this nanosuspension, therefore 4°C was chosen as milling temperature.

3.1.2.2 Influence of milling speed

In order to evaluate the impact of the milling intensity, the highest and the lowest possible settings for this rotor (500 rpm and 1500 rpm) were tested.

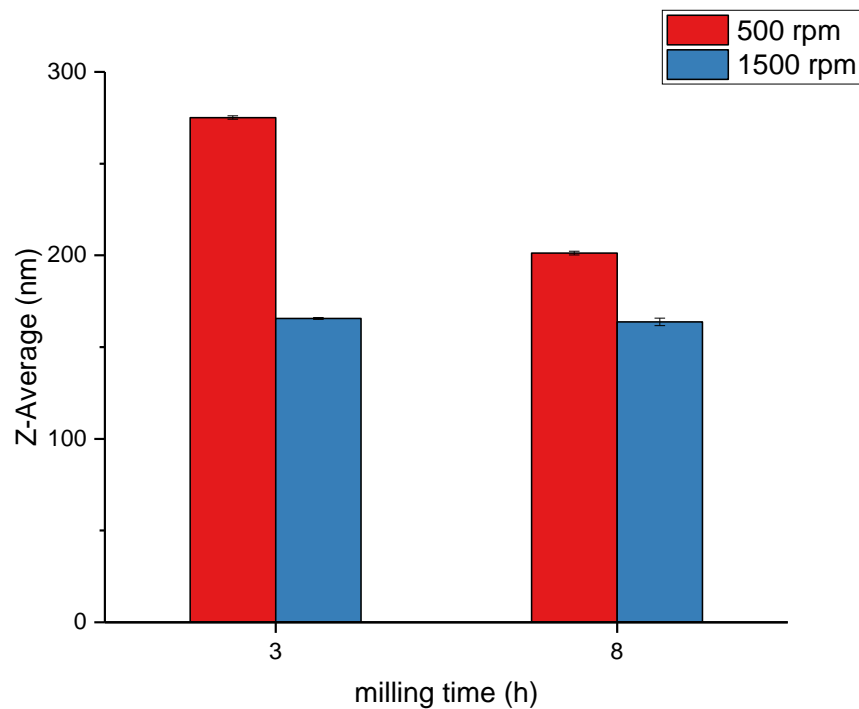


Figure 13: Impact of milling speed on the particle size of the ITZ nanosuspensions. Values are given as mean \pm SD, n = 3.

Using different milling speeds led to different particle sizes, as shown in Figure 13. Milling at 1500 rpm led to significantly lower particles sizes compared to 500 rpm for all investigated process durations ($p < 0.001$). Therefore, milling at 1500 rpm was preferred because of the reduced process time and the smaller Z-average obtained. A significant impact of the milling intensity on the particle size and the grinding limit could be shown: the higher the milling intensity, the earlier the grinding limit was reached.

3.1.2.3 Influence of bead size

The impact of using differently sized beads was evaluated for nine bead diameters, as shown in Table 9.

Table 9: Overview of the bead diameters and theoretical number of 5 g beads, assuming a bead density of 6 g/cm³ and a bead volume 0.83 cm³

Bead diameter [mm]	Theoretical number of beads in 5 g
0.1 – 0.2	471570
0.3 – 0.4	37121
0.4 – 0.6	12732
0.6 – 0.8	4640
0.8 – 1.0	1592
1.2 – 1.4	724
1.6 – 1.8	324
2.0 – 2.5	131
2.6 – 3.3	59

Figure 14 depicts the Z-average of the ITZ nanoparticles generated with different bead diameters as a function of the milling time using 0.14% (w/w) SDS and 0.14% (w/w) PS80, except for bead sizes 0.1 – 0.2 mm (0.28% (w/w) SDS and 0.28% (w/w) PS80)). Milling with all bead sizes led to stable and homogeneous nanosuspensions. The lowest particle size observed after 8 h of milling was directly correlated to the grinding bead diameter. The smallest particle size was achieved with the smallest milling beads (diameter 0.1 - 0.2 mm). However, the smallest beads demanded twice the stabilizer concentration used with larger milling beads to achieve constant particle sizes: 0.28% (w/w) SDS and 0.28% (w/w) PS80 in contrast to 0.14% (w/w) SDS and 0.14% (w/w) PS80 for all other sizes.

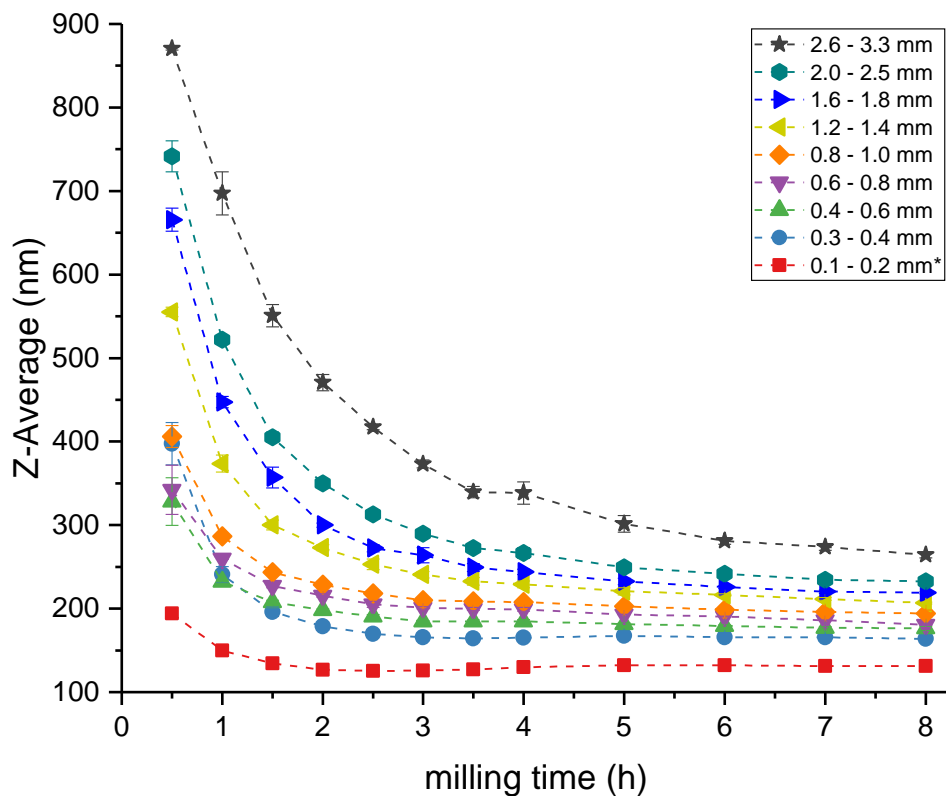


Figure 14: Effect of milling bead size on the ITZ particle size. Values are expressed as mean \pm SD, n = 3. Milling was carried out at 4°C with 1500 rpm. *Bead size 0.1 - 0.2 mm: stabilizer amount had to be changed to 0.9 % HPC-SL, 0.28 % PS and 0.28 % SDS

The largest beads (2.6 - 3.3 mm) led to the nanosuspension with the largest particle size and the highest PDI after 8 hours of milling. All samples showed significantly different particle sizes at the end of the milling process ($p < 0.001$), except for the samples milled with 0.4 - 0.6 mm and 0.6 - 0.8 mm, which showed no significant difference ($p = 0.64$).

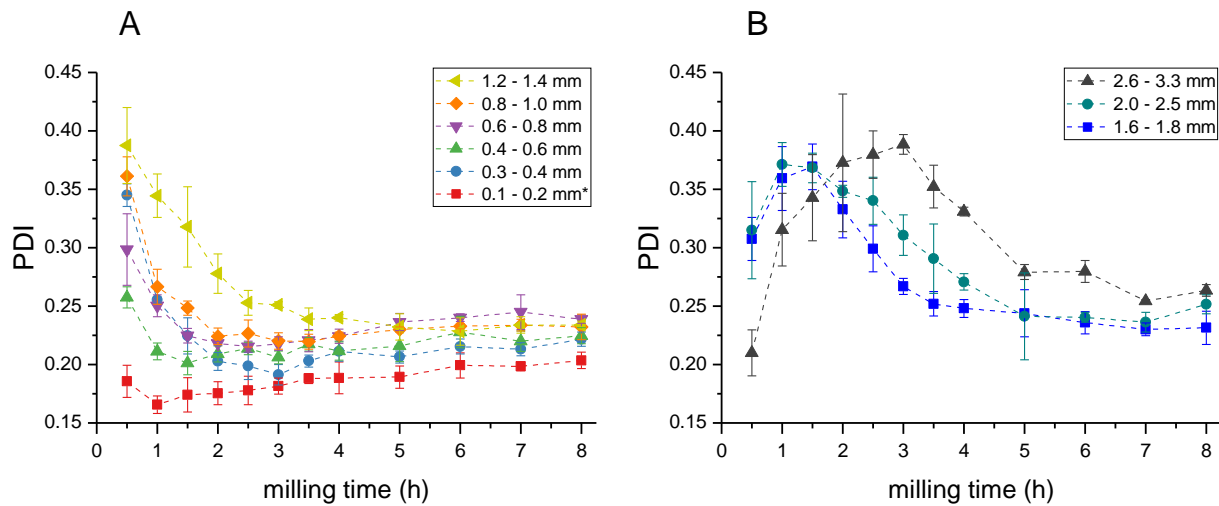


Figure 15: Effect of milling bead size on the polydispersity index (PDI) of ITZ particles (relating to F6). Values are expressed as mean \pm SD, $n = 3$. Milling was carried out at 4°C with 1500 rpm. *Bead size 0.1 - 0.2 mm: stabilizer concentration had to be changed to 0.9% (w/w) HPC-SL, 0.28% (w/w) PS80 and 0.28% (w/w) SDS. Data are shown in two figures (A & B) for better readability.

The PDI of the samples milled with 1.2 - 1.4 mm or smaller beads, decreased at the beginning of the milling process (as shown in Figure 15) and increased only slightly during prolonged milling. On the contrary, milling beads 1.6- 1.8 mm and larger, resulted in an initial increase of the PDI and a subsequent drop at about the same time the minimum particle size was reached.

For the determination of the grinding limit, samples were compared after a milling time of 6 h and 8 h (see Figure 14). In case there was no significant difference, it was assumed that the grinding limit was reached. The particle sizes of the suspensions generated with 0.1 - 0.2 mm to 0.4 - 0.6 mm beads did not change significantly after 6 h (0.1 - 0.2 mm: $p = 0.75$, 0.3 - 0.4 mm: $p = 0.29$, 0.4 - 0.6 mm: $p = 0.19$) and thus the grinding limit was reached. Regarding the suspensions milled with milling bead diameters of 0.6 - 0.8 mm and larger, the grinding limit was not reached within the investigated timeframe ($p < 0.001$, except for 0.8 mm - 1.0 mm: $p = 0.03$ and 2.0 - 2.5 mm: $p = 0.03$). The smallest particle size with the lowest concentration of stabilizers was achieved with the bead size 0.3 - 0.4 mm., which was regarded as optimum and thus these beads were chosen for the following experiments.

The size of the milling beads heavily affected the specific energy input, which determined the degree of comminution (i.e., particle size). The smallest particle size could be obtained by using the smallest milling bead size. However, the smallest obtainable particle size could be only achieved by using a higher stabilizer concentration to avoid agglomeration as smaller particles exhibit a larger specific surface area. The frequency of grinding contacts was highly increased for small milling

beads due to the higher number of beads per volume. This predominates the fact that the energy per contact is lower for smaller beads compared to larger beads [88]. These findings are in agreement with other studies investigating the effect of the milling bead size [87,89–91]. Remarkably, ITZ nanosuspensions with a relatively low particle size could be obtained even with the largest milling beads after 8 hours of milling. This is attributed to the fact that the ZentriMix operates with a much higher specific energy compared to other ball mills and the very long process duration. This assumption is supported by Hagedorn et al. (2019) [72] stating that the specific grinding energy of the ZentriMix is comparable or even higher to conventional agitator ball mills.

3.1.3 Impact of stabilizer concentration on critical material attributes

A comparison of F6 vs. F2 was performed to investigate the impact of the stabilizer concentration on the critical material attributes. F2 was chosen as this was the formulation with the lowest stabilizer concentration that resulted in a homogeneous suspension with the largest particle size after 8 hours of milling and F6 as the formulation with a stable grinding limit and the smallest PDI with a stabilizer concentration as low as possible. All runs were carried out at a milling temperature of 4°C with a speed of 1500 rpm and a milling bead size of 0.3–0.4 mm.

3.1.3.1 Particle size, zeta potential, PDI

Figure 16 displays the Z-average (A), the PDI (B) and the zeta potential (C) for both formulations in relation to the milling time. Comparing formulation F2 milled for 2.5 h and 8 h, respectively, showed that all parameters recorded were significantly different: After the first 2.5 h of milling, the particle size decreased and increased afterwards with no grinding limit to be reached ($p < 0.001$). The zeta potential magnitude increased after milling for 2.5 hours of milling and decreased significantly afterwards. After a process time of 2.5 h the PDI increased after milling for 8 h ($p < 0.001$). On the contrary, the particle size of formulation F6 remained constant after 3 h of milling thus grinding limit of this formulation was reached. The PDI exhibited a slight but statistically significant increase after 3 h and 8 h of milling ($p = 0.01$), respectively. This was in correspondence with the decrease in zeta potential magnitude after 8 h ($p = 0.01$).

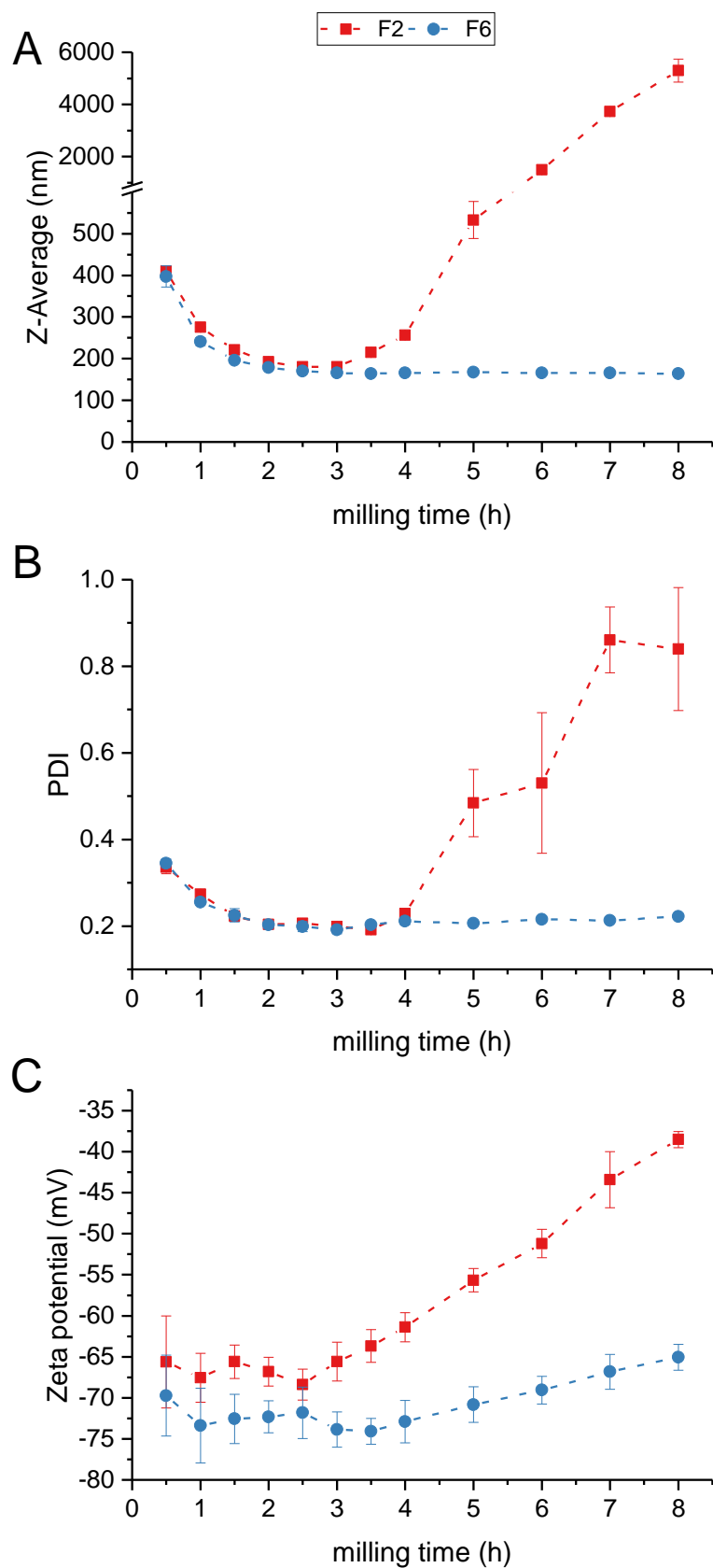


Figure 16: Z-Average (A), PDI (B) and zeta potential (C) of F2 (red squares) and F6 (blue dots) in relation to the milling time. Milling was carried out at 4°C with 1500 rpm and milling beads sized 0.3 – 0.4 mm. Values expressed as mean \pm SD, n = 3

An increase in particle size for formulation F2 throughout 8 hours of milling could be shown, which is accompanied by an increase in PDI. The zeta potential magnitude decreased and implies an only moderately to insufficiently stabilized nanosuspension [92], as the solid-liquid interfacial area increases with increased milling time resulting in increased Gibbs free energy and a thermodynamically unstable suspension [93]. If the stabilizer concentration is insufficient, van der Waals attraction may overcome repulsive forces of stabilizers and will lead to agglomeration. Crystal growth has also been reported as reason for a particle size increase during or immediately after milling [94]. It can be excluded in this case as progressive agglomeration could be shown over time. This observation was supported by SEM images (see 3.1.3.3) and by the fact that a much higher SDS and PS80 concentration was needed to prevent agglomeration for the smallest ITZ particles exhibiting the highest surface area (see 3.1.2.3). To gain further insight into the solid-state properties of F2 and F6, XRPD analysis was performed.

3.1.3.2 Solid-state

Figure 17 illustrates the XRPD pattern of formulation F2. The unprocessed ITZ suspension showed distinct peaks of ITZ, which are similar to the reference pattern of ITZ bulk material. A reduction in peak intensity as well as peak broadening occurred during the milling process and was observed starting from 0.5 hours of milling. After 6 h of milling, the peaks indicating crystalline structures were no longer evident. As an example, the signal-to noise ratio of the peak at 23.56 ° decreased from 2 after 0.5 h towards 1 after 8 h of milling.

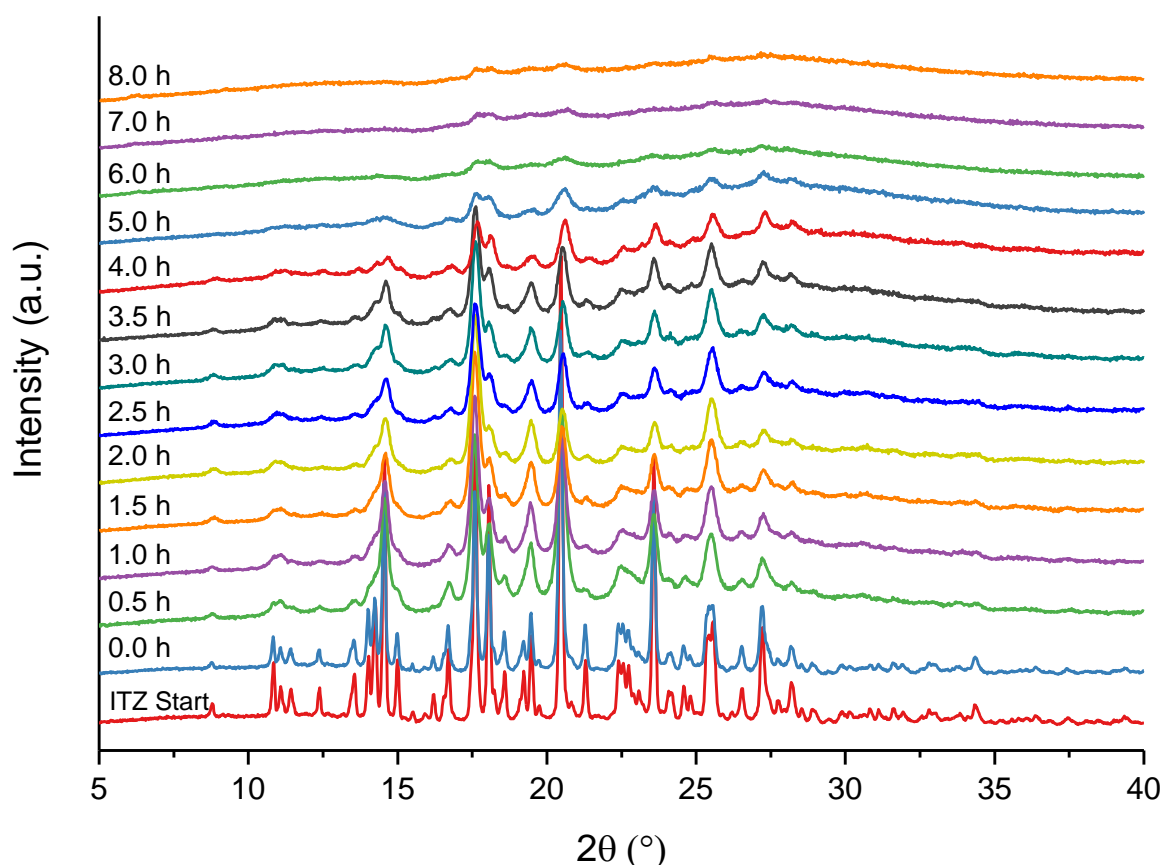


Figure 17: XRPD pattern of F2 in relation to grinding time. Milling was carried out at 4°C with 1500 rpm and milling beads sized 0.3 – 0.4 mm. ITZ Start: starting material of ITZ. Plots are shifted for a better illustration.

It is well known that the milling process may impact the solid-state characteristics of an API [95]. Particles are exposed to a very high energy during milling, which can lead to plastic deformation, defects in the crystal structure (or on the surface), and the creation of (amorphous) areas of high-energy on a crystal, also known as mechanochemical activation [87,96]. In general, reducing the particle size can result in XRPD peak broadening and halo formation, due to loss of long-range crystalline order but without complete transition to an amorphous form [97]. The reduced peak intensity in case of formulation F2 indicated amorphization. The XRPD pattern of the 8 h milled sample showed no complete amorphization as there are still crystal peaks evident, however the content of amorphous ITZ seemed to be quite high. Complete amorphization might have occurred during further milling. The XRPD findings are in agreement with DSC studies for this formulation (see Figure 19).

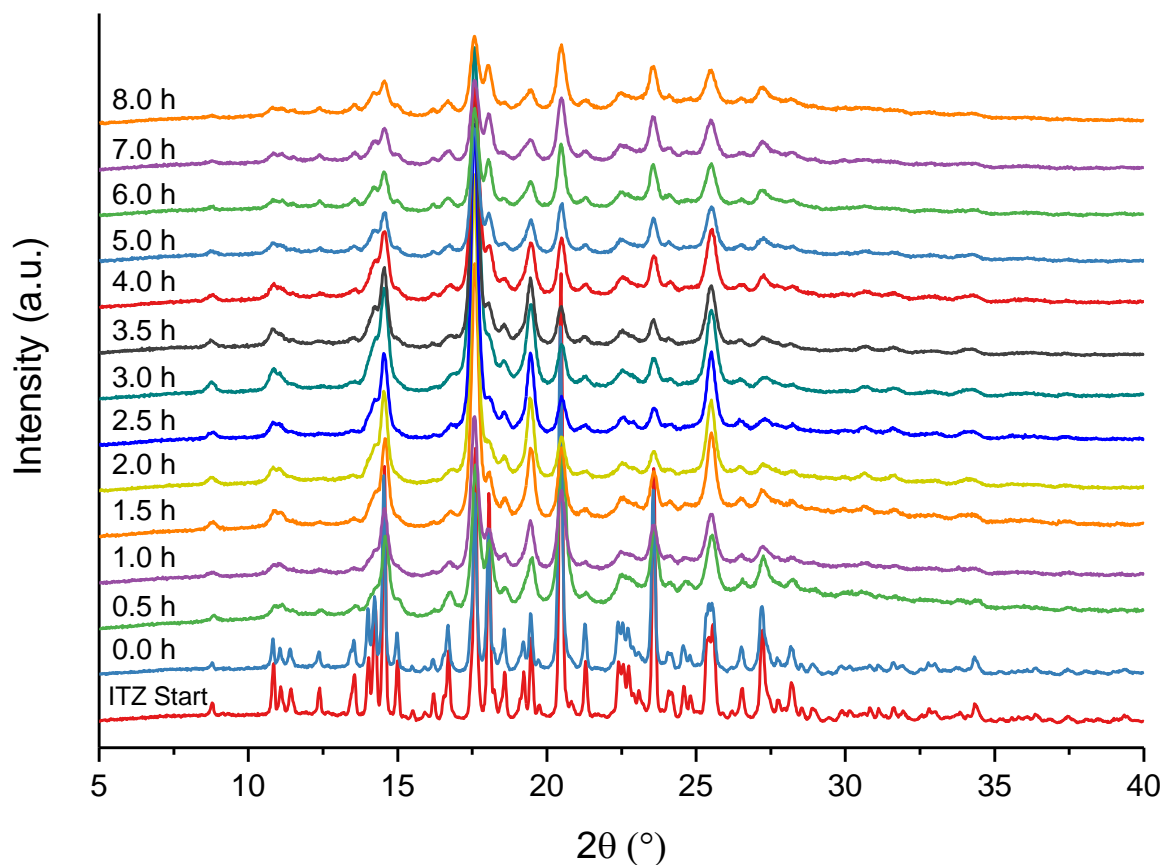


Figure 18: XRPD pattern of F6 in relation to grinding time. Milling was carried out at 4°C with 1500 rpm and milling beads sized 0.3 – 0.4 mm. ITZ Start: starting material of ITZ. Plots are shifted for a better illustration.

Figure 18 depicts the XRPD patterns of formulation F6. The unprocessed formulation showed similar peaks to the ITZ starting material. However, formulation F6 also exhibited a reduction in peak intensity as well as peak broadening after 0.5 hours of milling. In contrast to formulation F2, the peak intensity did not decrease during the milling process to a similar extent: The signal noise ratio of the peak at 23.56° stayed constant at 2 and the peaks remained clearly visible.

The effect of the stabilizer concentration (F2 vs. F6) on the solid-state characteristics had not yet been investigated: In contrast to the observations for F2, no amorphous content was detected during milling of formulation F6. The XRPD pattern of the unprocessed ITZ suspension is similar to the ITZ starting material and to already published reference samples [98]. Furthermore, it could be shown that the XRPD patterns of both formulations show an intensity reduction as well as peak broadening, which probably is related to the smaller particle size or by crystal defects [74].

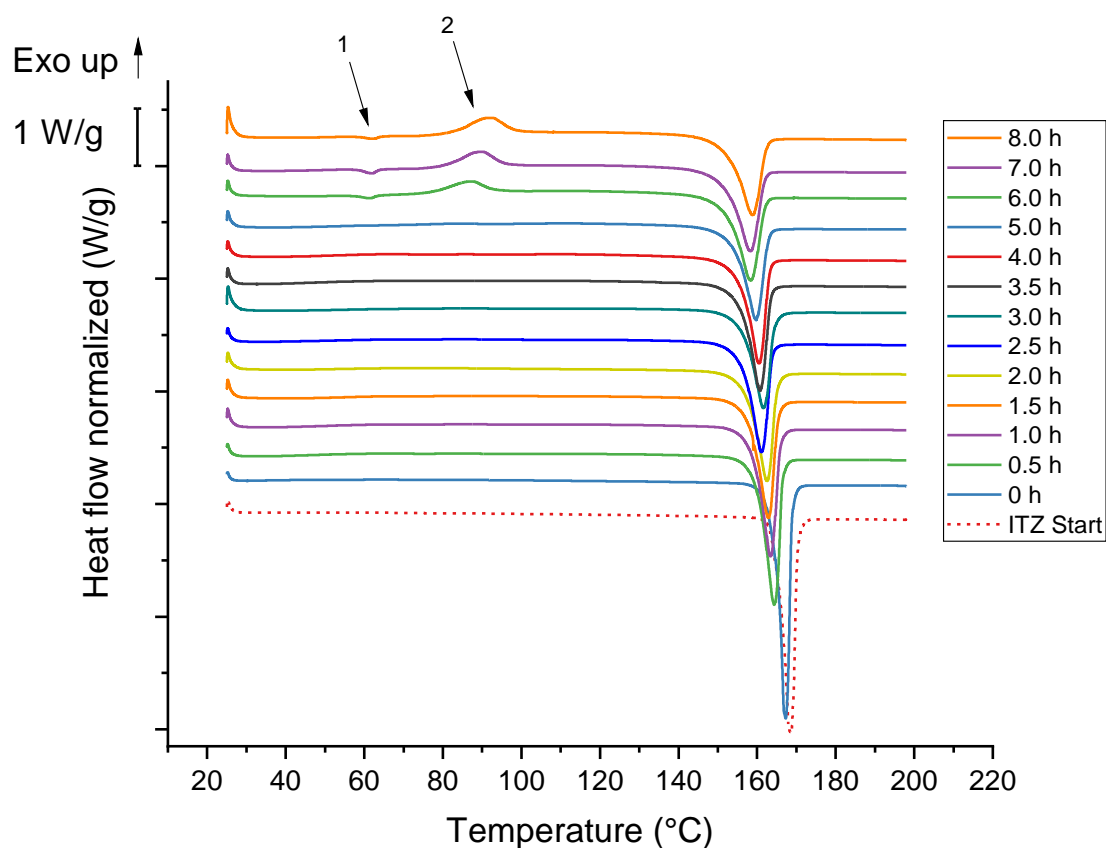


Figure 19: DSC-thermograms of F2 ITZ nanosuspension. Milling was carried out at 4°C with 1500 rpm and milling beads sized 0.3 – 0.4 mm. ITZ Start: starting material of ITZ. Event marked with arrow 1: glass transition and relaxation, marked with arrow 2: recrystallization. Plots are shifted for a better illustration.

Figure 19 shows DSC-thermograms of formulation F2 obtained after the indicated time points during the milling process. As indicated in the figure, an endothermic event at approximately 62°C occurred after 6 hours of milling (marked with arrow 1) which is described in literature as the glass transition temperature of ITZ [99]. Here, the glass transition was probably followed by relaxation due to mechanical stress of the sample. The following exothermic event at 87-90 °C (marked with arrow 2) could be attributed to some recrystallization of amorphous ITZ, as described in [100]. An endothermic peak with an onset temperature of 165 °C observed prior to milling, had a similar onset temperature as the ITZ starting material (166 °C) and is caused by melting of crystalline ITZ which is also reported in literature [100]. The onset of this melting peak was shifted by 13 °C during milling which might be related to crystal lattice defects [87], interaction with the polymer [101], or due to the small particle size of the nanoparticles [74]. The enthalpy of fusion decreased from 80 J/g to 60 J/g after 8 h of milling. Moreover, the enthalpy of the exothermic recrystallization peak increased from 1 J/g after 5 hours to 20 J/g after 8 hours of milling.

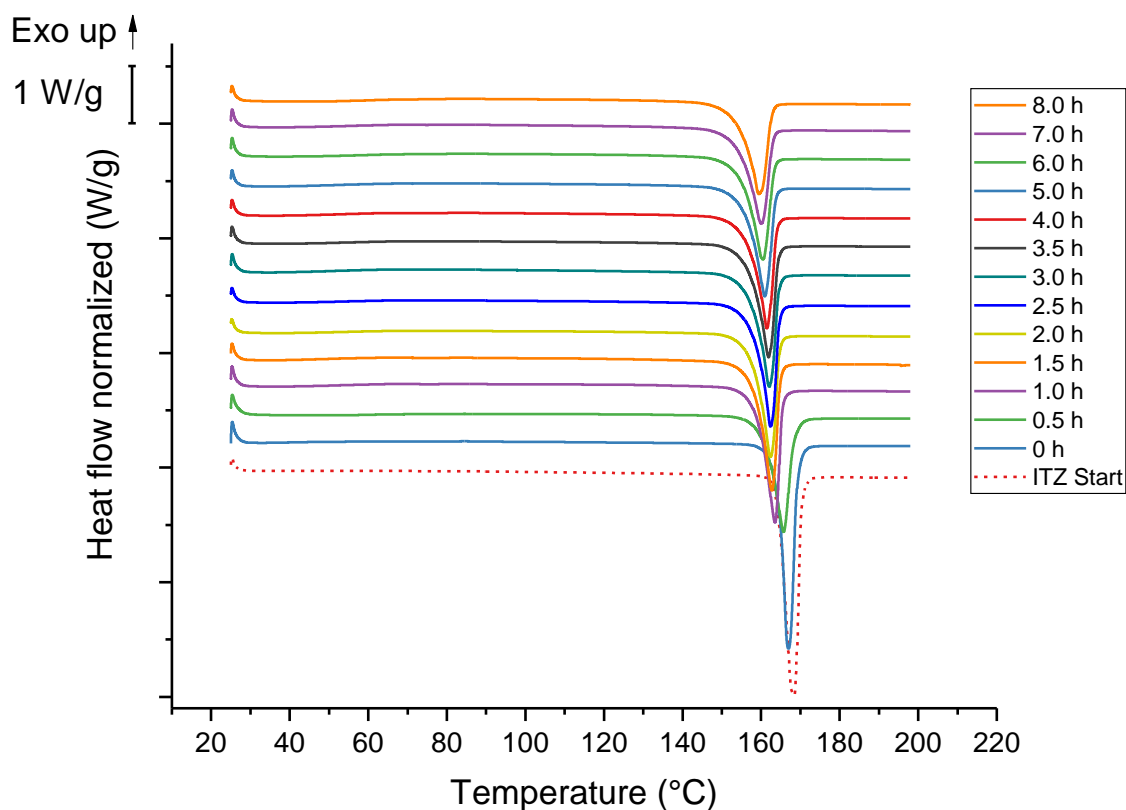


Figure 20: DSC-thermograms of F6 ITZ nanosuspension. Milling was carried out at 4°C with 1500 rpm and milling beads sized 0.3 – 0.4 mm. ITZ Start: starting material of ITZ. Plots are shifted for a better illustration.

Figure 20 displays DSC-thermograms of formulation F6. The ITZ starting material showed an endothermic melting peak of crystalline ITZ with an onset temperature of 165°C, which was also observed for the unprocessed ITZ suspension prior to milling. Formulation F6 showed only this melting event over the whole milling time. The onset was shifted to lower temperatures and the enthalpy decreased by 15 J/g during the milling process. Both observations, a reduction of melting enthalpy and a shift of the onset temperature, were also observed for F2 and are therefore related to the milling process (see above).

The comparison of the solid-state characteristics of formulations F2 and F6 clearly show the impact of the stabilizer concentration on the solid-state of ITZ nanoparticles. Increasing the amount of SDS and PS80 did not only inhibit the agglomeration of ITZ particles but also prevented them from getting amorphous. Kumar et al. (2014) reported an amorphization of the surface caused by milling. Interestingly, this was dependent on the type of polymeric stabilizer [95]. A surface amorphization was also suggested by Sharma et al. (2009) [101]. This effect was found to be related to a molecular

interaction of the stabilizers used with indomethacin and did not occur when using other APIs, e.g., simvastatin. However, the surface amorphization could not be confirmed by DSC measurements of these authors, in contrast to this work. Surface amorphization was also assumed in other study but could not be proven by DSC or XRPD experiments [94]. It can be hypothesized that an increased concentration of surfactants might prevent the potential interaction of ITZ and HPC or reduce the mechanical stress of the ITZ particles resulting in stable crystalline nanoparticles. It is considered, for ITZ, it is critical to understand the solid-state to develop a physically stable nanosuspension.

3.1.3.3 Morphology

In addition, to DSC and XRPD, SEM analysis was conducted. Figure 21 shows SEM images of formulation F2. The ITZ crystals showed a needle-like shape after 2 h of milling. After 4 h slight agglomeration was observed and additional milling led to the formation of large agglomerates, as shown on the image recorded after 8 h of milling.

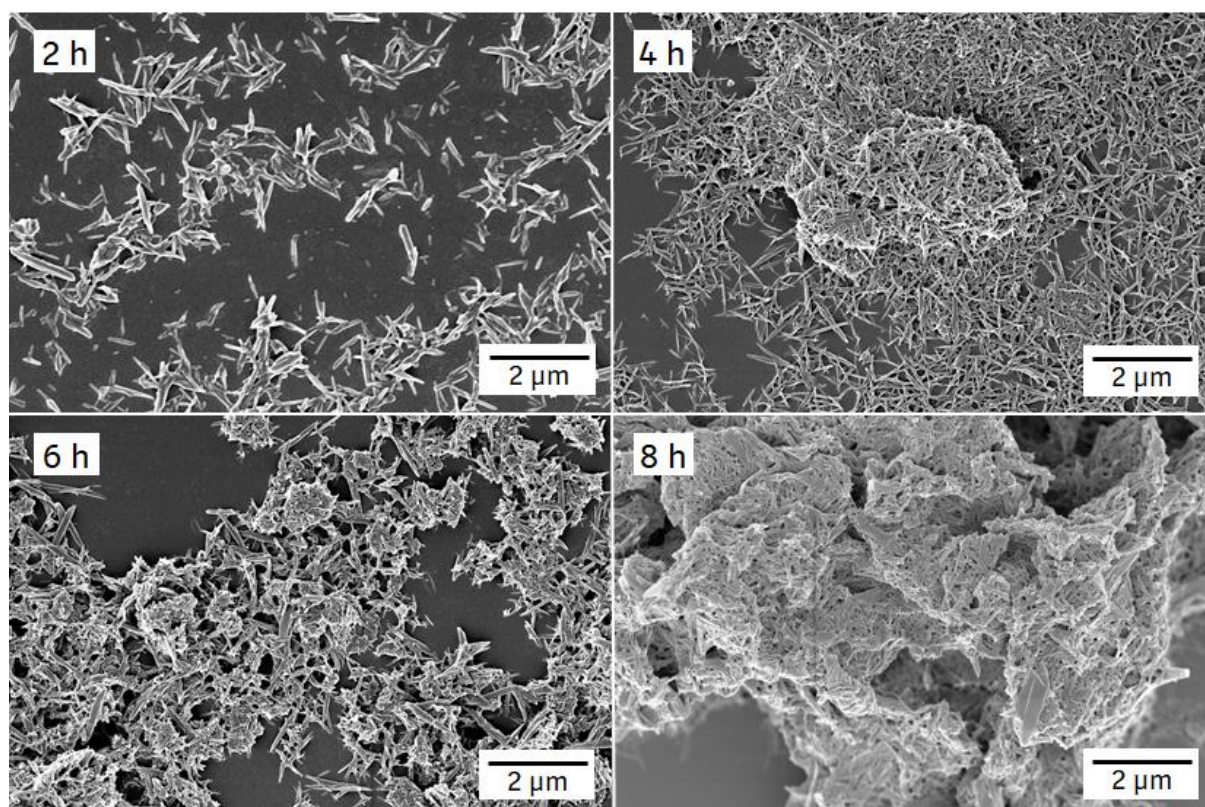


Figure 21: SEM images of F2 ITZ nanosuspension after different milling periods (indicated in the left upper corner of each image). Milling was carried out at 4°C with 1500 rpm and milling beads sized 0.3 – 0.4 mm.

Figure 22 displays SEM images of formulation F6. Unlike formulation F2, the particle size and shape of formulation F6 remained stable during the milling process and no agglomeration was observed.

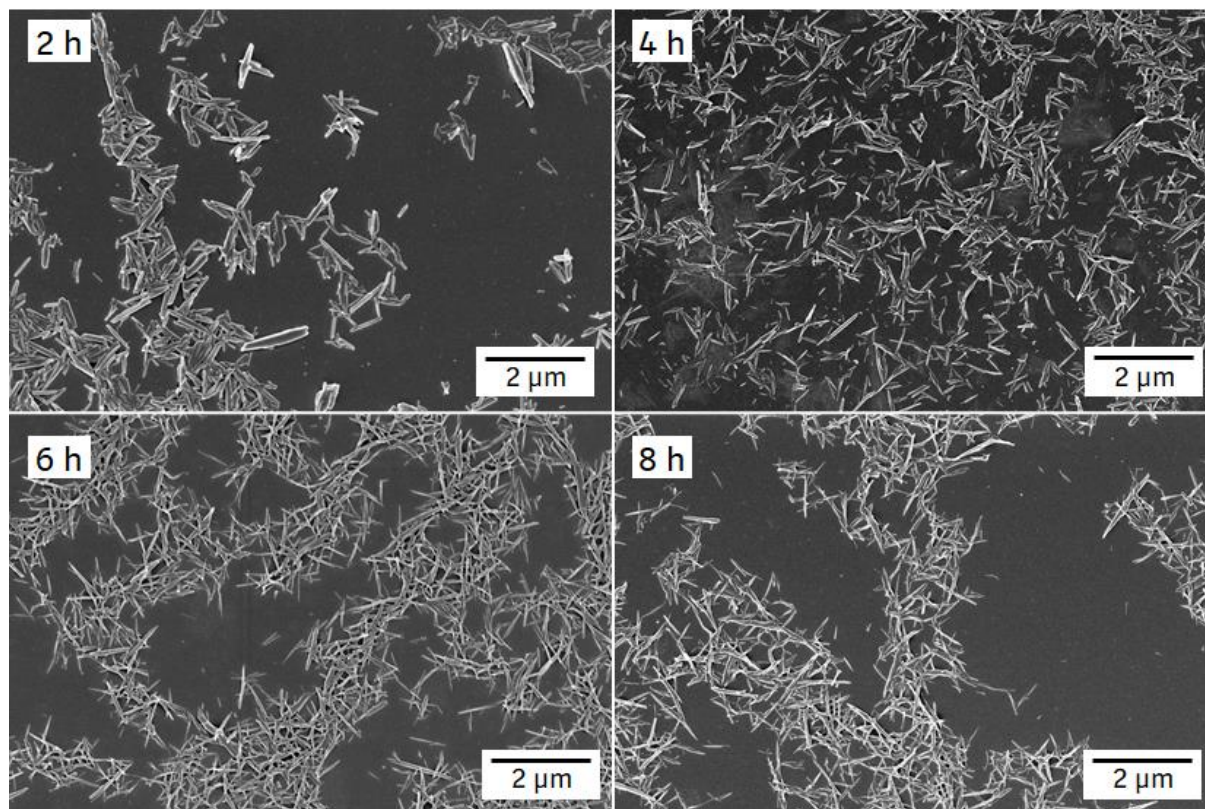


Figure 22: SEM images of F2 ITZ nanosuspension after different milling periods (indicated in the left upper corner of each image). Milling was carried out at 4°C with 1500 rpm and milling beads sized 0.3 – 0.4 mm.

3.1.3.4 Storage stability

The storage stability of the nanosuspensions was investigated for (F2 and F6 (see Table 7) at room temperature ($22\text{ °C} \pm 1\text{ °C}$) and at refrigerated conditions for 7 and 14 days, respectively. In addition, both formulations, milled for 3 hours, were put on long-term stability testing for 70 weeks at refrigerated conditions. Solid-state (XRPD/DSC) was investigated with samples milled for 2, 4, 6 and 8 h and stored at refrigerated conditions. The formulations were selected based on the results of the stabilizer assessment described in 3.1.1. F6 was selected as it yielded a constant particle size during milling while minimizing the concentration of stabilizer. F2 was selected because it was the formulation with the lowest stabilizer concentration that resulted in a homogeneous suspension with the largest particle size.

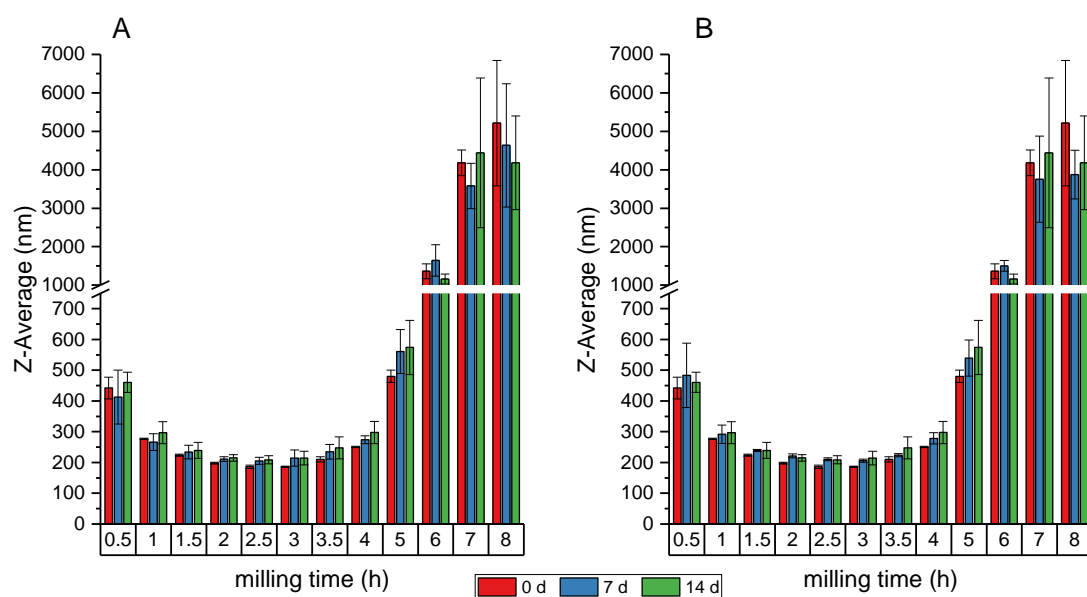


Figure 23: Particle sizes of formulation F2 stored at refrigerated conditions (A) and at room temperature (B) for different storage periods. Values are expressed as mean \pm SD, n = 3. Milling was carried out at 4°C with 1500 rpm and milling beads sized 0.3 – 0.4 mm.

Formulation F2 showed no significant change in particle size between 0, 7 and 14 days of storage (see Figure 23), regardless of the storage conditions and the duration of the milling process applied ($0.07 \leq p \leq 0.98$), even though solid-state changes were observed. Furthermore, an investigation of the behavior of the sample milled for 3 h after long-term (70 weeks) storage showed no significant particle size increase when stored at refrigerated conditions ($p = 0.70$).

However, formulation F6 exhibited a statistically significant but very small increase in particle size after 7 days of storage ($p < 0.001$), regardless of the conditions and milling time applied, but no further significant change occurred after another 7 days of storage ($p = 0.71$ for refrigerated conditions and $p = 0.29$ for room temperature), see Figure 24. Long-term storage investigation over 6 and 70 weeks at refrigerated conditions showed another slight increase between 2 and 6 weeks of storage ($p = 0.05$, rounded) but no further significant change occurred afterwards ($p = 0.08$), also shown in Figure 48 in the appendix.

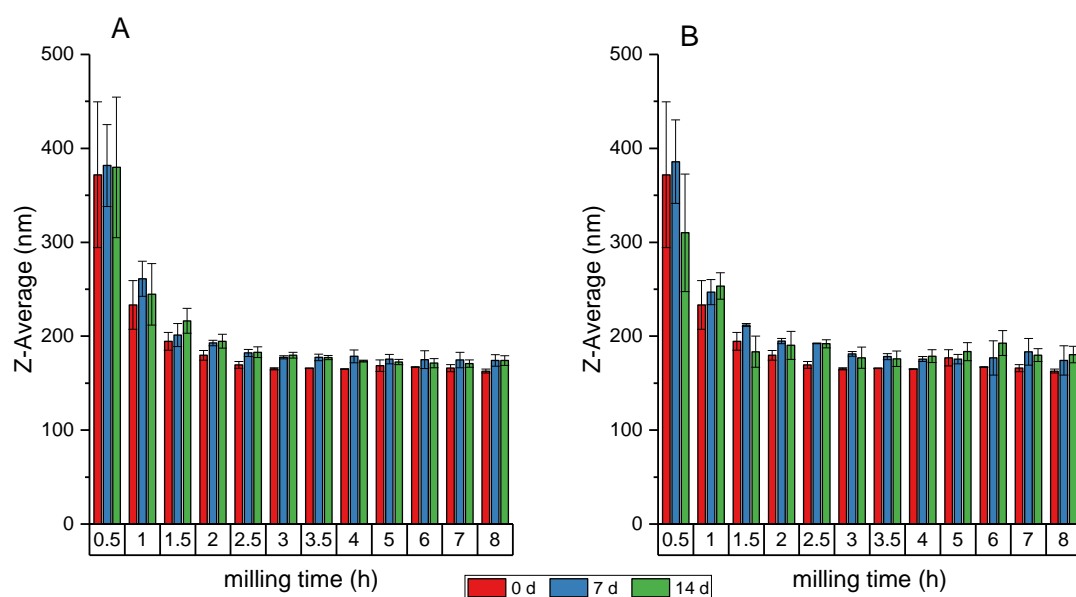


Figure 24: Particle sizes of formulation F6 stored at refrigerated conditions (A) and at room temperature (B) for different storage periods. Values are expressed as mean \pm SD, n = 3. Milling was carried out at 4°C with 1500 rpm and milling beads sized 0.3 – 0.4 mm.

The stabilizer concentration affected storage stability. The particle size significantly increased after 7 days of storage for formulation F6 (0.14% (w/w) SDS, 0.14% (w/w) PS80). A further particle growth was observed after 2 and 6 weeks but not afterwards. The use of high stabilizer concentrations obviously promoted Ostwald ripening during storage, as also already reported by S. Verma et al. (2011) [50]. This group reported a significant increase in particle size upon 0 and 3 days of storage with high concentrations of stabilizer. On the contrary, the stabilizer concentration of formulation F2 was insufficient to prevent agglomeration during the milling process but did not result in particle growth during storage.

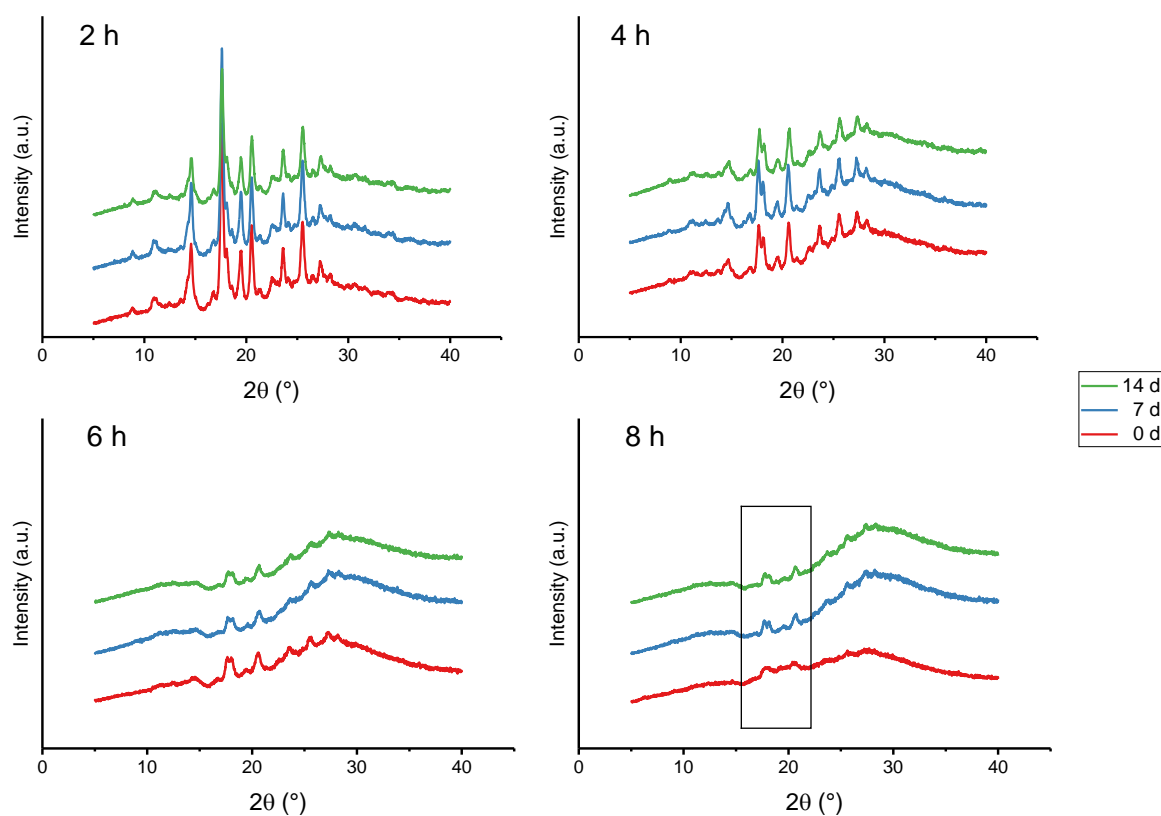


Figure 25: XRPD patterns of F2 ITZ nanosuspension after storage for storage periods of 0, 7, and 14 days at refrigerated conditions. Milling was carried out at 4°C with 1500 rpm and milling beads sized 0.3 – 0.4 mm. Milling time is indicated in the upper left corner of each figure. Marked area: Increase in peak intensity. Plots are shifted for better a illustration.

The solid-state properties of formulation F2 exhibited no change during storage regarding the samples milled for 2 h, 4 h and 6 h of milling, whereas an increase in peak intensity was observed at 17.7°, 18.1° and 20.7° after 7 days of storage of the sample that had been milled for 8 hours (see marked area in Figure 25). Furthermore, a general reduction in peak height during prolonged milling could be found (see also Figure 18).

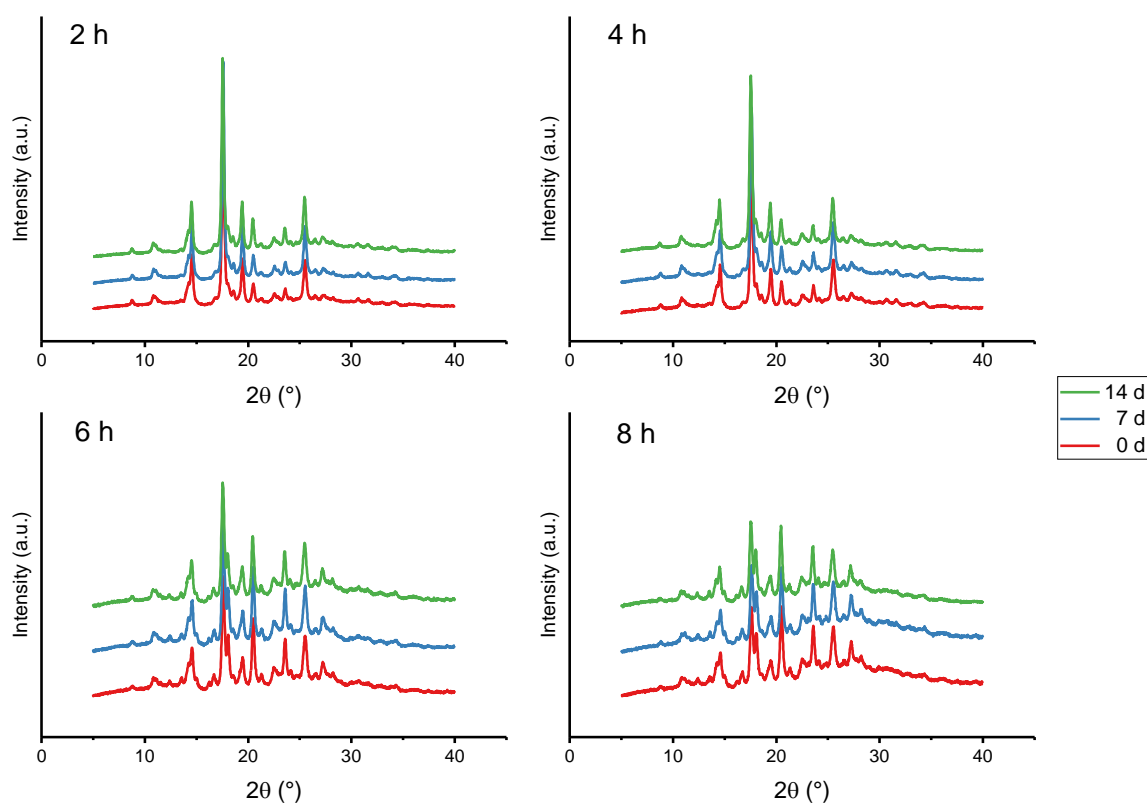


Figure 26: XRPD patterns of the F6 ITZ nanosuspension after storage for storage periods of 0, 7, and 14 days at refrigerated conditions. Milling was carried out at 4°C with 1500 rpm and milling beads sized 0.3 – 0.4 mm. Milling time is indicated in the upper left corner of each figure. Plots are shifted for a better illustration.

Formulation F6 also showed a decrease in peak intensity during prolonged milling (Figure 26). Nevertheless, no qualitative change in solid-state was observed during storage as the samples were crystalline after milling.

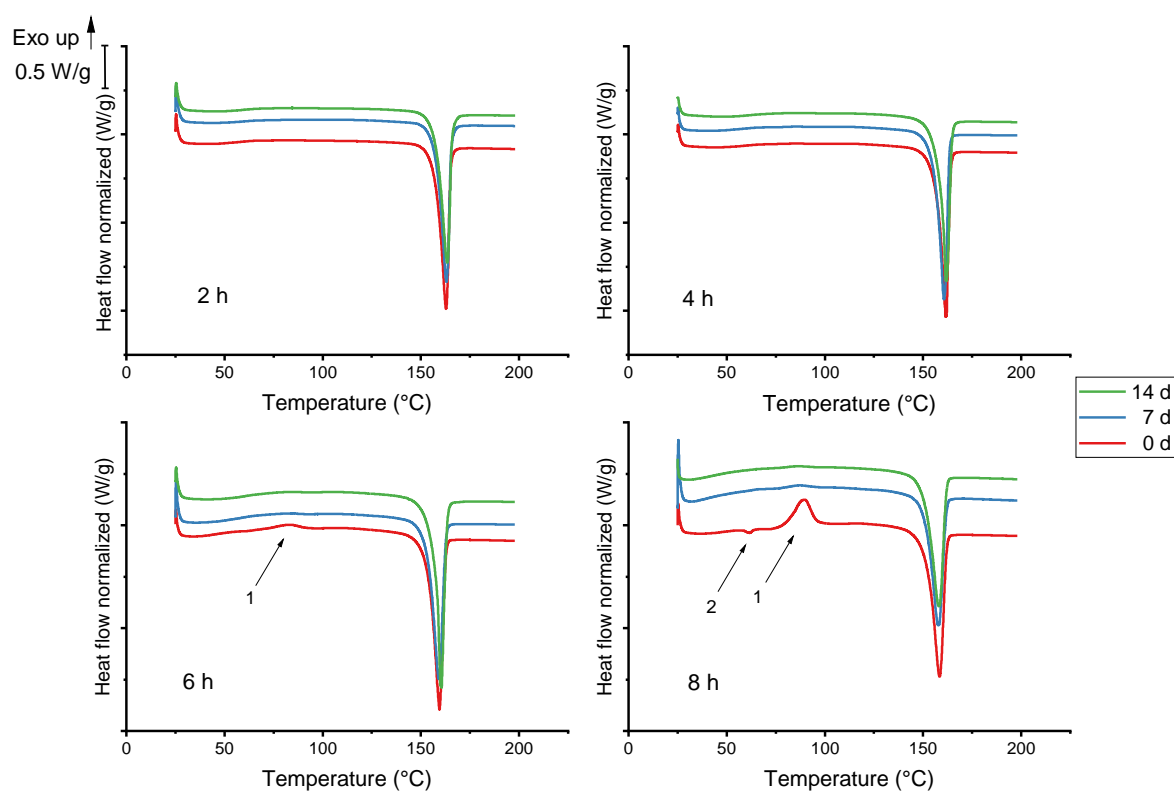


Figure 27: DSC thermograms of F2 ITZ nanosuspension after storage at refrigerated conditions for storage periods of 0, 7, and 14 days. Milling was carried out at 4°C with 1500 rpm and milling beads sized 0.3 – 0.4 mm. Milling time is indicated in the lower left corner of each figure. Event marked with arrow 1: recrystallization, event marked with arrow 2: glass transition. Plots are shifted for a better illustration.

F2 showed differences in the thermogram obtained after 7 days of storage, when compared to the initial thermogram directly after milling. Both the glass transition at about 60 °C after 8 h of milling (event 2 in Figure 27) and recrystallization at 90°C (event 1), that had occurred after milling for at least 6 h, were no longer observed (Figure 27). This in combination with the XRPD data proves that the crystalline fraction increases upon storage.

In contrast to that, the thermal behavior of formulation F6 remained unchanged after storage, as shown in the DSC thermograms (Figure 28).

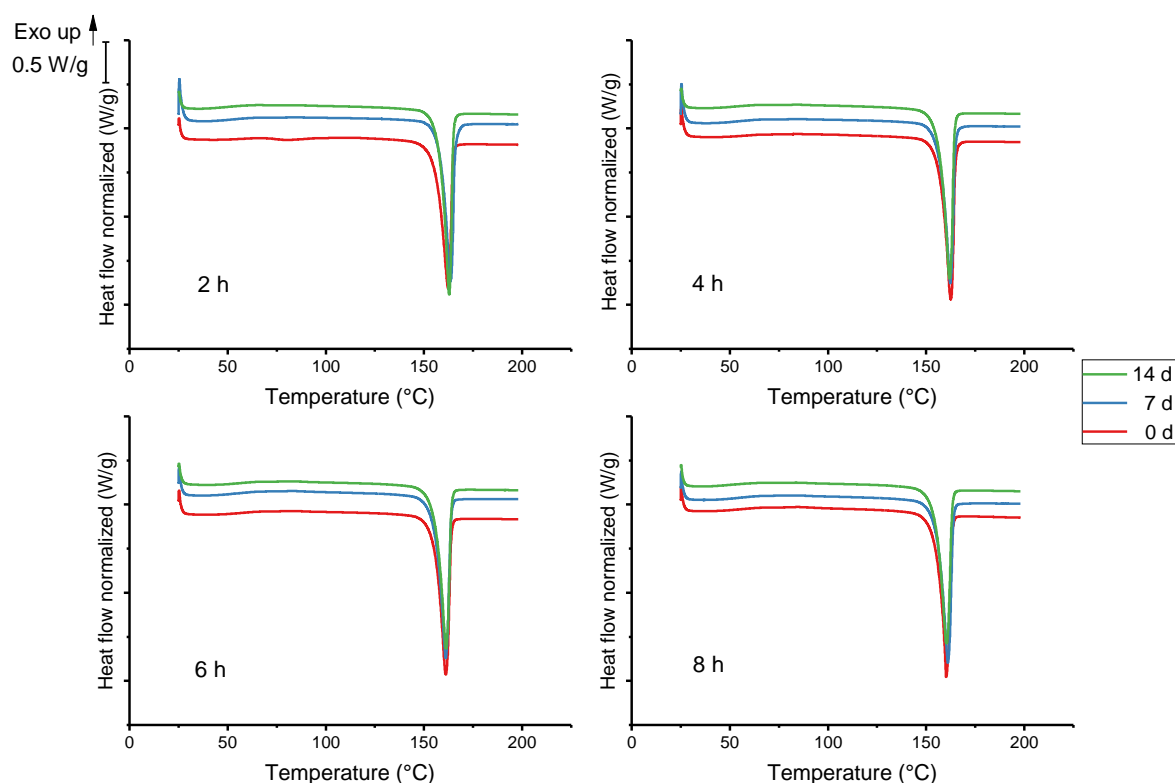


Figure 28: DSC thermograms of F6 ITZ nanosuspension after storage at refrigerated conditions for storage periods of 0, 7, and 14 days. Milling was carried out at 4°C with 1500 rpm and milling beads sized 0.3 – 0.4 mm. Milling time is indicated in the lower left corner of each figure. Plots are shifted for a better illustration.

Investigation of the solid-state of the ITZ nanosuspensions during storage showed recrystallization of amorphous ITZ nanoparticles over time. An intensification of XRPD peak intensity (see Figure 25) and the disappearance of glass transition in DSC experiments (see Figure 27) illustrated this.

3.1.4 Conclusion of the nanoization of ITZ

Media milling using the dual centrifugation principle of the ZentriMix proved to be a useful tool for fast and small-scale formulation development of ITZ nanosuspensions. At maximum speed of 1500 rpm the grinding limit was primarily governed by the milling bead size with 165 – 185 nm for bead sizes between 0.2 mm and 1.00 mm at 3 h of milling and 130 nm for bead sizes smaller than 0.2 mm already after 2 h of milling, which in consequence is recommended as process parameter to target the required particle size of the nanocrystals. Especially for insufficiently stabilized formulations, particle sizes of ITZ nanocrystals increased again after reaching the grinding limit upon further milling, which was accompanied with a similar trend for PDI and zeta potential. At insuffi-

cient protection of the nanocrystals surface with stabilizing excipients continuing mechanical energy intake resulted in amorphization of the particles with pronounced agglomeration resulting in increasing PDI and particle size. Successful electrosteric stabilization, including long term stability, could be obtained with the combination of HPC-SL (0.9% w/w), SDS (0.14% w/w) and PS80 (0.14% w/w) with SDS having the dominant impact on stabilization.

3.2 Spray drying process

The prerequisite for efficient pulmonary deposition of powders are particles with an aerodynamic diameter between 1 and 5 μm , good flowability to ensure homogenous filling and dosing, as well as sufficient de-agglomeration during the inhalation process.

Spray drying was applied to transform the nanosuspension into an inhalable powder as the process enables the formation of tailored particles with defined particle size and morphology. This chapter describes the development of a spray drying process for the ITZ nanosuspensions.

3.2.1 Process development

As discussed in chapter 2, several parameters, e.g., the nozzle gas flow, are known to have an impact on the particle size of spray dried particles. The excipients that are used to stabilize the nanoparticles might alter the surface of the particles, illustrated as a dimpled griseofulvin particles using 2.5% HPC and 0.2% SDS [102] or a rough surface of ITZ particles with spherical morphology as shown for 2.5% HPC and 2% sucrose as matrix former [103]. For material saving purposes, optimization of the process parameters was conducted with an aqueous mannitol solution (MAN) solely (i.e., placebo solution), as it was also used as a matrix former for the spray dried ITZ nanoparticles. The type of matrix former and the concentration used, is known to modify the morphology of spray dried particles: Shetty et al. (2018) showed rough ciprofloxacin nano-in-microparticles when spray dried with sucrose and a smooth surface when using trehalose as matrix former [104]. Torge et al. (2017) found an increased buckling of spray dried PLGA (poly(lactic-co-glycolic acid)) nano-in-microparticles with decreasing mannitol concentration [105]. An overview of the evaluated parameters is given in Table 10.

MAN was added to the stabilizer medium used for the ITZ nanosuspension (as described in chapter 3.1.1) at a ratio of 4:1 (w/w) MAN:stabilizers, which is equivalent to the intermediate ratio of MAN:stabilizers for the ITZ nanosuspension samples to be spray dried using the optimized process parameters. As reference a solution containing solely H_2O and no stabilizers was applied for the second set of experiments. The total solids content was kept constant at 5% w/w.

Table 10: Overview of the spray drying parameters used for process evaluation. Nozzle gas flow rate is given in standard liters per minute (SL/min, flow rate at standard conditions for pressure and temperature: 1 bar and 0°C).

Response parameter	Solid	Medium	Solution composition [%w/w]	Nozzle gas flow rate [SL/min]	Outlet temperature [°C]	Feed rate [g/min]
Droplet size	MAN	H ₂ O + stabilizers	0.7% HPC-SL 0.1% SDS 0.1% PS80 4.1% MAN 95.0% H ₂ O	13, 18, 23, 28, 33	N/A	2.5, 5.0, 10.0
Particle size, solid-state, morphology	MAN	H ₂ O	5.0% MAN 95.0% H ₂ O	23	60, 80, 100	5.0
		H ₂ O + stabilizers	0.7% HPC-SL 0.1% SDS 0.1% PS80 4.1% MAN 95.0% H ₂ O	23	60, 80, 100	5.0

3.2.1.1 Impact of nozzle flow and feed rate on droplet size

The aerodynamic diameter of spray dried particles is affected by several parameters, as described by Vehring (2008) [27]: the major impact is attributed to the feed solution concentration and the diameter of the primary droplets. As the solid concentration in the feed solution was set to 5% w/w to enable a reasonable spray drying process duration, the impact of both the nozzle gas flow and the feed rate on the primary droplet diameter were examined.

The droplet size was determined with a maximum pressure of nozzle gas of 12 bar.

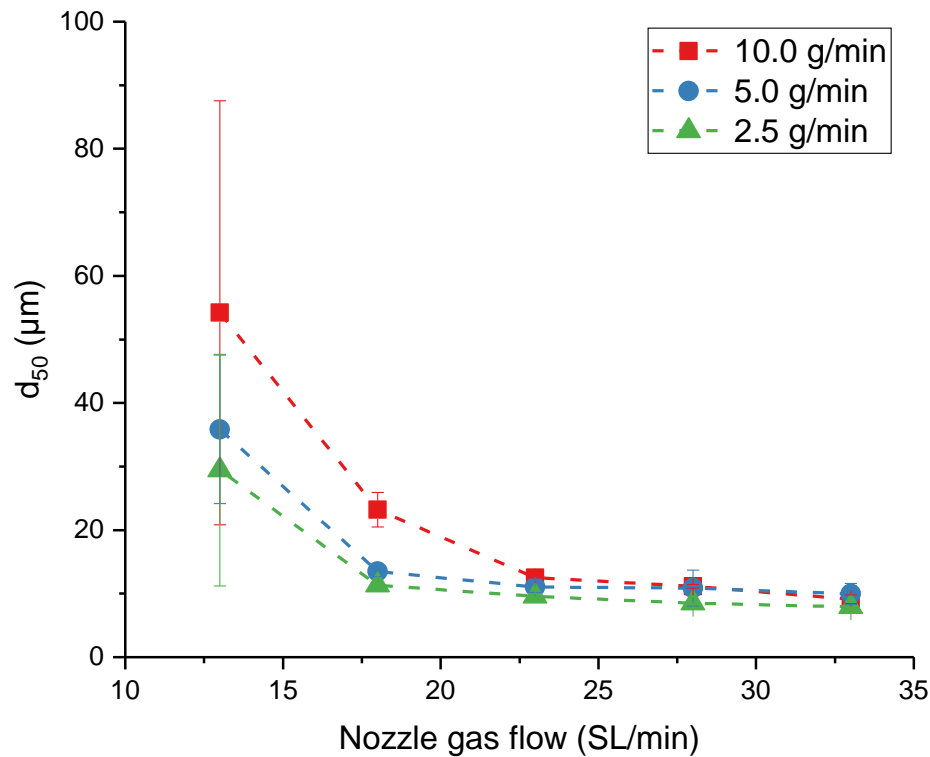


Figure 29: Droplet size of mannitol dissolved in stabilizer medium depending on feed rate and nozzle gas flow. Values are given as mean \pm SD (n = 3), measured by Helos H1411.

The mean droplet diameter (d_{50}) decreased with increasing nozzle gas flow until a constant droplet size was reached (see Figure 29). This droplet size limit was reached for the feed rate 5 g/min at a nozzle gas flow of 23 SL/min. A further increase of the nozzle gas flow did not result in significantly smaller droplet diameters for each flow rate (2.5 g/min: $p = 0.01$, 5 g/min: $p = 0.93$, 10 g/min: $p = 0.01$).

Spray drying was conducted with a maximum pressure of nozzle gas of 6 bar. Due to inherent limitations of the equipment, the nozzle gas flow could not be tested at higher values than 23 SL/min. Therefore, 23 SL/min was chosen for the spray drying process.

The highest feed rate (10 g/min) led to the largest droplet sizes. A feed rate of 5 g/min was chosen for further experiments as this resulted in an optimized particle size while minimizing the process duration. Reducing the feed rate would presumably have led to smaller particles [27,56] but might also negatively impact the yield (of the dried particles) of the spray drying process as the particles would not be collected by the cyclone efficiently. Additionally, this could also be disadvantageous for deposition in the lower respiratory tract as particles might be exhaled if they are too small [32] or show a high cohesion.

In summary, 23 SL/min was chosen for the nozzle gas flow rate to enable the generation of small droplets. The feed rate of 5 g/min was selected as this was the balance between an optimal particle size and a reasonable process duration.

3.2.1.2 Properties of spray dried MAN particles

The impact of the spray drying parameters and excipients (i.e., stabilizers for the nanosuspension) on the physicochemical properties of the spray dried particles was evaluated. Furthermore, the loss on drying and the yield was recorded. The results are given in Table 11 and Figure 30.

Table 11: Overview of the physicochemical properties of the generated MAN particles. Values are given as mean \pm SD. Med: H₂O + stabilizers (simulating stabilizer medium for ITZ nanosuspension)

Sample name	H ₂ O 60 °C	H ₂ O 80 °C	H ₂ O 100 °C	Med 60 °C	Med 80 °C	Med 100 °C
Medium	H₂O			H₂O + stabilizers		
T_{out} [°C]	60	80	100	60	80	100
particle density [g/cm ³] (n = 10)	1.34 \pm 0.00	1.46 \pm 0.00	1.49 \pm 0.01	1.44 \pm 0.00	1.43 \pm 0.00	1.46 \pm 0.00
bulk density [g/cm ³] (n = 3)	0.21 \pm 0.01	0.24 \pm 0.03	0.26 \pm 0.01	0.16 \pm 0.01	0.21 \pm 0.01	0.20 \pm 0.01
tapped density [g/cm ³] (n = 3)	0.32 \pm 0.01	0.36 \pm 0.01	0.40 \pm 0.02	0.22 \pm 0.01	0.30 \pm 0.02	0.26 \pm 0.02
Carr index (n = 3)	34.01 \pm 4.97	33.39 \pm 10.34	35.73 \pm 5.16	29.97 \pm 4.39	28.25 \pm 3.75	22.09 \pm 4.64

With increasing outlet temperatures, both the yield and the LoD decreased for the samples of both media (water and water containing stabilizers), as shown in Figure 30. The reason for the former was most likely related to the strong increase in particle size. The larger spray dried particles showed a larger inertia and worse transportation in the process gas and were not efficiently deposited in the sample collection glass of the spray dryer. Instead, they deposited in the drying chamber and mostly did not reach the cyclone. The higher the outlet temperature the lower was the resulting LoD as the product temperature was also increased (see also chapter 1.2.5).

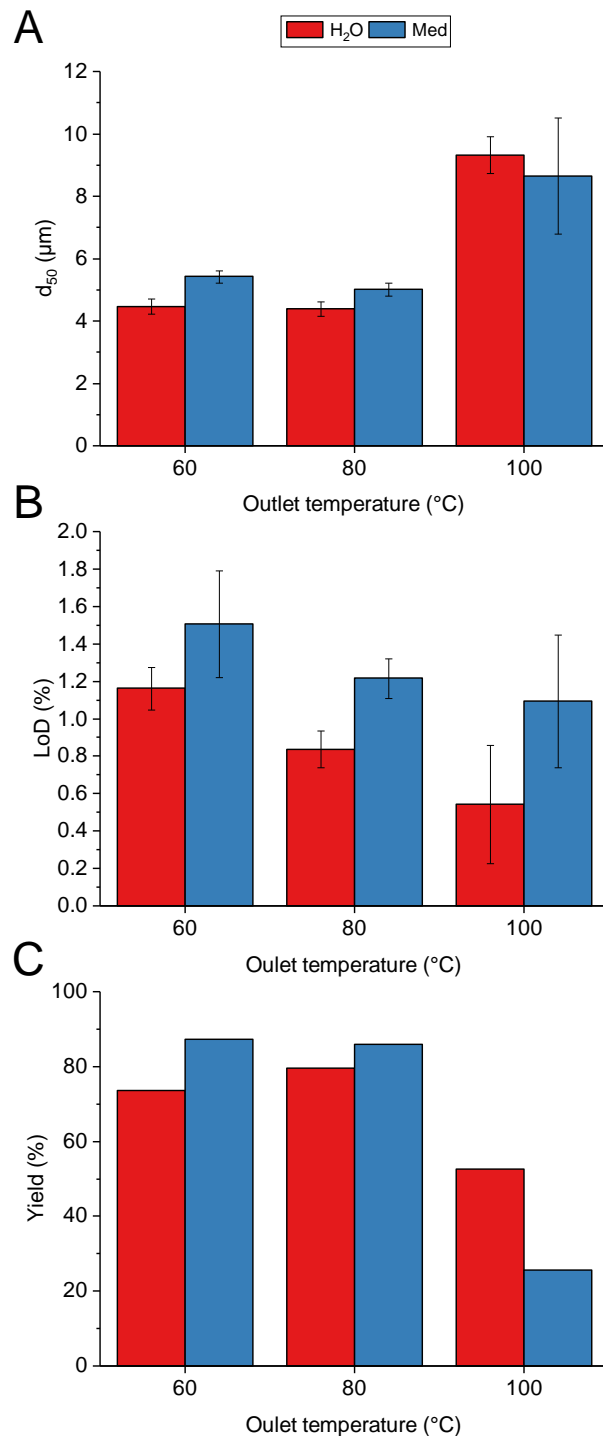


Figure 30: Spray drying results of MAN obtained from water (H₂O) and water with stabilizers (Med). The d₅₀ at 0.1 bar dispersion pressure (A), the LoD (B) and yield (C) are displayed. Values are given as mean ± SD, if applicable.

Regarding the samples obtained with MAN only, the particle density, the bulk density, and the tapped density increased with increasing outlet temperature, which was probably related to the increasing particle size. The value of the Carr index did not change with the outlet temperature: This

indicates very poor flowability for all samples [106–108]. The spray dried MAN particles using water containing stabilizers revealed a slightly different behavior: The sample spray dried at 60 °C showed the lowest bulk- and tapped density, samples Med 80 °C and Med 100 °C were comparable but showed higher values. The particle density was similar for all three samples. Carr index indicated poor flow properties for samples Med 60 °C and Med 80 °C, whereas sample Med 100 °C showed passable flow properties. The latter might be attributed to the larger particle size of this sample. Compared to the samples using water as solvent, the flowability of the samples obtained from water containing stabilizers was improved for outlet temperatures 60 °C and 80 °C, which presumably might be an effect of the stabilizers.

The stabilizers in the medium led to particles with distinctly lower bulk and tapped densities, improved yield (except for the highest outlet temperature) and flowability compared to the samples spray dried using water, which might be attributed to the stabilizers. A high (> 80 °C) outlet temperature resulted in larger particles and a distinctly lower yield.

3.2.1.3 Influence of outlet temperature and stabilizers on modification and morphology of mannitol

Mannitol usually is present in crystalline form after spray drying due to its low glass transition temperature [109]. It is known to have at least three different modifications with varying nomenclature in literature. An overview can be found in [76]. The nomenclature according to Walter-Levy et al. (1968) [110] was applied here, differentiating in α -, β - and δ - forms. Mannitol starting material exhibited β -modification, which is the thermodynamically most stable form [111]. The range between $5^\circ 2\theta$ and $15^\circ 2\theta$ of the XRPD pattern could be used for differentiation within polymorphic forms.

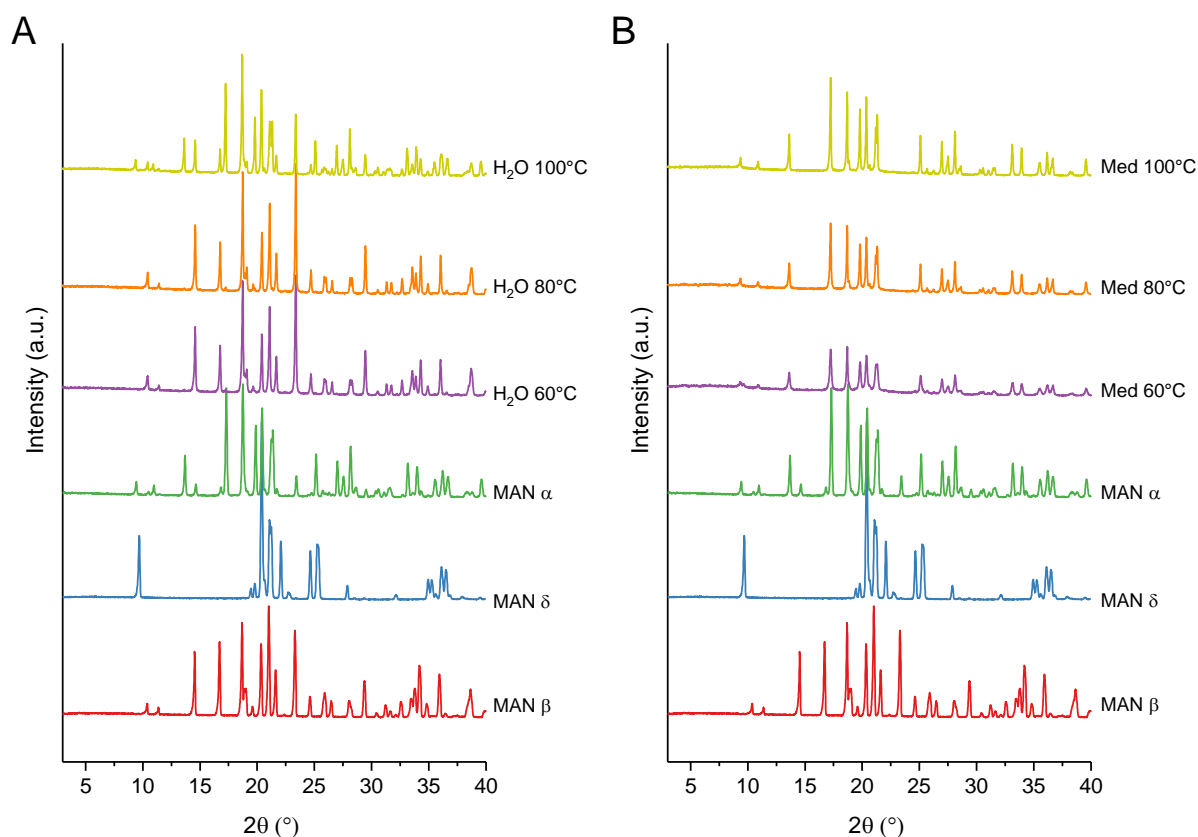


Figure 31: XRPD patterns of mannitol powders spray dried at different outlet temperatures, (A) using water, (B) using stabilizer medium. MAN α : α -modification of mannitol. MAN β : β -modification of mannitol. MAN δ : δ -modification of mannitol. Plots are shifted for better illustration.

The presence of crystalline mannitol was also given in these experiments, as shown by the distinct reflexes in Figure 31. Spray drying using water resulted in the β -modification for outlet temperatures 60°C and 80°C, identical to the starting material (data not shown). An exception was the sample obtained at the highest outlet temperature of 100°C: The modification obtained after spray drying was α (with traces of β). This finding is in agreement with observations made by Maas et al. (2011), who also found an increasing amount of α -mannitol with rising outlet temperatures [112].

Adding stabilizers to the mannitol solution resulted in a different modification after spray drying. Regardless of the outlet temperature, mannitol occurred in the α -modification, as shown in Figure 31 B. This was most likely related to the HPC: Ito et al. (2016) found a method to manufacture α -mannitol in a spray drying process in the presence of hydrophilic polymers [113]. These polymers (e.g., polyethylene glycol, polyvinylpyrrolidone or cellulose derivatives) enabled the formation of α -mannitol out of an aqueous-organic solution with β -mannitol as starting material. However, the mechanism has not been reported.

In conclusion, both the outlet temperature and the presence of stabilizers have impact on the mannitol modification. With water, the β -form was present at lower outlet temperatures. For the highest outlet temperature of 100°C, the modification changed to the α -form. Using the stabilizer medium, the α -modification was obtained for all outlet temperatures investigated (60 – 100°C).

In addition to the findings discussed in the previous chapter, the outlet temperature and the use of stabilizers had an impact on the morphology of the spray dried particles (see Figure 32) as well.

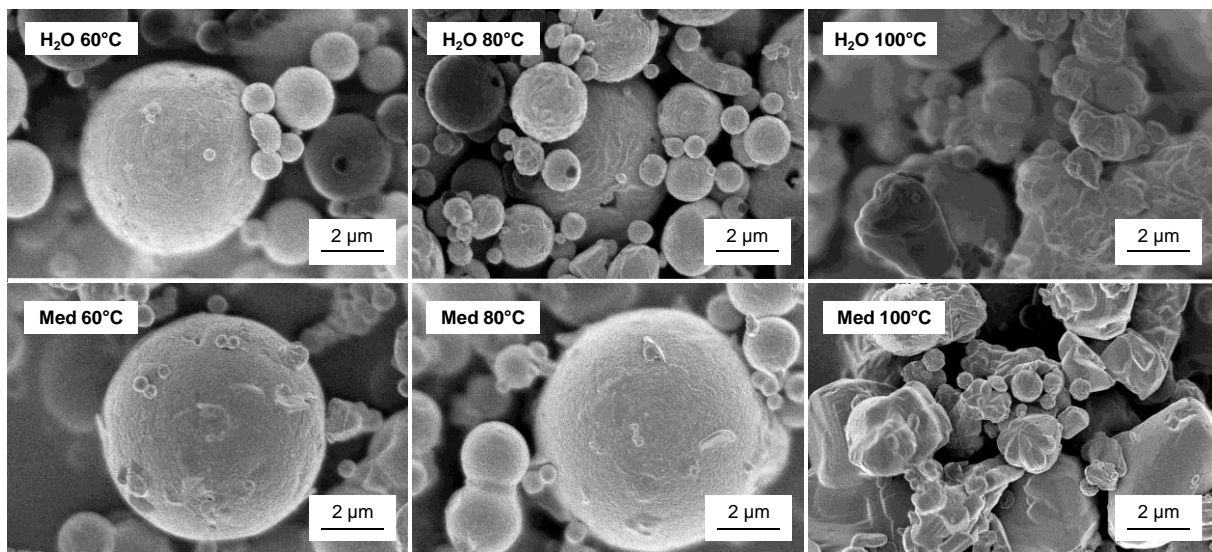


Figure 32: SEM images of MAN samples spray dried at different outlet temperatures without (sample named H₂O, first row) and with stabilizers (sample named Med, second row)

When spray dried out of water only, the MAN particles were of spherical morphology but with both, smooth and rough surfaces. Surface roughness increased from 60 °C outlet temperature to 80 °C outlet temperature. The intensification of surface roughness with higher outlet temperatures has also been described in literature [60,112,114]. However, as this observation was made by the authors only for larger particles at higher outlet temperatures, it obviously seems to be also applicable for smaller droplets with a lower volume due to an increased inner pressure. The authors of the aforementioned literature explained the difference in surface roughness by an altered crystallization kinetics of MAN at higher outlet temperatures, without elucidating the mechanism detailly.

Different theories to explain the increase in surface roughness and particle size observed when spray drying at outlet temperatures of 100 °C or higher can be postulated. One hypothesis involves sintering of the particles during the spray drying process. Solid bridges resulting in larger, aggregated particles might be formed. Another hypothesis is that large, hollow particles with an unstable

crust were initially obtained during spray drying and subsequently fragmented upon separation from the air stream in the cyclone separator. This hypothesis is supported by the finding that many particles from the dried product apparently were fragmented during the process. A third hypothesis corresponding with observations reported in [111] e.g., involves an altered crystallization behavior of MAN leading to large particles with a rough surface. The first hypothesis seems to be most likely assessing observations made on SEM images in combination with the particle size distribution of the product. Further investigation on this topic to elucidate this mechanism would be necessary but is out of scope of this work.

Samples Med 60 °C and Med 80 °C were similar with regard to their morphology and showed a spherical shape with a quite smooth surface. A reason could be the impact of the stabilizers on the crystallization process of MAN hence no larger crystals (which were observed at the surface of sample H₂O 80°C) were formed at an outlet temperature of 80 °C. At the highest outlet temperature of 100 °C non-spherical compact particles with a rough surface were found for both solvents. This was accompanied by an increase in particle size. The possible reasons for this observation have been described above.

Some particles with a hole in the shell are visible in Figure 32. The evaporating solvent escaped from the inside of the droplet through the solid shell, which was already built during the drying process on the droplet's surface, and caused this "blow-hole", as also explained by Maas et al. (2011) [112].

Overall, the outlet temperature highly affected the morphology of the spray dried particles, resulting in a rougher surface for H₂O 80°C compared to H₂O 60 °C. At an outlet temperature of 100 °C, the particles were distinctly larger and lost their spherical shape, which presumably could be attributed to sintered and agglomerated MAN particles. This effect was independent of the presence of stabilizers. However, the stabilizers impacted the size of the MAN crystals as only small crystals were observed for samples Med 60 °C and Med 80 °C leading to quite smooth particles for both samples.

3.2.1.4 Dispersibility of MAN particles by pressure titration

The dispersibility of powder particles (i.e., ability to de-agglomerate in a gas stream) is a prerequisite for efficient deposition in the lower respiratory tract. The geometric mean particle size of the spray dried mannitol samples (d_{50}) was evaluated by laser diffraction in relation to the applied dispersion pressure (so-called pressure titration, see Figure 33).

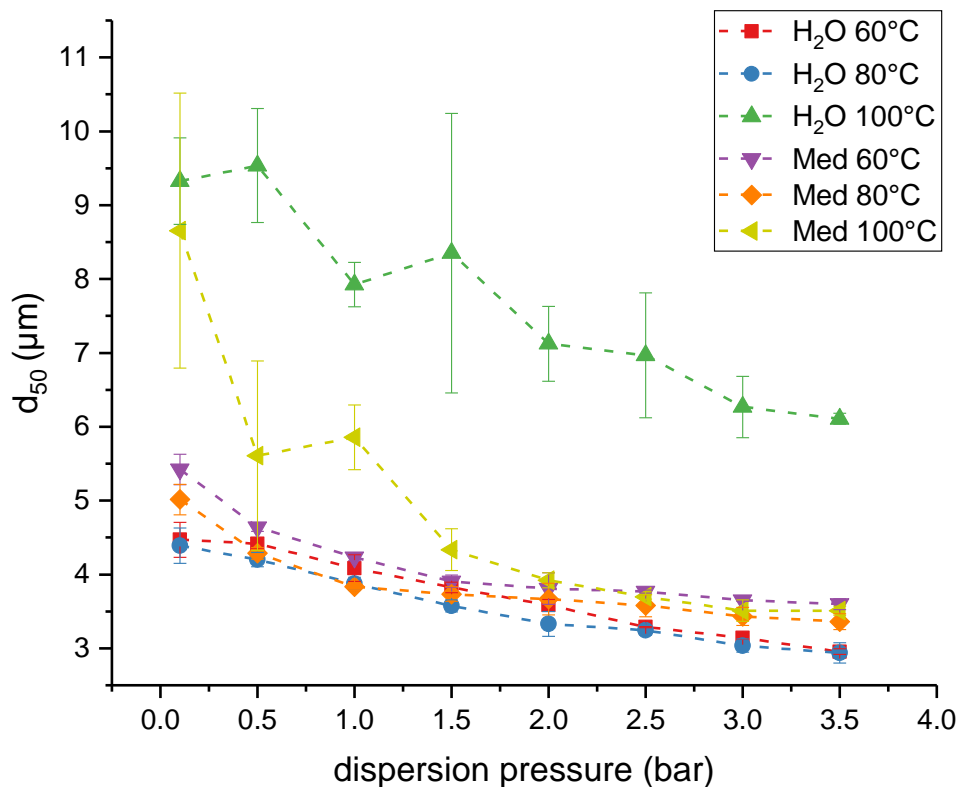


Figure 33: Impact of outlet temperature and stabilizers on the dispersibility of spray dried MAN particles determined by pressure titration. The mean particle size is displayed as a function of the dispersion pressure. Values are given as mean \pm SD (n = 3).

At the highest dispersion pressures, it is assumed that the individual particles are present, whereas at lower pressures agglomerates may exist. With increasing pressure information on the adhesion forces of the agglomerates can be obtained by the magnitude of changes of d_{50} . The higher the particle size reduction with increasing dispersion pressure is, the stronger the cohesion forces. It should be noted that very high dispersion pressures may also negatively impact the particle size as a jet-milling effect may occur [115].

As indicated in the SEM images (see Figure 32) and described in chapter 3.2.1.2, the particles obtained at 100 °C had a distinctly larger particle size compared to the other outlet temperatures, irrespective of the solvent. This difference was statistically significant for the samples obtained using water as solvent ($p = 0.002$). With rising dispersion pressures, the particle sizes of samples Med 100°C and H₂O decreased significantly ($p = 0.04$ for Med 100°C and $p = 0.01$ for H₂O 100°C). Sample Med 100°C showed a sharper decrease which could be an indicator for high cohesion, presumably

related to the rough surface (mechanical interlocking). Sample H₂O 100°C showed the largest particle size even at the highest dispersion pressure, which indicates a larger primary particle size.

At the lowest dispersion pressure, significantly larger particles were obtained for the samples using water with stabilizers compared to the samples with pure MAN, except for the samples spray dried at the highest outlet temperature (60°C: $p = 0.01$, 80°C: $p = 0.03$, 100°C: $p = 0.60$). This was probably related to the viscosity increase due to HPC-SL resulting in a higher droplet diameter as the diffusion coefficient decreases with increasing viscosity leading to higher Peclet numbers [58,62,116]. The reduction of surface tension by the surfactants has only a negligible impact on the droplet size, and consequently on the particle size, compared to the viscosity [56]. Samples obtained at outlet temperatures of 60 °C and 80 °C showed low differences in particle size at 0.1 bar and 3.5 bar (irrespective of the presence of stabilizers), therefore indicating a low agglomeration tendency.

In general, the dispersibility of the spray dried MAN particles was acceptable, except for the samples obtained at 100 °C. There was no sharp decrease in the particle sizes with rising dispersion pressures, regardless of the presence of stabilizing excipients, indicating a low agglomeration tendency.

3.2.2 Manufacturing of nano-in-microparticles

As a next step, the nanosuspension from chapter 3.1 was spray dried. In addition, a suspension of jet-milled ITZ (without bead milling) was spray dried as well, acting as a control. These spray dried samples were compared with pure jet-milled ITZ.



Jet-milling of the ITZ particles resulted in particle sizes of $d_{10} = 0.70 \mu\text{m} \pm 0.01 \mu\text{m}$, $d_{50} = 1.55 \mu\text{m} \pm 0.03 \mu\text{m}$ and $d_{90} = 3.47 \mu\text{m} \pm 0.26 \mu\text{m}$, respectively (particle size was evaluated by laser diffraction with dry dispersion pressure of 3 bars). The Z-averages of the ITZ nanoparticles after nanoization, bead separation and addition of MAN and water, (before spray drying) were in a range of 206 nm to 217 nm with corresponding PDIs of 0.21 to 0.24. The nanosuspensions exhibited a zeta potential in a range of -70 mV to -67 mV which indicated excellent stability [92]. The ITZ concentration of the nanosuspension was determined after milling and bead separation in order to add the correct amount of mannitol. It was also confirmed that nanoization did not result in degradation of ITZ (assay: $100.7\% \pm 2.7\%$).

Spray drying of the nano-in-microparticles was conducted using the optimized process parameters as previously determined, see chapter 3.2.1.1 and 3.2.1.2. The inlet temperature was set to 120 °C

and the feed rate to 5 g/min, which resulted in an outlet temperature of 60 °C. This temperature was chosen to reduce thermal stress for the product and energy saving purposes. Furthermore, it was shown that outlet temperatures exceeding 80 °C led to particles with very low yield and a poor dispersibility.

An overview of the ITZ samples is given in Table 12:

Table 12: Overview of ITZ samples with regard to preparation method. Number in sample name indicates the ITZ:MAN ratio [% w/w]. JM: jet-milled, JM SD: jet-milled and spray dried.

Sample name	Jet Milling (JM)	Nanoization (NS)	Spray drying (SD)	ITZ:MAN ratio w/w [%]	Calc. stabilizer conc. w/w [%]	Schematic illustration
25:75	X	X	X	25:75	5.49	
50:50	X	X	X	50:50	10.05	
75:25	X	X	X	75:25	16.73	
100:0	X	X	X	100:0	18.70	
JM SD	X		X	100:0	18.70	
JM	X			100:0	0.00	

3.2.2.1 Physicochemical characterization

The results of the physicochemical characterization of the different powder samples are shown in Table 13.

Table 13: Characterization results of the nano-in-microparticles, in comparison sample JM SD (jet-milled and spray dried) and sample JM (jet-milled). Number in sample name describes the ratio of ITZ:MAN [%w/w]. Values are expressed as mean \pm SD, if applicable.

Sample	25:75	50:50	75:25	100:0	JM SD	JM
Particle density [g/cm ³] (n = 10)	1.46 \pm 0.00	1.44 \pm 0.00	1.37 \pm 0.00	1.33 \pm 0.00	1.40 \pm 0.00	1.37 \pm 0.01
Bulk density [g/cm ³] (n = 3)	0.24 \pm 0.01	0.22 \pm 0.03	0.22 \pm 0.00	0.18 \pm 0.00	0.12 \pm 0.00	0.16 \pm 0.01
Tapped density [g/cm ³] (n = 3)	0.32 \pm 0.01	0.29 \pm 0.00	0.30 \pm 0.01	0.25 \pm 0.00	0.16 \pm 0.00	0.22 \pm 0.01
Carr Index (n = 3)	24.02 \pm 2.05	29.16 \pm 0.99	27.34 \pm 0.58	26.51 \pm 1.32	26.80 \pm 3.03	28.36 \pm 2.38
d₅₀ [μm] (n = 3, at 0.1 bars)	3.88 \pm 0.03	4.29 \pm 0.06	3.85 \pm 0.04	3.74 \pm 0.03	6.69 \pm 0.31	5.02 \pm 0.50
LoD [%] (n = 3)	0.91 \pm 0.21	1.54 \pm 0.41	1.44 \pm 0.41	1.16 \pm 0.04	1.29 \pm 0.58	-
Yield [%]	91.43	88.23	97.86	93.29	82.79	-
Theoretical API content [%]	23.63	44.98	62.41	81.30	81.30	100
Measured API content [%] (n = 3)	23.70 \pm 0.94	43.84 \pm 0.22	65.36 \pm 1.53	83.70 \pm 1.64	79.41 \pm 0.53	100

Overall, spray drying led to dry particles (LoD < 1.6%) with a high yield (> 82%). All samples showed a similar relatively high Carr index values (24%-29%). Highest Carr index values could be found for the samples 50:50 and JM. The Carr index of all powder samples indicated poor flow properties except for the sample 25:75, which exhibited passable flow properties [108] but this difference was

not statistically significant (except for sample 50:50, $p = 0.02$). These flow properties were in line with the expectations of microparticles showing an unfavorable mass/surface area ratio. The bulk density of the spray dried nanosuspensions was within a similar (low) range. The JM SD sample showed a particular low bulk density. The low densities combined with a high surface area may lead to uncontrolled agglomeration, which is a result of the high cohesion forces.

Figure 34 und Figure 35 show SEM pictures of all powder samples at different magnifications. All nano-in-microparticles showed a similar morphology: hollow spheres with partial corrugation. This morphology and the particle size range were independent of the MAN content of the spray dried particles, which is not in accordance with previous observations by Duret et al. (2012) [117]. They reported massive irreversible agglomeration after the spray drying process of ITZ nanosuspensions without MAN. Agglomeration was most likely caused by capillary pressure during the drying process [118,119]. Duret et al. (2012) used high pressure homogenization to create nanosuspensions which resulted in small platelet-like particles. Probably, this particle morphology favors aggregation by particle interaction and interlocking caused by an increased number of interaction sites compared to needle-shaped particles obtained after media milling.

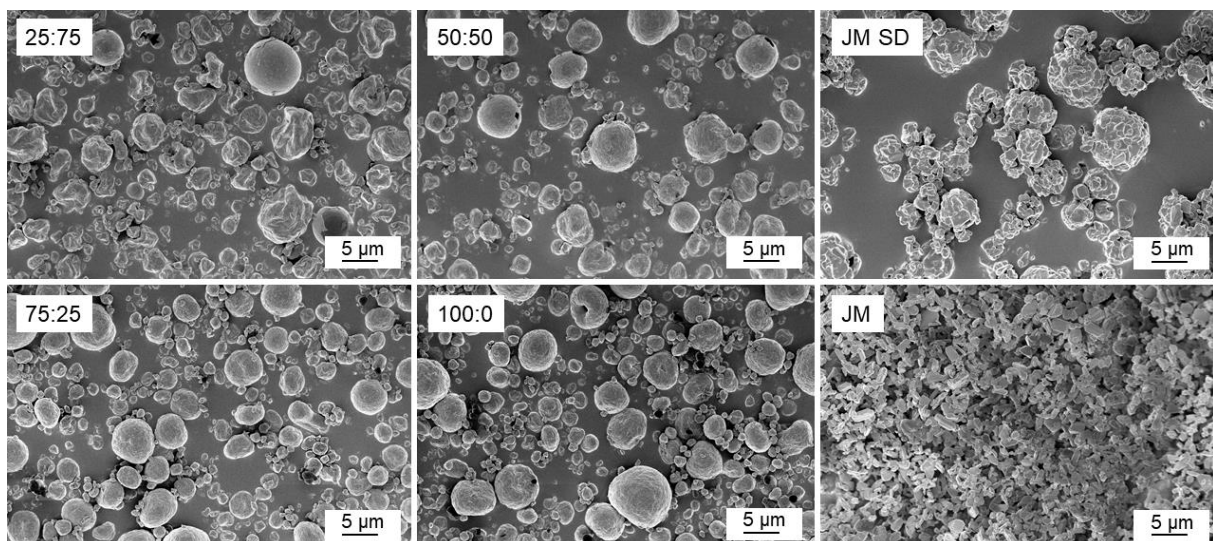


Figure 34: SEM images of nano-in-microparticles, the jet-milled sample (JM) and the jet-milled and spray dried sample (JM SD). Number in sample name describes the ratio of ITZ:MAN [%w/w].

Needle-shaped ITZ nanoparticles were visible on the surface of the spray dried particles. The JM particles showed a plate-like morphology with strong agglomeration tendency. These platelets were also evident on the surface of the JM SD particles.

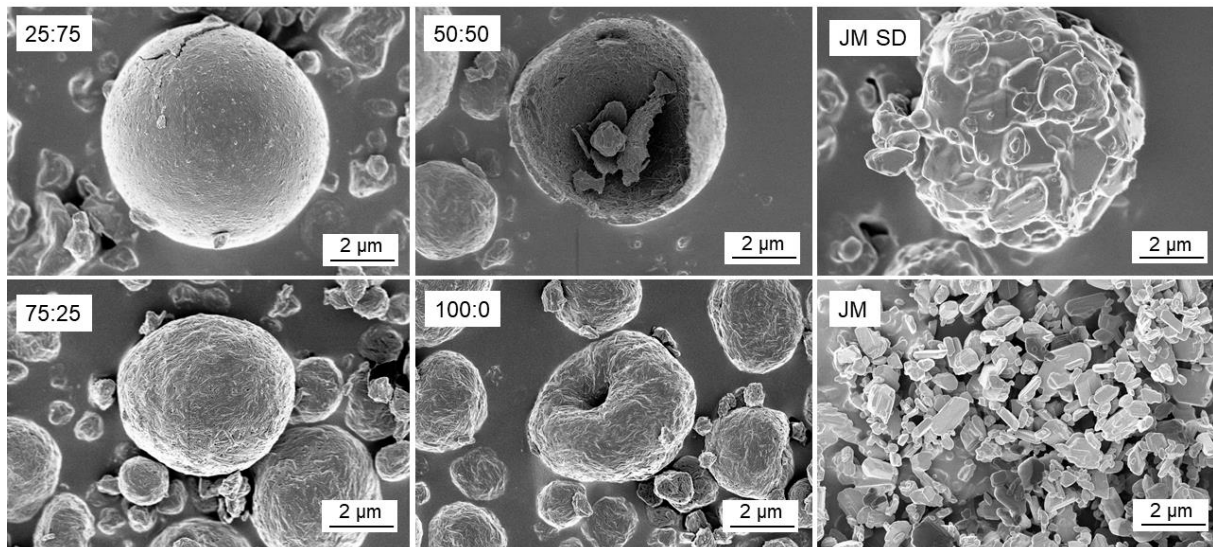


Figure 35: SEM images of the nano-in-microparticles, the jet-milled sample (JM) and the jet-milled and spray dried sample (JM SD). Number in sample name describes the ratio of ITZ:MAN [%w/w].

This particle morphology of the spray dried nanoparticles is the typical result of spray drying particles with a high Peclet number [27,58]. In case the droplet surface recession rate is much faster than the diffusion in the droplets, which is the case here as the suspended particles can be regarded as immobile according to Vehring (2008) [27], very high Peclet numbers can be applied. Hence, surface accumulation occurs, and a shell is formed [20,27,120]. This enrichment was supported by HPC-SL which is characterized with a high Peclet number and revealed a restricted diffusivity [58]. Furthermore, it hindered the nanoparticle mobility due to a viscosity increase. The surface enrichment was enhanced by the presence of surfactants in the suspension. Together, these facts supported the creation of spherical hollow particles. The donut-shaped particles, as shown for sample 100:0, were described for spray dried nanoparticles in literature as well [121,122]. It is supposed that this toroid morphology is caused by deformation of the droplet during the drying process due to loss of structural stability. This could be the result of a large droplet size, use of high process gas flow rates or the use of stabilizers [122]. Buckled particles, as shown for sample 50:0 in Figure 35, occur if the shell of the drying particle cannot stand the pressure difference which arise by continuous internal solvent evaporation during the drying process [58].

Overall, nanoization and spray drying led to hollow, low-density particles with poor powder flow characteristics, regardless of the drug load.

3.2.2.2 Solid-state analysis

Figure 36 shows the XRPD patterns of the powder samples. As references, patterns of ITZ starting material, MAN in different modifications, the physical mixture of the powder components and the ITZ nanosuspension before spray drying were included. All samples exhibited crystalline peaks and no halo indicating amorphous structures. In addition, differential scanning calorimetry showed no glass transitions (data not shown), which supported the finding that the samples were crystalline after spray drying. The nanosuspensions showed similar peaks in XRPD diffractograms as ITZ starting material but with a slightly lower peak intensity. β -MAN, which was used as starting material, could not be found in the spray dried samples. δ -MAN has a characteristic peak at $9.7^\circ 2\theta$ [123], which could be found in the δ -form reference and in various manifestation in all other spray dried samples containing mannitol (25:75, 50:50 and 75:25). The samples 50:50 and 75:25 showed no other characteristic peaks except for δ -MAN and ITZ. Sample 25:75 showed a weak peak at $9.7^\circ 2\theta$ and additional ones at 9.4° , 13.7° and $14.6^\circ 2\theta$. The three latter peaks could also be found in the α -MAN reference, which is in agreement with literature [123,124]. The samples JM and JM SD showed similar reflexes to the ITZ starting material reference.

Differences in MAN samples obtained after spray drying and the MAN starting material seemed to be depending on the composition of the formulations. The stabilizers probably have a strong impact, as no difference in modification was observed when spray drying a solution with β -mannitol as starting material in demineralized water, whereas incorporating stabilizers triggered the formation of the α -form, as shown in chapter 3.2.1.3. The reason for the different modifications was presumably related to the varying HPC-SL concentration. Sample 25:75 exhibited an amount of 6% (w/w) HPC-SL relative to mannitol which seemed to stabilize the α -polymorph, whereas 75:25 exhibited 62% (w/w) HPC-SL relative to mannitol and lead to the δ -form. However, this observation was different to the results of the process development with mannitol, where the α -form was found for an HPC-SL amount of 17% relative to mannitol (same amount as for sample 50:50). The suspended ITZ nanoparticles presumably impacted the crystallization process of the mannitol enabling the formation of a different polymorph. Buanz et al. (2019) reported the influence of "foreign" particles on the formation of metastable mannitol modifications during drying of mannitol droplets [125]. These additional particles on the surface of the droplet might inhibit or retard the nucleation of certain polymorphs, e.g., stabilize the α -form. However, no clear mechanism can be suggested.

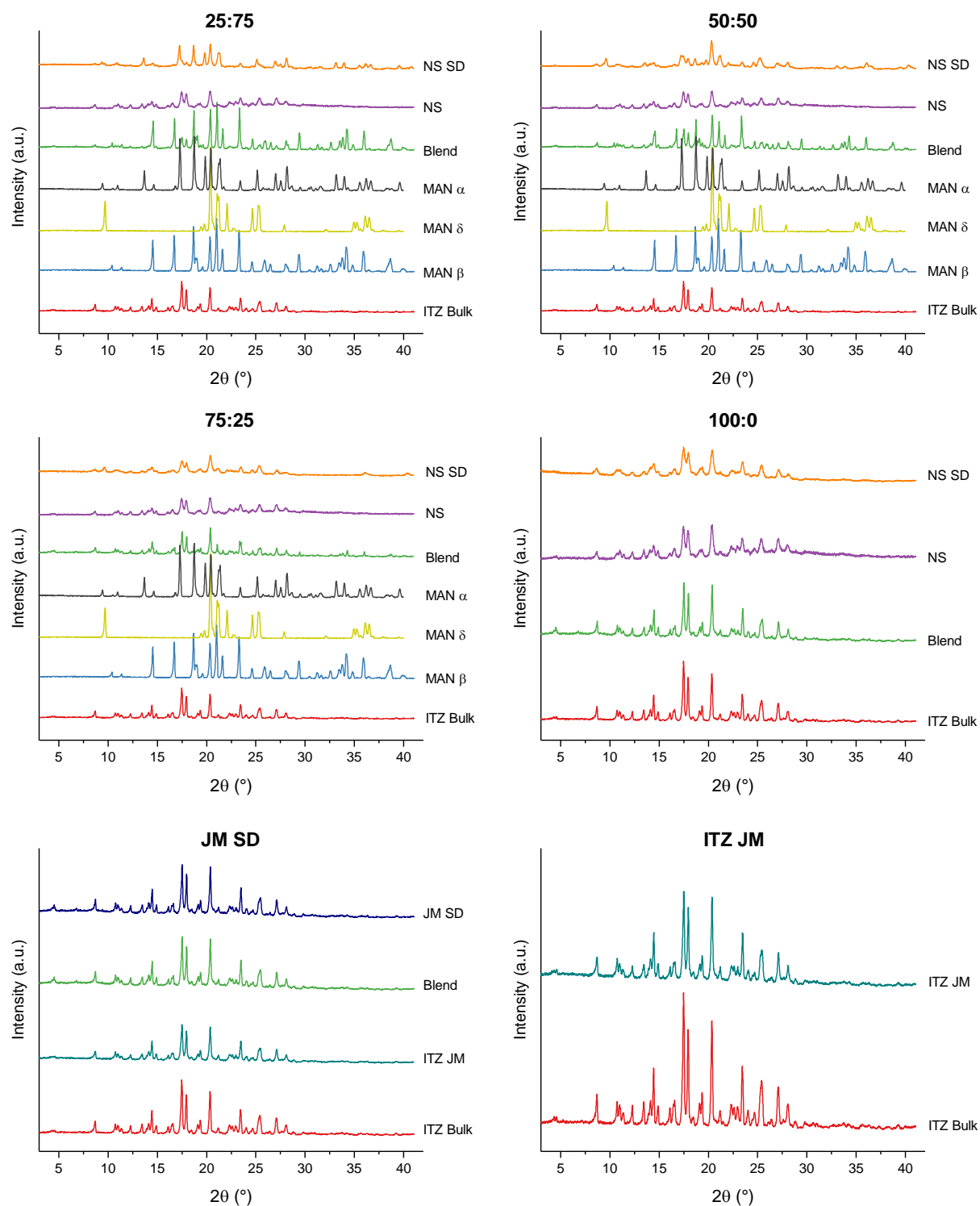


Figure 36: XRPD patterns of the powder samples. Sample name is indicated at the top of each figure. Number in sample name describes the ratio of ITZ:MAN [%w/w]. Plots are shifted for better illustration. JM: jet-milled, JM SD: je-milled and spray dried.

The presence of metastable MAN modifications might impact the performance of the formulations during storage, so that the polymorphic form of MAN should be monitored during storage stability studies.

In conclusion, both ITZ and MAN were found in crystalline state after spray drying. The MAN modification changed compared to the starting material as stabilizers and the suspended ITZ particles might favor the formation of the metastable α - and δ -polymorphic forms of MAN. However, no clear mechanism is evident, and the modification of MAN needs to be monitored during storage.

3.2.2.3 Impact of relative humidity on solid-state stability

A hint on the behavior during storage of solid particles can be given by vapor sorption measurements.

Figure 37 and Figure 38 show the relative mass change during moisture adsorption and desorption of the ITZ powder samples and starting materials in relation to the relative humidity.

The evaluation of the moisture sorption behavior showed differences within the samples although all samples released the adsorbed water completely and no hysteresis occurred.

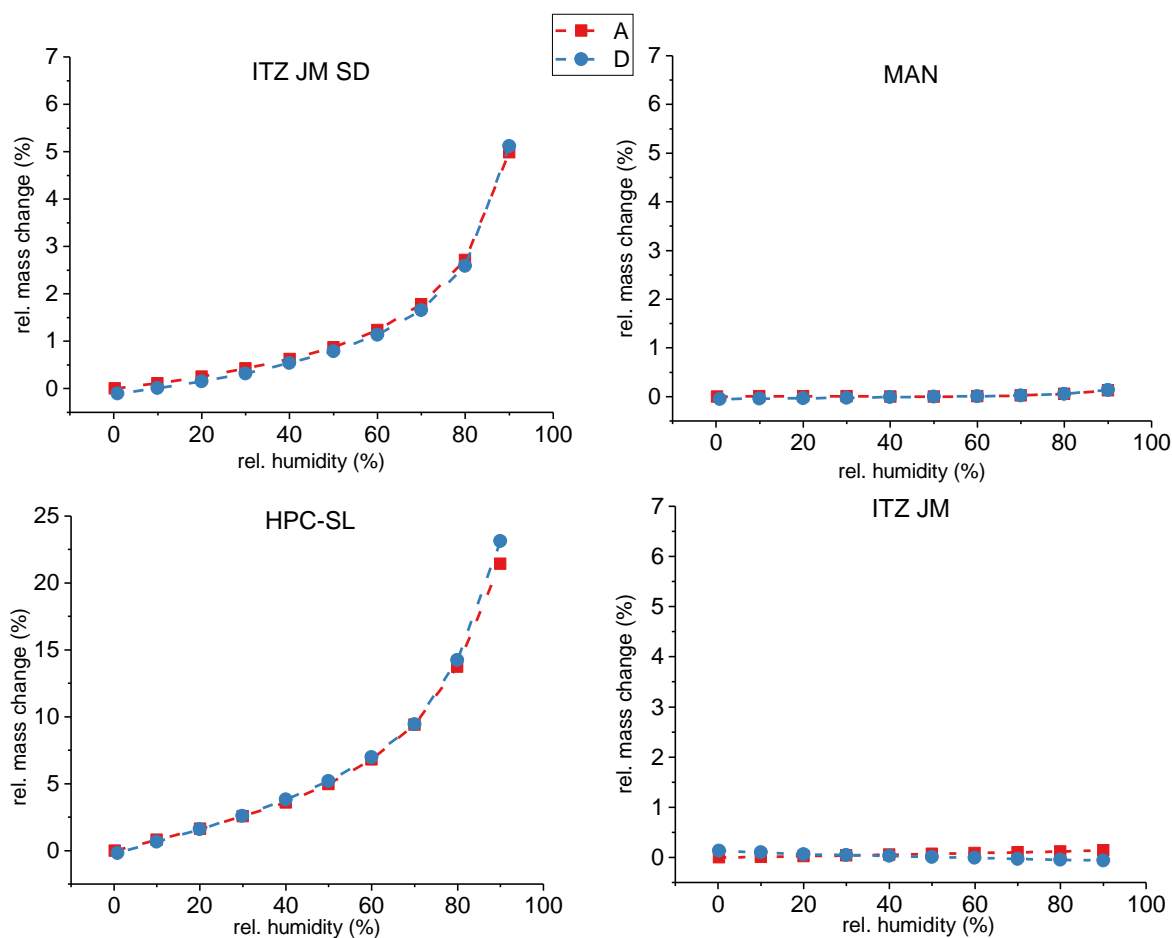


Figure 37: Adsorption (A) and desorption (D) curves for the powder samples and starting materials measured by DVS. Sample name is indicated on the top of each plot. JM: jet-milled, JM SD: jet-milled and spray dried.

As illustrated in Figure 37, HPC-SL showed a high moisture sorption and hence distinct hygroscopicity, as also described in literature [86]. In contrast to that, the MAN and ITZ JM showed very low mass changes (below 1% (w/w)). This is in accordance with literature for MAN as this compound is known to be not hygroscopic [86]. The low moisture sorption for ITZ can be explained by its hydrophobic nature. The difference in moisture sorption between samples JM and JM SD was related to the HPC-SL amount: sample JM SD (calculated amount of 14.59% (w/w) HPC-SL) showed maximum 4.99% (w/w) mass change, whereas sample JM (0.00% (w/w) HPC-SL) exhibited a maximum uptake of 0.14% (w/w) water.

The nano-in-microparticles showed a moisture sorption behavior depending on the sample composition (see Figure 38). The higher moisture sorption of formulations with less mannitol was related to the higher HPC-SL amount of these formulations. Sample 25:75 exhibited the lowest HPC-SL amount and showed the lowest vapor sorption.

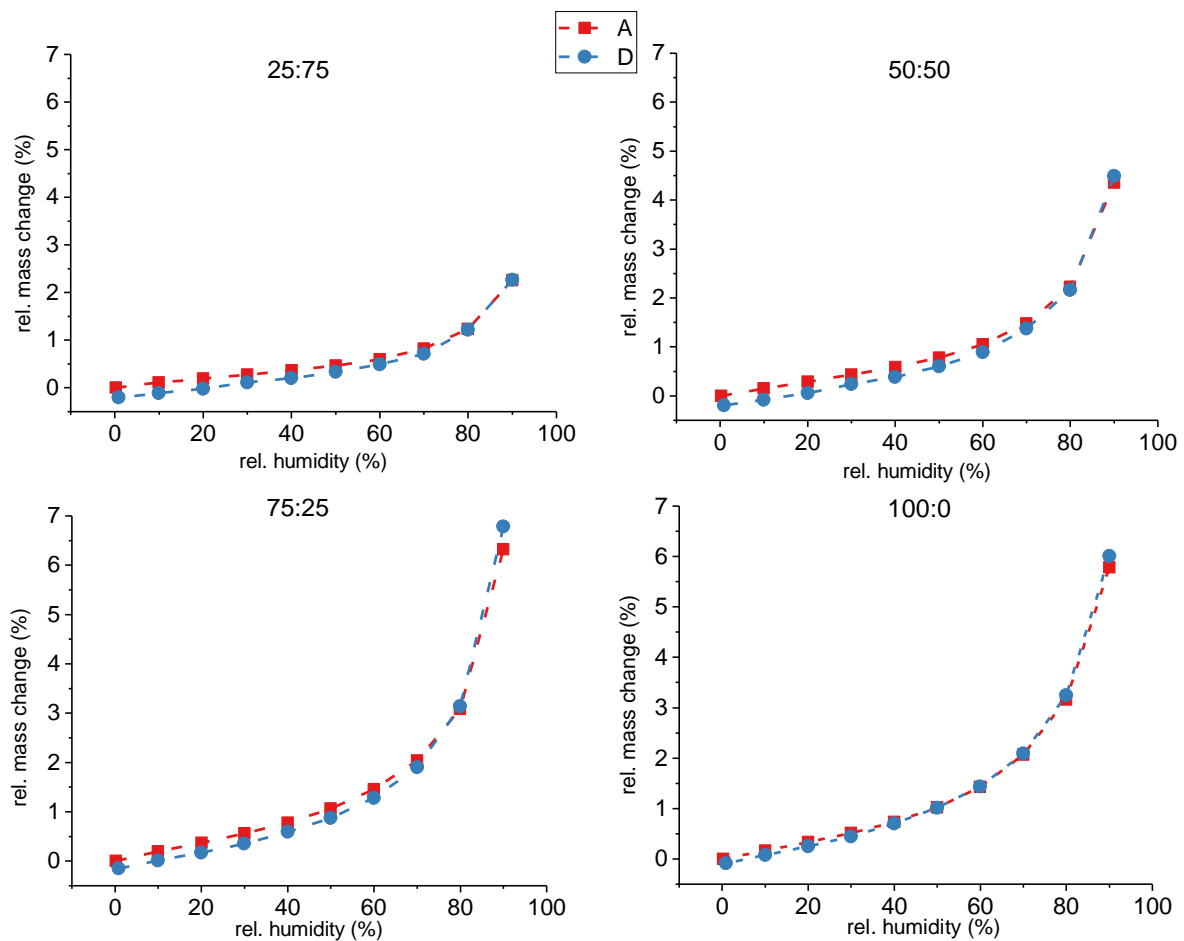


Figure 38: Adsorption (A) and desorption (D) curves for the nano-in-microparticles measured by DVS. Sample name is indicated on the top of each plot (number: ratio of ITZ:MAN [%w/w]).

Solid-state analysis after DVS, illustrated in Figure 39, indicated no modification change as no additional peaks occurred. Although δ -mannitol is known as a metastable form, no physical instability was observed even at very high relative humidity values. Therefore, the formulations were expected to show good storage stability with regard to solid-state.

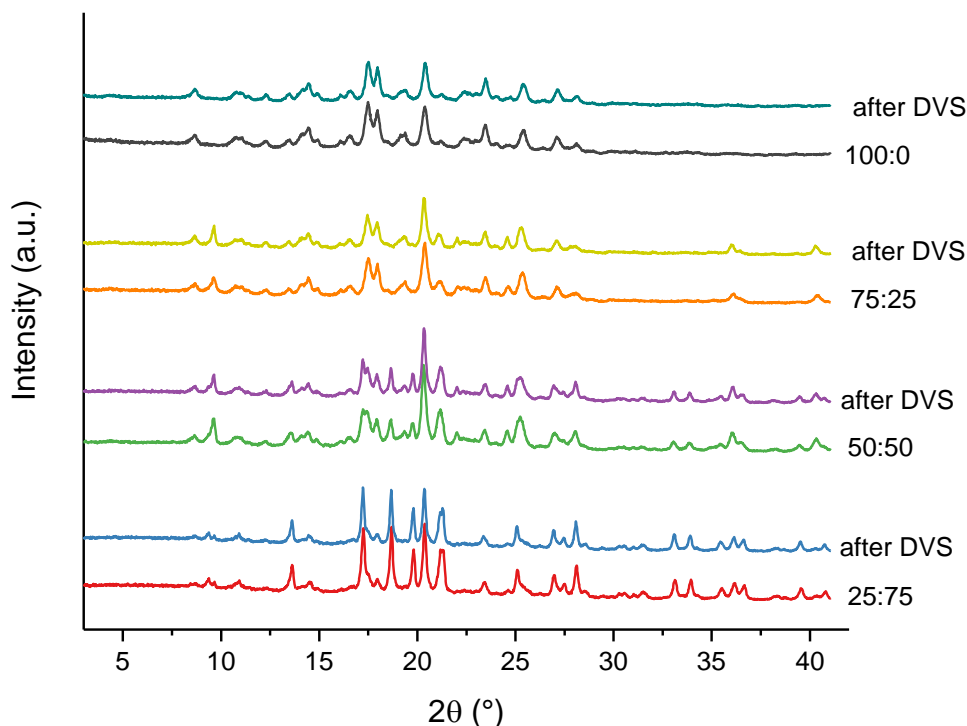


Figure 39: XRPD patterns of the powder samples before and after one DVS cycle. Plots are shifted for better illustration. Number in sample name describes the ratio of ITZ:MAN [%w/w].

In order to minimize the potential effect of the humidity, all powder samples were stored in a desiccator over molecular sieve. Conditioning (storage under defined humidity) was not regarded as necessary in this case as no amorphous material was generated (compared to carrier-based formulations in which the API usually is jet-milled and might need to be stored at specific rH conditions to enable controlled crystallization of amorphous regions [126]). Nevertheless, investigation of storage stability is required since not only solid-state is a critical parameter. Relative humidity might have an impact on e.g., chemical stability and aerosolization performance as well [31,32].

Overall, the samples showed a slight hygroscopicity. The water uptake was directly correlated to the HPC-SL content in the samples as pure MAN and ITZ were not hygroscopic. The exposure to humidity did not affect the solid-state stability as no modification change occurred.

3.2.2.4 Dispersibility of ITZ dry powder particles by pressure titration

Figure 40 illustrates the mean particle size (d_{50}) of the powder samples in relation to the dispersion pressure obtained by laser diffraction. At the lowest possible dispersion pressure of 0.1 bar the particle size of four out of six samples were in a geometric diameter range of below 5 μm with

exception of samples JM and JM SD. The sample JM SD revealed a significantly higher particle size ($6.7 \mu\text{m} \pm 0.3 \mu\text{m}$) than all other samples ($p < 0.01$), which decreases with rising dispersion pressure. This shows a very poor de-agglomeration behavior even at the lowest dispersion pressure, that could be related to the rough surface with large asperities potentially leading to mechanical interlocking. Particle size of sample JM was found to be $5.0 \mu\text{m}$ at 0.1 bar and decreased to a constant value of about $2 \mu\text{m}$ with rising dispersion pressure, indicating a high agglomeration tendency even at a low dispersion pressure. The presence of these agglomerates led to the conclusion that this sample could also show poor deagglomeration in a DPI, demonstrating the need for a coarse carrier for inhalation.

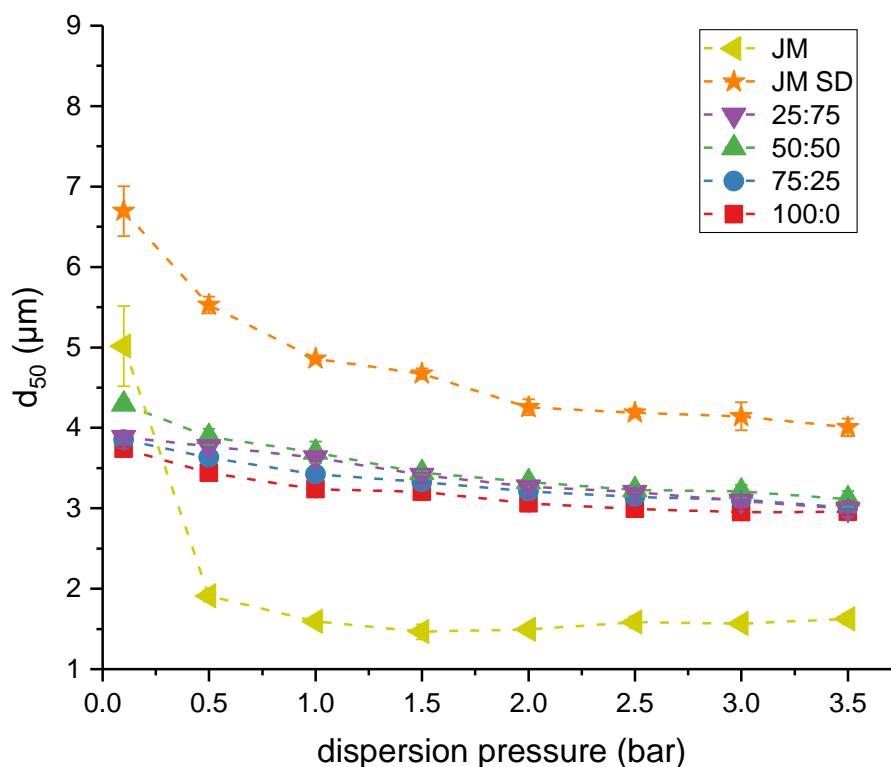


Figure 40: Mean particle size (d_{50}) of ITZ powder samples in relation to the dispersion pressure (pressure titration). Number in sample name describes the ratio of ITZ:MAN [%w/w]. JM: jet-milled, JM SD: jet-milled and spray dried. Values are expressed as mean \pm SD ($n = 3$).

The nano-in-microparticles showed the lowest change in particle size over the whole dispersion pressure range demonstrating a very low agglomeration tendency, which could presumably be related to the low density, or the smoother surface compared to sample JM SD.

Nevertheless, the dispersion pressure in the laser diffraction experiments is much higher (0.1 bar compared to 0.04 bar in a DPI at 4 kPa pressure drop) and mechanisms in an inhalation device differ,

especially for the HandiHaler® as the capsule motion is known to support de-agglomeration [65]. It is assumed that samples, which cannot be de-agglomerated at the lowest dispersion pressure (JM and JM SD), will as well show a poor de-agglomeration behavior in the cascade impaction experiments. The direct comparison of JM SD and 100:0 shows very clearly the possibilities of particle engineering for ITZ.

Consequently, the nano-in-microparticles are expected to show a higher fine particle fraction compared to jet-milled samples (JM and JM SD) as they show no drop in particle size over the dispersion pressure range indicating a low agglomeration tendency. The drug load presumably did not influence the dispersibility.

3.2.2.5 Reconstitution of spray dried nanoparticles in water

The impact of spray drying on the reconstitution of ITZ nanoparticles in water as well as the effect of the MAN concentration was analyzed. The nano-in-microparticles were diluted with water to a concentration of 5% (w/w), which was the same for spray drying, and were gently stirred with a magnetic stirrer. The particle size of the particles was evaluated for a time period of 24 hours by DLS, as shown in Figure 41, where the particle size (A) and PDI (B) of nano-in-microparticles are displayed.

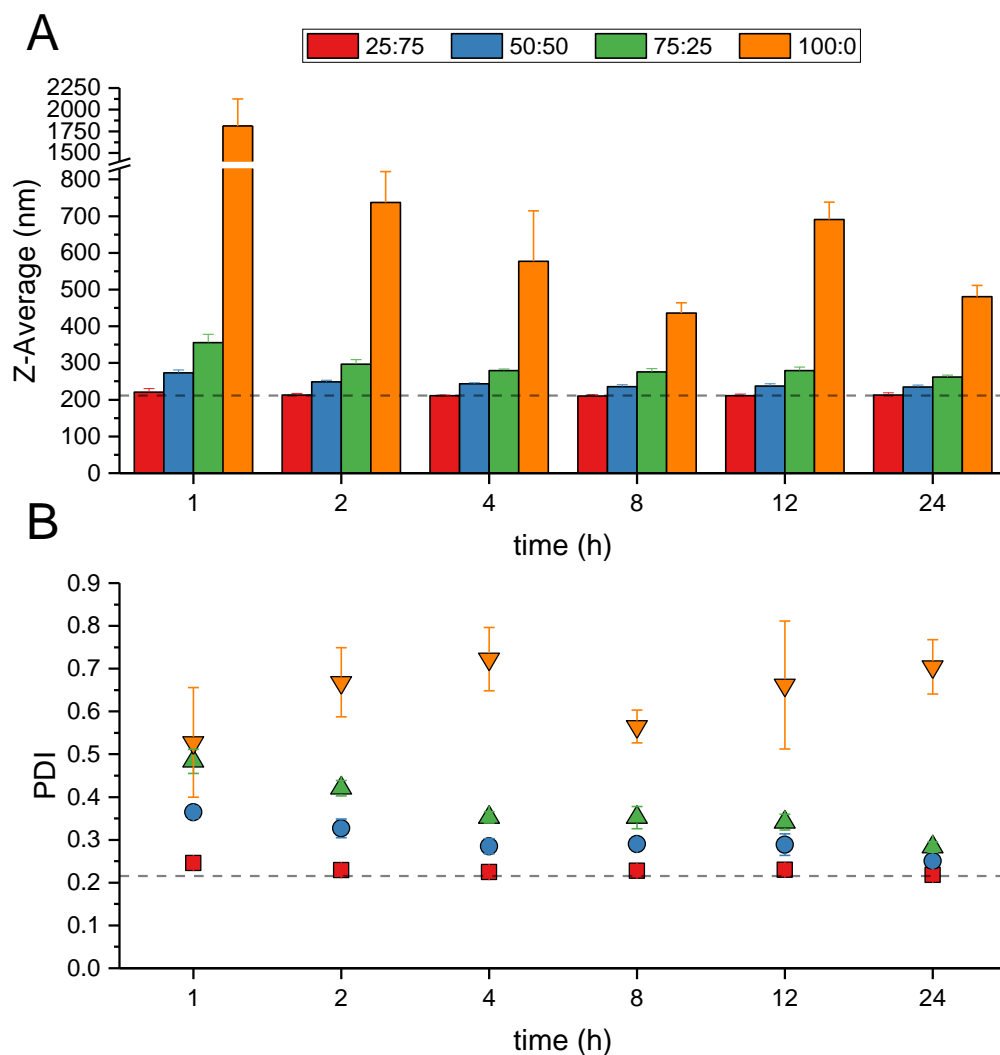


Figure 41: Particle size (A) and PDI (B) of the reconstituted nano-in-microparticles in relation to the stirring time. Dashed line indicates value before spray drying (nanosuspension). Values are expressed as mean \pm SD, $n = 3$. Sample names indicate the ITZ:MAN ratio (% w/w).

Compared to the initial nanoparticle size before spray drying (210 nm), only sample 25:75 showed no significant difference, regardless of the reconstitution time (e.g., $p = 0.24$ for one hour). The PDI of this sample was significantly higher compared to the initial value (0.21), except for a reconstitution time of 12 h ($p = 0.18$) and 24 h ($p = 0.73$), but still in the same range. Sample 100:0 exhibited the largest particle sizes and highest PDI values after reconstitution. However, the particle size decreased from 1750 nm after one hour reconstitution to 500 nm after 24 h reconstitution time with a corresponding PDI of 0.7. After 24 h of reconstitution time, the PDI values of the samples 25:75, 50:50 and 75:25 were similar (0.2-0.3) but still significantly different ($0.001 < p < 0.03$).

The reconstitution of spray dried nanoparticles could be affected by manufacturing process parameters (e. g. the outlet temperature as described in [127]) and formulation parameters (such as the

HPC type and concentration [128]). As the product temperature was kept constant at a suitable value, it did not affect the reconstitution of the samples in this case. The polymer concentration was also kept constant for all nanosized samples and solely the MAN concentration was changed. This illustrates the impact of MAN concentration on the reconstitution: the higher the MAN content, the faster and to a greater extent the reconstitution occurred. This was in accordance with the results reported in literature for other APIs [105,129–131]. The ease of reconstitution with higher MAN amounts could be explained by MAN particles forming a matrix around the ITZ nanoparticles and preventing them from irreversible agglomeration. In general, spray drying had no negative impact on the nanoparticles since the samples maintained their size and even sample 100:0 showed reconstitution to a certain extent. Pulmonary aspergillosis can affect the bronchial tract as well as the alveoli [1]. Therefore, it is not trivial to define a pulmonary target region resulting in a target particle size for the ITZ particles. However, ABPA mainly affects the lower respiratory tract [132], hence this is regarded as target region here. Prerequisite for a therapeutic effect is the reconstitution of the nano-in-microparticles into ITZ nanoparticles followed by dissolution of these particles. Although samples 25:50 and 50:50 showed the fastest reconstitution, presumably also faster dissolution, they have a lower dose at the same time and were therefore regarded as not beneficial in this context. Taking into account the high fine particle dose, which is required [5], samples 75:25 or 100:0 seemed to be feasible options containing 65% (w/w) and 84% (w/w) ITZ, respectively. Sample 75:25 is preferred over 100:0 as it enabled a faster reconstitution in a volume comparable to the lining fluid [133].

In conclusion, the MAN content in the composite particles highly affected the reconstitution of the nano-in-microparticles into the original nanoparticles present prior to spray drying. The higher the MAN content, the faster the reconstitution. Sample 100:0 also showed reconstitution to a certain extent (gaining nanoparticle size again after four hours of reconstitution). Hence, spray drying had no negative impact on the reconstitution of the nanoparticles.

3.2.3 Conclusion of the spray drying process

It was found that both the outlet temperature and the presence of stabilizers highly affect the morphology and the polymorphic form of spray dried plain MAN particles. A rougher surface was observed for H₂O 80°C compared to H₂O 60 °C. At an outlet temperature of 100 °C, the particles were significantly larger and lost their spherical shape, which could presumably be attributed to the for-

mation of sintered, large MAN agglomerates. This effect was independent of the presence of stabilizers. However, the stabilizers impacted the size of the MAN crystals as only small crystals were found for samples Med 60 °C and Med 80 °C leading to quite smooth particles for both samples. In case of the H₂O-samples, the β -form of MAN was present. Additionally, the α -form of MAN was found for the highest outlet temperature caused by an altered crystallization kinetics. For the Med-samples, the α -modification was obtained, regardless of the outlet temperature, probably related to the presence of HPC in the formulation. The process evaluation showed as optimized spray drying parameters an outlet temperature of 60 °C, a nozzle gas flow rate of 23 SL/min and a feed rate of 5 g/min.

Overall, nanoization and spray drying led to hollow, low-density composite particles with poor powder flow characteristics, regardless of the drug load. Both ITZ and MAN were found in crystalline state after spray drying. The MAN modification differed compared to the starting material as stabilizers and the suspended ITZ particles might favor the formation of the metastable α - and δ -polymorphic forms of mannitol. Furthermore, the samples showed a slight hygroscopicity. The water uptake was directly correlated to the HPC-SL content in the samples as MAN and ITZ were not hygroscopic. Exposure to humidity did not affect the solid-state stability as no modification change occurred. The evaluation of dispersibility demonstrated that nanoization and consecutive spray drying as a particle engineering technique enables the generation of small spheres with a low density and an excellent dispersibility. Furthermore, the drug load did not affect the dispersibility, which means that even formulations with up to 84% ITZ may be delivered to the lung efficiently. Samples JM and JM SD showed a significantly worse dispersibility highlighting the benefits of nanoization.

The MAN content in the composite particles highly affected the reconstitution of the nanoparticles in water. The higher the MAN content was, the faster was the reconstitution. The sample containing no MAN also showed reconstitution to a certain extent (gaining nanoparticle size again after four hours of redispersion). Hence, spray drying had no negative impact on the nanoparticle size.

3.3 In-vitro aerodynamic assessment

The effect of nanoization and spray drying on the in-vitro inhalative performance of the ITZ dry powder formulations was investigated by NGI cascade impaction analysis. The impact of the drug load of the spray dried particles and the inhalation device on the aerodynamic performance was evaluated.

3.3.1 Filling of nano-in-microparticles into primary packaging materials

Reproducible and accurate powder filling is challenging and especially in the case of high dose formulations without coarse fillers, that typically do not exhibit suitable flow properties.[134]. The poor flow properties, reported in the previous chapter, are typical for microparticulate formulations, which consequently have a high surface area thus showing strong aggregation. This might negatively impact the filling process [135].

A reproducible filling process with a target filling amount of 13.5 mg powder formulation (defined through the volume of the blister cavity) was achieved using an in-house made automated filling machine (BI drum filler) that allowed accurate filling with all samples meeting the acceptance value (AV) according to the test "Uniformity of Dosage Units" (Ph. Eur., chapter 2.9.40) [80] (see Table 14). Although all formulations met the acceptance criteria, the AV were borderline for some formulations. Showing the highest d_{50} , sample 50:50 exhibited the lowest AV among the nano-in-microparticles, which could be related to a superior flowability. Carr index values and bulk densities of all samples were comparable and therefore no correlation to the filling performance could be found, as described otherwise in literature for much larger particles [136].

Table 14: Physicochemical properties of nano-in-microparticles, sample JM SD and sample JM. Number in the sample name indicates the ratio of ITZ:MAN [% w/w]. Samples JM and JM SD (marked with *) were filled manually. Values are expressed as mean \pm SD.

Sample	25:75	50:50	75:25	100:0	JM SD*	JM*
article density [g/cm³] (n = 10)	1.46 \pm 0.00	1.44 \pm 0.00	1.37 \pm 0.00	1.33 \pm 0.00	1.40 \pm 0.00	1.37 \pm 0.01
Bulk density [g/cm³] (n = 3)	0.24 \pm 0.01	0.22 \pm 0.03	0.22 \pm 0.00	0.18 \pm 0.00	0.12 \pm 0.00	0.16 \pm 0.01
Tapped density [g/cm³] (n = 3)	0.32 \pm 0.01	0.29 \pm 0.00	0.30 \pm 0.01	0.25 \pm 0.00	0.16 \pm 0.00	0.22 \pm 0.01
Carr Index (n = 3)	24.02 \pm 2.05	29.16 \pm 0.99	27.34 \pm 0.58	26.51 \pm 1.32	26.80 \pm 3.03	28.36 \pm 2.38
Mean powder dose per cavity/capsule \pm SD [mg] (n = 10)	13.79 \pm 0.82	13.41 \pm 0.44	13.67 \pm 0.62	12.39 \pm 0.20	13.37 \pm 0.43	13.47 \pm 0.32
RSD of mean powder dose [%] (n = 10)	5.92	3.28	5.48	1.63	3.21	2.39
Calculated mean ITZ dose per cavity/capsule [mg]	3.27	5.88	8.93	10.37	10.62	13.47
Dosage uniformity (AV)*	15	8	13	10	8	6

* AV \leq 15 is accepted according to the Ph. Eur.

Samples JM and JM SD could not be filled automatically and were filled manually instead. Very poor flowability and the occurrence of rat holes in the powder reservoir made automatic filling impossible. This was most likely related to either the strong cohesiveness of sample JM, which was also observed in the pressure titration experiments, or to mechanical interlocking as sample JM SD had a very rough and irregular surface (observed in the SEM images, Figure 35).

Increasing the negative pressure for drum filling could probably optimize the filling process to reduce the AV of the nano-in-microparticles, but this would most likely increase the density of the powder pellet formed in the drum, leading potentially to a worse dispersibility [134,137].

Volume-based filling using a similar principle of operation is commercially available (e.g., Omnidose by Harro Höfliger) and hence, it is to be expected that the process can be scaled up easily, as reported in literature from the Omnidose TT to Omnidose DF1 [73].

Overall, automatic filling with the BI drum filler was carried out successfully for the nano-in-microparticles but the process appeared challenging for samples JM and JM SD, which is due to pronounced cohesiveness of the powders.

3.3.2 Overview of cascade experiments and impact of inhalation device

The FPFs obtained with the HandiHaler® using the nano-in-microparticles were significantly higher than for the samples JM SD and JM, as shown in Figure 42. The drug load of the nano-in-microparticles did not affect the FPF as there was no significant difference ($0.10 < p < 0.88$). The FPF of JM SD and JM were statistically equivalent ($p = 0.63$) to each other but significantly lower compared to the nano-in-microparticles ($p < 0.01$).

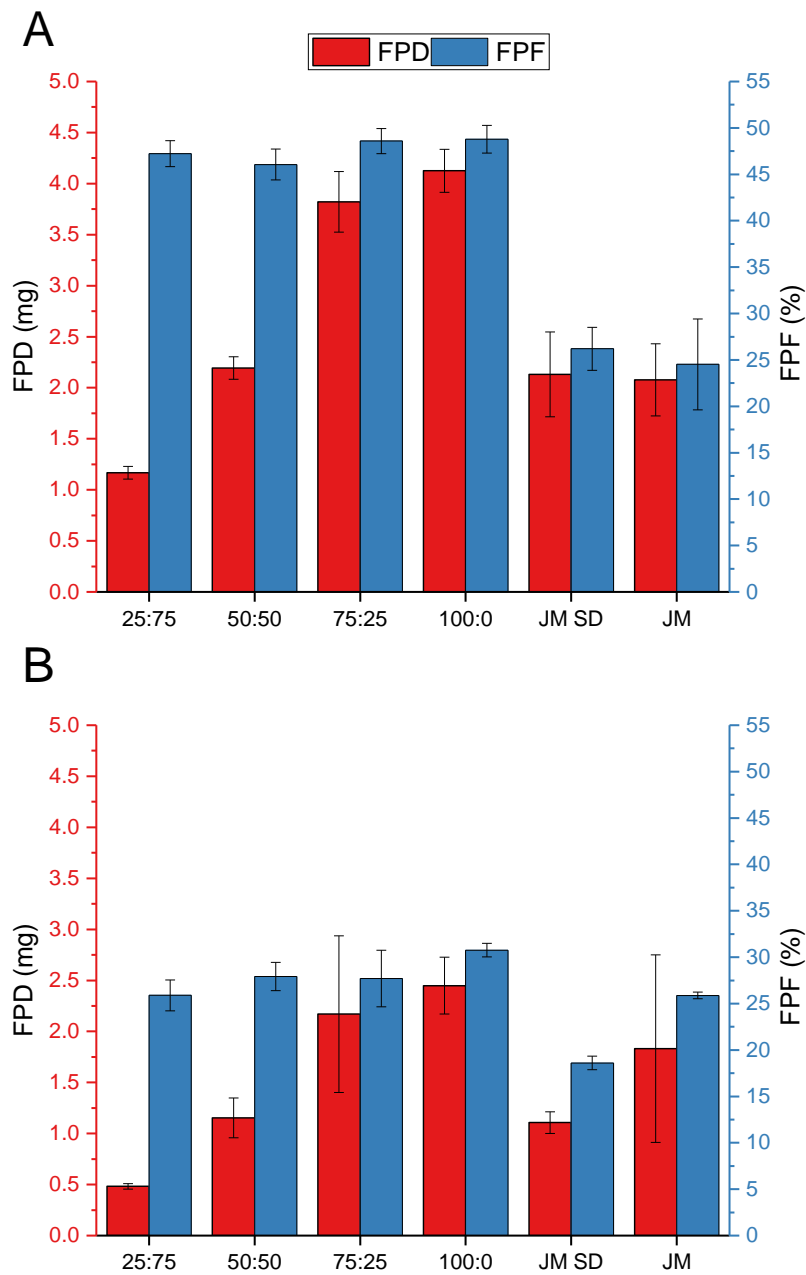


Figure 42: Comparison of FPD (red) and FPF (blue) for the HandiHaler® (A) and the GyroHaler® (B). Values are given as mean \pm SD. Number in sample name describes the ratio of ITZ:MAN [%w/w]. JM: jet-milled, JM SD: jet-milled and spray dried.

The MMAD and GSD values are shown in Table 15. Sample JM SD showed the highest MMAD value with significant difference to the other samples ($p < 0.01$).

Table 15: Results of the aerodynamic assessment of the formulations in relation to the device. Values are expressed as mean \pm SD, n = 3. Formulation JM and JM SD (marked with *) were filled manually. Number in sample name describes the ratio of ITZ:MAN [%w/w]. JM: jet-milled, JM SD: jet-milled and spray dried.

Device	HandiHaler®						GyroHaler®					
	25:75	50:50	75:25	100:00	JM SD*	JM*	25:75	50:50	75:25	100:0	JM SD*	JM*
MMAD [μ m]	2.96 \pm 0.09	3.14 \pm 0.07	3.02 \pm 0.03	2.85 \pm 0.09	4.36 \pm 0.22	3.11 \pm 0.21	3.79 \pm 0.26	3.69 \pm 0.19	3.74 \pm 0.11	3.35 \pm 0.07	4.86 \pm 0.14	2.88 \pm 0.12
GSD	1.98 \pm 0.03	1.91 \pm 0.01	1.98 \pm 0.01	2.09 \pm 0.06	1.81 \pm 0.03	2.05 \pm 0.02	1.95 \pm 0.02	1.97 \pm 0.05	2.04 \pm 0.05	2.12 \pm 0.02	1.83 \pm 0.06	2.20 \pm 0.13

For the GyroHaler® a slightly different result of the six formulations could be observed. A low FPF of 18.6% was found for the sample JM SD with a statistically significant difference compared to all other samples ($p < 0.03$). In contrast to that, sample 100:0 showed the highest FPF. The FPFs of the nano-in-microparticles were comparable to the FPF of sample JM. The MMADs of the nano-in-microparticles were similar and differed significantly to samples JM and JM SD ($p < 0.03$). The latter sample showed the largest MMAD.

The observations made in the pressure titration experiments could be confirmed by cascade impaction. Formulations JM and JM SD showed a lower FPD compared to the nano-in-microparticles, independent of the device. In the pressure titration experiments, the dispersibility of the nano-in-microparticles was distinctly better compared to samples JM and JM SD.

As described in chapters 1.2.3.1 and 2.2.2.13, the HandiHaler® and the GyroHaler® are characterized with different intrinsic resistance. The cut-off diameters of the NGI stages are dependent on the flow rates and therefore differ for different devices at 4 kPa pressure drop.

The particles dispersed by the GyroHaler® were deposited in the SIP and preseparator to a large extent, as also shown in Figure 43.

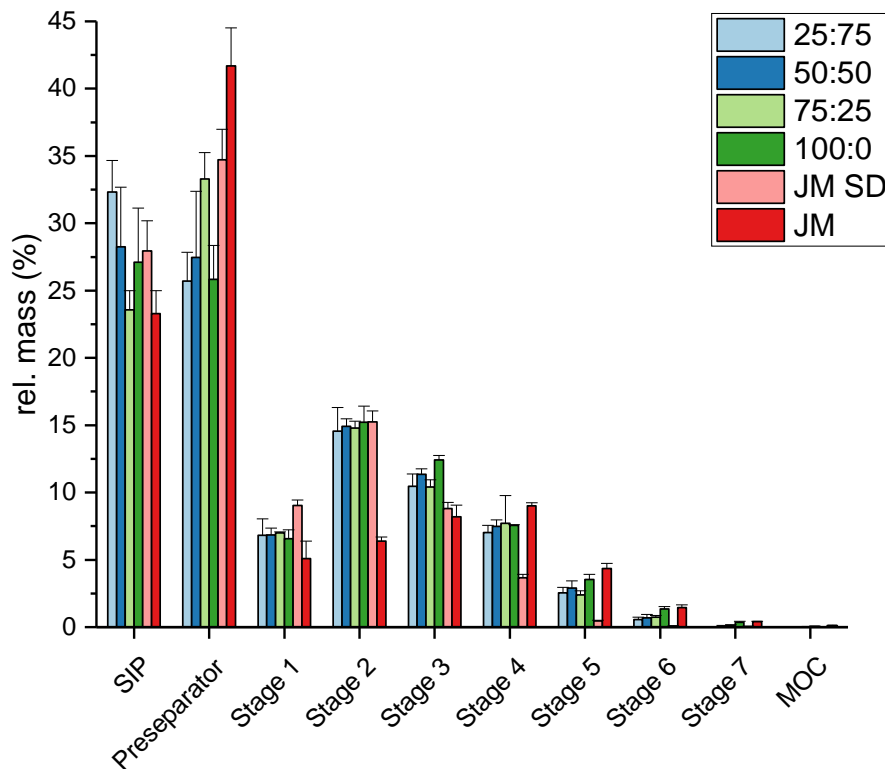


Figure 43: Results of the impaction measurements with the GyroHaler®. Values are expressed as mean \pm SD, n = 3. Mass is related to the recovered (=emitted from the device) mass of the NGI including SIP and preseparator. Number in sample name describes the ratio of ITZ:MAN [%w/w]. JM: jet-milled, JM SD: jet-milled and spray dried.

In contrast, the HandiHaler® showed a comparable deposition in the SIP but the amount of the formulations, which was deposited in the preseparator, was distinctly lower (except for JM SD and JM), see Figure 44.

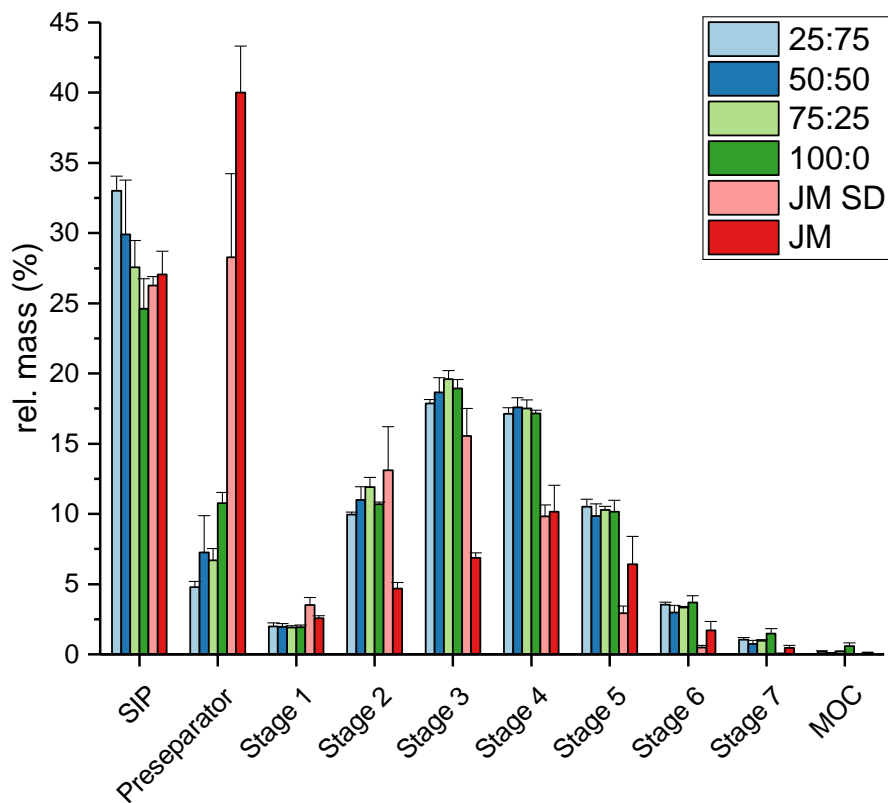


Figure 44: Results of the impaction measurements with the HandiHaler®. Values are expressed as mean \pm SD, $n = 3$. Mass is related to the recovered (=emitted from the device) mass of the NGI including SIP and preseparator. Number in sample name describes the ratio of ITZ:MAN [%w/w]. JM: jet-milled, JM SD: jet-milled and spray dried.

As shown in Table 15 and Figure 42, the FPFs and the MMAD differed significantly for all formulations, except for JM, when both inhalation devices are compared. The HandiHaler® generated noticeably higher FPFs and lower MMADs. However, the GSD was comparable and not significantly different.

Interestingly, for both devices the ED was similar for most of the formulations except for samples 25:75 and JM SD, where a significant difference was observed between the two devices (see Figure 45, $p < 0.05$).

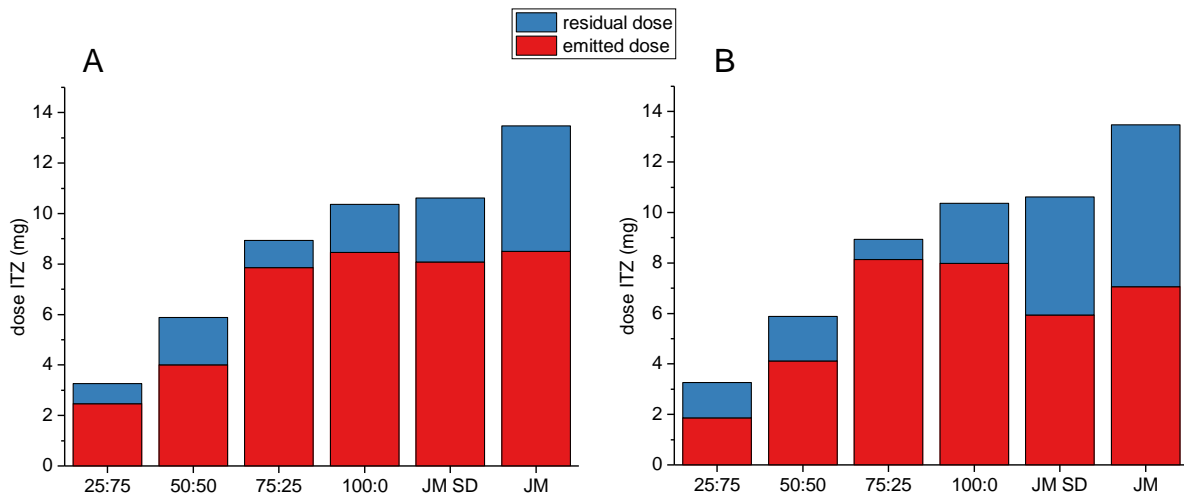


Figure 45: Overview of calculated residual ITZ dose in the device and emitted (= recovered from NGI) ITZ mass for the HandiHaler® (A) and the GyroHaler® (B). Number in sample name describes the ratio of ITZ:MAN [%w/w]. JM: jet-milled, JM SD: jet-milled and spray dried. The total dose of ITZ varies dependent on the drug loading of the filled 13.5 mg powder formulation.

The FPF is an important criterion for the performance of a DPI formulation in combination with the device. As the focus is on high dose, the FPD is the more meaningful parameter to consider. The FPD showed significant differences with lower values for the GyroHaler® for all other samples, except for 75:25 and JM (see Figure 42). This could also be seen in Figure 43, where the deposited mass fractions in relation the cut-off diameter were plotted in one graph for both devices. A shift in the distributions towards smaller cut-off diameters (and therefore towards a higher FPD) could be observed for nearly every formulation with the HandiHaler®. A reason for this was most likely the differing dispersion mechanisms of the two devices. The motion of the capsule (axially vibration) in the HandiHaler® probably increases the dispersion of the powder formulation [38,65,66,138]. In contrast to that, the GyroHaler® presumably does not foster the aerosolization and requires therefore a well dispersible powder.

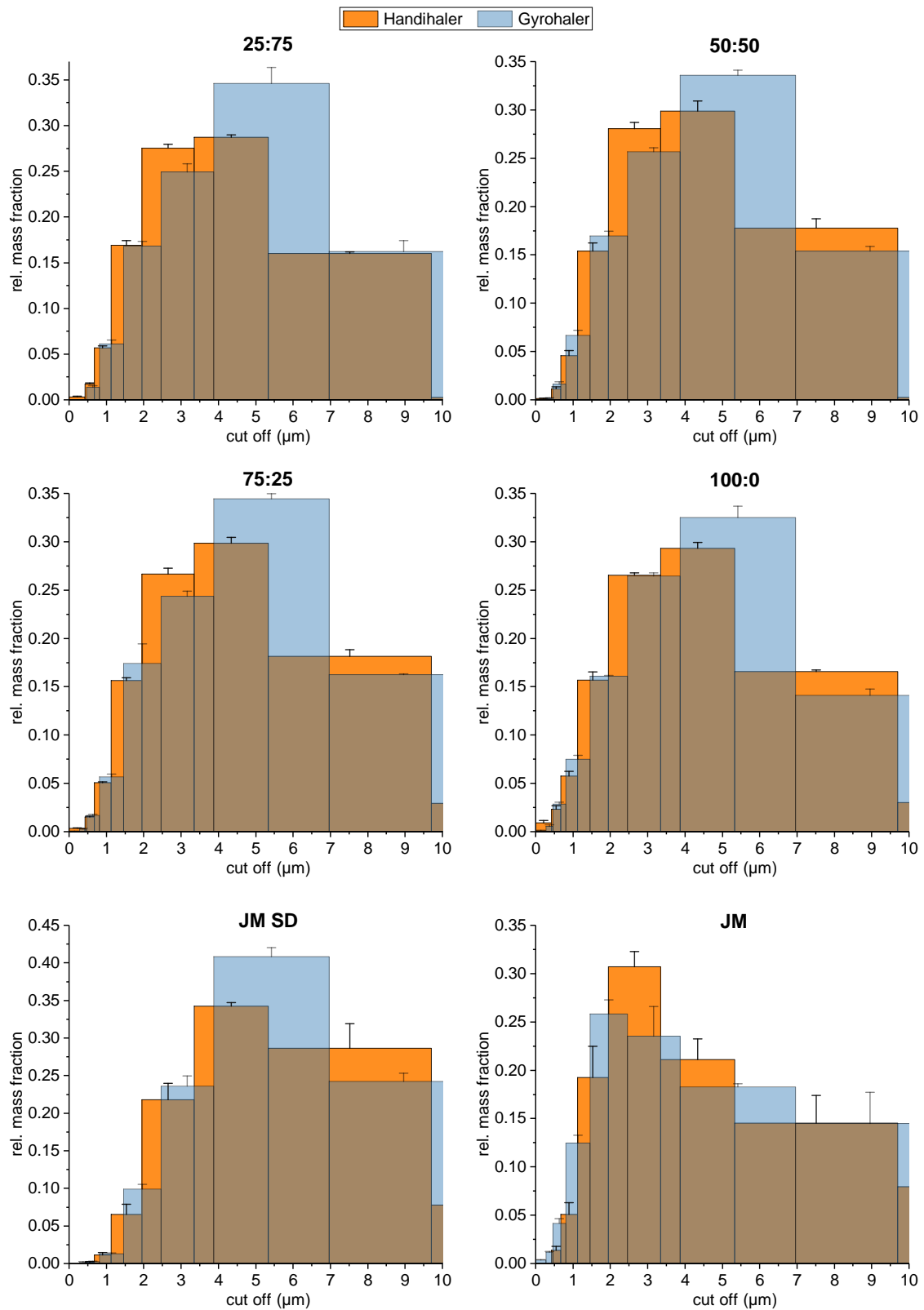


Figure 46: Results of the impaction measurements with the Handihaler® and the Gyrohaler®. Values are expressed as mean \pm SD, n = 3. Mass is related to the recovered mass of the NGI stages (S1-MOC). Number in sample name describes the ratio of ITZ:MAN [%w/w]. JM: jet-milled, JM SD: jet-milled and spray dried.

The highest FPD for ITZ was obtained with the HandiHaler® for formulation 100:0 (\approx 4.1 mg), followed by 75:25 (\approx 3.8 mg) (see Figure 42). The obtained FPFs and FPDs were good compared to carrier-based formulations, where typically a drug load of $<2\%$ is applied resulting in a FPD of less than 1 mg [9,139].

In comparison with other ITZ DPI formulations, Duret et al. (2012) showed a better performance for their ITZ formulation with regard to the FPF (63%) but only a low FPD (1 mg) could be achieved [117]. Another study reported a higher FPD (4.6 mg) for ITZ [140]. However, in this study nanoization was achieved by ionotropic gelation, which might lead to complex scale-up and commercial manufacturing. Wan et al. (2020) achieved a higher FPD (5.1 mg) with a high FPF (71%), but also applied a very special technique for nanoization (flash nanoprecipitation) [119], which might result in a very difficult scale-up and commercial manufacturing process.

To date, no studies are known reporting the combination of media milling and spray drying for the preparation of ITZ dry powders for inhalation. The abovementioned authors applied other manufacturing processes; therefore, the comparability is limited. In this work, only commercially accepted manufacturing techniques with proven upscaling potential were used.

Formulating poorly soluble drugs such as ITZ is often challenging and requires high efforts. The currently marketed spray dried products for high dose drug delivery contain water soluble APIs (Bronchitol® and TOBI® Podhaler®), which are often simpler to formulate. The nano-in-microparticles overcame this hurdle. Furthermore, this formulation principle provides several advantages. Besides the remarkable increase in FPD, this approach offers the potential of an increase in bioavailability [141]. The performance (FPF) of the nano-in-microparticles is comparable to Bronchitol® and TOBI® Podhaler® or slightly lower. The FPD of both marketed products is higher, which could be related to either a higher loaded dose of the capsule, a different design of the device or the formulation [142,143].

Overall, nanoization with subsequent spray drying enabled the generation of high dose formulations for ITZ and can be regarded with good reasons as a very beneficial particle engineering technique. The highest FPD and FPF were obtained with the HandiHaler® for sample 100:0. The FPD of \approx 4 mg is very good compared to carrier-based formulations. The HandiHaler® generated a significantly higher fine particle fraction compared to the GyroHaler®. This was most likely related to the capsule motion of the HandiHaler®, which enhanced the powder aerosolization. For the treatment

of ABPA and IPA, which affects both patients with and without an obstructive disease, the HandiHaler® would be the preferred device as the generated FPDs were significantly higher compared to the GyroHaler®. As the HandiHaler® shows only little flow rate dependency it is even suitable for patients who cannot obtain the required flow rate for 4 kPa pressure drop [36].

3.3.3 Impact of nanoization

For the samples 100:0 (nano-in-microparticles) and JM SD (jet-milled and spray dried), the following conclusions could be made:

- The difference in the aerodynamic behavior of these particular samples was not related to a device as this was observed for both devices.
- The excipients used for stabilization of the nanosuspension are considered to have no impact on the dispersibility and the aerodynamic behavior as both samples had the same composition and content of excipients.

The aerodynamic differences can be explained by the nanoization process step. Nanomilling significantly increased the FPF of a factor of two for the HandiHaler®. Most likely, the reason was the different morphology of the spray dried particles. The spherical nano-in-microparticles showed a spherical morphology with a slightly rough surface, independent of the drug load (see Figure 35). In contrast to this, sample JM which showed a plate-like morphology.

As the aerosolization behavior depends on the particle interaction, it is closely related to surface roughness, particle size and other factors. It is assumed that electrostatic forces and capillary forces play only a minor role at ambient conditions [16]. Increased surface roughness may lead to fewer contact points due to increased asperities, compared to very smooth particles, and thus lower Van der Waals forces. Hence, the aerosolization ability might be improved, as Hassan et al. (2009) showed the highest FPF for pollen-shaped particles as well as Adi et al. (2008) for corrugated bovine serum albumin compared to smooth particles [144,145]. Furthermore, the nano-in-microparticles showed some small indentions (see Figure 35), which could enhance this effect. The circumstance that the nano-in-microparticles were hollow, and exhibited therefore a low density, might support their impaction in the lower respiratory tract as the aerodynamic diameter is highly dependent on the particle density (see Equation 1). The hollow shape with a low density is the typical result of spray dried nano-in-microparticles [22].

The FPF of the nano-in-microparticles was significantly higher than the FPF of sample JM, which exhibited a plate-like morphology (see Figure 35) and a strong agglomeration tendency (shown by pressure titration, see Figure 40), probably due to a high number of contact points and high cohesive forces. Sample JM SD showed spherical particles, however, the surface was very irregular and might favor interlocking, resulting in a low dispersibility [42]. Therefore, this formulation showed the lowest FPF.

Overall, nanoization and subsequent spray drying as particle engineering technique significantly improved the FPF of ITZ formulations, most likely due to an optimized morphology. This effect was more pronounced for the HandiHaler® as the capsule motion supports the deagglomeration by generating high dispersion forces.

3.3.4 Impact of ITZ:MAN ratio

No significant difference was found for the FPFs of various drug loadings of nano-in-microparticles for the HandiHaler®. For experiments with the GyroHaler®, a significant difference was found for the FPFs of the samples with ITZ:MAN ratios 25:75-50:50, 25:75-100:0 and 50:50-100:0. However, this was not associated with a difference in MMAD. It might be the case, that the drug load (i.e., the formulation composition) has an impact on the FPF, which is predominated by the higher dispersion forces generated in the HandiHaler®. Therefore, differences related to the formulation composition may manifest using the GyroHaler® as this device exhibits a lower dispersion force. However, as the difference was only found for some of the samples, it might be also related to analytical variances.

Based on these results, it is assumed that the ITZ:MAN ratio does not distinctly impact the dispersibility and the FPF. Presumably, the effect of the particle-particle interaction of MAN and ITZ was very low compared to the other factors playing a role in the dispersion process.

As discussed in the previous chapter, the main effect that governed the superior aerodynamic behavior of the nano-in-microparticles is presumably attributed to the morphology of the particles, which was similar for the nano-in-microparticles. Other factors, based on the surface composition (e.g., surface energy or capillary forces due to different moisture sorption [146]) had presumably only a minor effect compared to the morphology impact.

This finding, also reported in a study by Yamasaki et al. (2011) [129], who investigated cyclosporine A nanoparticles, showed that different amounts of matrix forming MAN had no effect on the FPF.

The authors explained this with the similarity of the surface roughness of their particles, which was independent from the drug load. However, other authors concluded that the MAN amount has an impact on dispersibility and FPF. Adi et al. (2010) investigated ciprofloxacin [147] and correlated the differing FPF to the diverse cohesion forces in the samples and it was found that increasing MAN contents led to an increase in the FPF. Nevertheless, the authors could not find a mechanistic explanation for the different cohesion as the particles showed a very diverging morphology in addition to the different drug loads investigated. Torge et al. (2017) studied the effect of MAN on PLGA nano-in-microparticles [105]. They attributed the differences to the varying surface texture of the particles without explaining the mechanism detailly.

In conclusion, the ITZ:MAN ratio did not distinctly affect the aerosolization of the nano-in-microparticles. Presumably, other factors (mainly the dispersion force of the device but also particle morphology and surface roughness) overruled the potential effect of the drug load.

3.3.5 Conclusion

The performance of a DPI formulation strongly depends on the interplay between the device, the formulation and the primary packaging material. The formulations showed differences even before the performance evaluation by impaction. Automatic filling with the BI drum filler was possible for the nanosized and spray dried samples but not for samples JM and JM SD because of their strong cohesiveness. This finding was supported by the cascade impaction experiments. Samples JM and JM SD showed a significantly lower FPF and FPD compared to the spray dried nanoparticles. Hence, consecutive nanoization and spray drying seems to be a superior particle engineering technique and enabled the generation of high dose formulations for ITZ up to 4 mg FPD. The highest FPD and FPF were obtained with the HandiHaler® for sample 100:0. The achieved FPD is distinctly higher compared to carrier-based formulations. The reason for the improved dispersibility of the engineered particles was most likely the optimized morphology (low density with a moderately rough surface), as indicated by SEM images. The ITZ:MAN ratio most likely did not affect the aerosolization of the composite ITZ particles. Presumably, other factors (such as particle morphology and surface roughness and the dispersion force of the device) exceeded the potential effect of the drug load.

Furthermore, it could be shown that pressure titration can serve as a valuable screening tool to get a first impression of the dispersion behavior of a formulation. Differentiation between the nano-in-microparticles and the other formulations was possible. However, an in-vitro assessment of the fine particle dose by e.g., cascade impaction is still necessary. The pressure drop in a device is much

lower (4 kPa = 0.04 bar) than the lowest possible dispersion pressure with the laser diffraction method (0.1 bar) and the dispersion mechanisms in devices are different, as shown by the HandiHaler® and the GyroHaler®. The great impact of the device has also been demonstrated. The HandiHaler® generated a significantly higher fine particle fraction compared to the GyroHaler®. This was most likely related to the capsule motion in the HandiHaler®, which enhanced the powder aerosolization.

4 Overall conclusion

The present work describes the development of a high dose dry powder formulation for ITZ for a potential local treatment for respiratory fungal diseases such as ABPA or IPA. It was shown that a combination of media milling and spray drying is a feasible approach to manufacture high dose dry powder formulations of ITZ. With this particle engineering technique, the achievement of a FPD of up to 4 mg ITZ in combination with the HandiHaler® was feasible. An overview of the performance parameters of all formulations investigated is given in Table 16. As indicated by color, the nano-in-microparticles showed superiority for all criteria, whereas formulations JM SD and JM had several liabilities. The nano-in-microparticles could be filled automatically and exhibited FPFs higher than 45% as well as MMADs of below 5 µm. As the FPD depends on the drug loading of the nano-in-microparticles, only formulations 75:25 and 100:0 showed FPDs greater than 2.5 mg, which is considered as high dose. The ITZ:MAN ratio is the key parameter for reconstitution of the nanoparticles. Nearly complete reconstitution was possible up to an ITZ-MAN ratio of 75:25. Therefore, this was preferred ratio of ITZ:MAN with a drug loading of 65%, enabling a balance between a high FPD and reconstitution of the nanoparticles.

Table 16: Performance criteria and rating for the ITZ dry powder formulations. Number in sample name describes the ratio of ITZ:MAN [%w/w]. JM: jet-milled, JM SD: jet-milled and spray dried. N/A: not applicable. Color coding: ■ critical issue, ■ challenge, ■ uncritical

	25:75	50:50	75:25	100:0	JM SD	JM
Automatic filling	■	■	■	■	■	■
FPF > 45% ¹	For Handi-haler®	For Handi-haler®	For Handi-haler®	For Handi-haler®	■	■
FPD > 2.5 mg ²	■	■	For Handi-haler®	For Handi-haler®	■	■
MMAD < 5 µm ³	■	■	■	■	■	■
Reconstitution	■	■	■	■	N/A	N/A

¹threshold was chosen arbitrarily to illustrate a high FPF

²2.5 mg is considered as high dose [8]

³a MMAD of < 5 µm is regarded necessary for inhalation [148]

The FPF and FPD of a formulation highly depends on the interplay between the device and formulation characteristics. Multi-dose devices (such as the GyroHaler®) might improve patients' adherence and show some advantages with regard to humidity-sensitive formulations if they are blister-based. However, the motion of the capsule fosters the deagglomeration of a powder formulation for capsule-based devices and increases the aerosolization. Hence, the HandiHaler® is preferred over the GyroHaler® for delivering the nano-in-microparticles of ITZ.

Additionally, new insights into the development of nanosuspensions of ITZ were gained. It could be shown that the stabilizer concentration did not only affect the particle size of the ITZ nanoparticles but also the solid-state. The reason for the increase in particle size during prolonged milling (i.e., agglomeration) could clearly be identified.

5 Outlook

The ITZ:MAN ratio did presumably not affect the FPF of the nano-in-microparticles. A deeper insight into the effect of the ITZ:MAN ratio might be gained by e.g., atomic force microscopy (AFM) or inverse gas chromatography (IGC), as also used in [129] and [147]. Surface energy and roughness as well as cohesion forces might be quantified for a comprehensive understanding. However, this was not in scope of this work.

Some of the excipients used in this work are considered as model excipients (such as SDS or HPC). HPC has not yet been approved for inhalation but is contained in a marketed nasal dry powder (Teijin Rhinocort®)[149]. Therefore, the respiratory tolerance is considered acceptable though toxicological studies are required to prove this. Although SDS is regarded as inactive ingredient for inhalation by the FDA [150], it may cause irritation after inhalation [151]. Presumably, the use of other non-irritating surfactants is possible if using a nanoization process with lower energy, as reported in literature [117]. Further experiments could also include an investigation on storage stability (e.g., at 25°C/60% rH for 12 months or 40°C/75% rH for 6 months according to the ICH guideline [152]) as temperature and humidity are known to have a remarkable impact on the inhalative performance [31,32]. As mentioned before, the MAN modification in the nano-in-microparticles changed compared to the starting material, which was the thermodynamically most stable form. As a prediction of the modification obtained after spray drying is not possible, the MAN modification in the powders should be monitored.

The achieved FPD of ITZ might be increased with modifications regarding both the device and the formulation. The latter can be modified by addition of leucine before spray drying as this is known as dispersibility enhancing agent [22]. Another approach is the use of pore formers for spray drying. Excipients such as ammonium carbonate or perflubron, which it is used in the Pulmosphere® technology, expand rapidly during the drying step leading to a high number of pores in the final particles [17,153]. This decreases the density and enhances the dispersibility. By using a different device, a further improvement may be realized. A higher loading dose in the capsule and therefore a larger capsule size (larger than size 3) would increase the potential ED. A modified RS01® device with a capsule with a size of 0 has been reported to deliver a FPD of 75 mg tobramycin [154]. The Aerolizer® has also been modified with regard to the capsule compartment (for size 0), the air-inlet opening and the capsule piercing. With this set-up, a FPD of above 50 mg for tobramycin could be obtained [155,156].

To obtain a better estimation of the *in-vivo* fate of the engineered particles, the reconstitution experiments could be conducted using more biorelevant conditions as e.g., described by Ruge et al. (2016), who used a model mucus [157]. However, this was not in scope of this work. Additionally, a simulated lung fluid could be used [105]. The cascade impaction experiments were set-up as described in the Pharmacopoeia as *in-vitro* trials. The biorelevance could be improved by using anatomical throats such as the Alberta idealized throat [30].

6 Summary

Fungal infections of the respiratory tract are widely spread as over one billion people suffer from fungal infections. Infections caused by *Aspergillus sp.* can manifest differently depending on the immune status of the patients. A hypersensitivity reaction causes allergic bronchopulmonary aspergillosis (ABPA), whereas life-threatening invasive pulmonary aspergillosis (IPA) can also occur. Itraconazole (ITZ) is considered as first-line therapy against ABPA and also used against IPA. To date, only systemic treatments with ITZ exist, that are often associated with tolerability and safety issues. Thus, local treatment of these infections is regarded beneficial as it might reduce systemic side effects. Significantly higher doses compared to those applied in asthma or COPD therapy are demanded. Therefore, particle engineering with the aim of developing a carrier-free, high dose powder formulation with excellent dispersibility is required. The combination of media milling and spray drying enables the generation of tailored spherical particles with low density in a desired particle size range and with a defined surface structure and an API in a crystalline state.

Nanocrystals of ITZ were stabilized by electrosteric stabilization using hydroxypropyl cellulose (HPC-SL), sodium dodecyl sulfate (SDS) and polysorbate 80 (PS80) and the impact of formulation and process parameters of a dual centrifugal mill on material attributes like particle size, zeta potential, particle morphology, storage stability and especially solid-state characteristics was evaluated. A concentration of 0.9% (w/w) HPC-SL, 0.14% (w/w) SDS and 0.14% (w/w) PS80 was necessary for a sufficient nanoparticle stabilization. Despite the minor effect of PS80 its presence was beneficial for the electrosteric stabilization. Choosing lower stabilizer concentrations resulted in a pronounced increase in particle size due to agglomeration, which was confirmed by SEM imaging and a decrease in zeta potential in combination with an amorphization of the particles. Milling temperature had no significant impact on the particle size whereas milling speed and the size of the milling beads used were found to have a strong impact on the critical material attributes such as particle size and polydispersity index. The smallest particle sizes could be obtained by using the smallest milling bead size. However, the smallest obtainable particle size could be only achieved by using two-fold stabilizer concentrations as smaller particles exhibit a larger specific surface area.

Process evaluation of spray drying revealed an outlet temperature of 60 °C, a nozzle gas flow rate of 23 SL/min and a feed rate of 5 g/min as optimized parameters. Nanoization and spray drying led to spherical, hollow, low-density nano-in-microparticles (ITZ nanoparticles with mannitol (MAN) as matrix former) with poor powder flow characteristics, regardless of the drug load. Both ITZ and MAN were found in crystalline state after spray drying, although less stable forms of MAN were

present as the suspended ITZ particles might favor the formation of the metastable α - and δ -polymorphic forms of MAN. However, these forms were stable after vapor sorption, which showed water adsorption correlated to the HPC-SL content in the samples as MAN and ITZ were not hygroscopic.

The evaluation of dispersibility by laser diffraction (pressure titration) demonstrated that nanoization and consecutive spray drying as a particle engineering technique enables the generation of particles with an excellent dispersibility. Furthermore, the drug load most likely did not affect the dispersibility, which means that even formulations with up to 84% ITZ may be delivered to the lung efficiently. Samples JM and JM SD showed a significantly worse dispersibility highlighting the benefits of nanoization. Pressure titration can serve as a valuable screening tool to get a first impression of the dispersion behavior of a formulation. However, an in-vitro assessment of the fine particle dose by e.g., cascade impaction is still necessary as dispersion pressures and mechanisms are different. The latter was also shown by cascade impaction. The performance of a DPI formulation strongly depends on the interplay between the device, the formulation, and the primary packaging material. The formulations showed differences even before the performance evaluation by impaction. Automatic filling with the BI drum filler was possible for the nano-in-microparticles but not for samples JM and JM SD because of their strong cohesiveness. This finding was supported by the cascade impaction experiments. Samples JM and JM SD showed a significantly lower FPF (fine particle fraction) and FPD (fine particle dose) compared to the nano-in-microparticles. Hence, consecutive nanoization and spray drying seems to be a superior particle engineering technique and enabled the generation of high dose formulations for ITZ up to 4 mg FPD. The highest FPD and FPF were obtained with the HandiHaler® for sample 100:0: The achieved FPD is distinctly higher compared to carrier-based formulations. The reason for the improved dispersibility of the engineered particles was most likely the optimized morphology (low density with a slightly rough surface), as indicated by SEM images. The ITZ:MAN ratio most likely did not affect the aerosolization of the composite ITZ particles. Presumably, other factors (such as particle morphology, surface roughness and the dispersion force of the device) exceeded the potential effect of the drug load. However, the MAN content in the nano-in-microparticles highly affected the reconstitution of the nanoparticles in water. The higher the MAN content was, the faster was the reconstitution. The sample containing no MAN also showed reconstitution to a certain extent indicating spray drying had no negative impact on the nanoparticle size. An ITZ:MAN ratio of 75:25 (resulting in a drug loading of 65% (w/w) ITZ) was the preferred formulation as this enables a balance between a high FPD and nearly complete reconstitution of the nanoparticles.

The great impact of the device has also been demonstrated. The HandiHaler® generated a significantly higher FPF compared to the GyroHaler®. This was most likely related to the capsule motion in the HandiHaler®, which enhanced the powder aerosolization. Thus, the HandiHaler® is preferred over the GyroHaler® for delivering the nano-in-microparticles of ITZ.

7 References

- [1] F. Palmieri, A. Koutsokera, E. Bernasconi, P. Junier, C. von Garnier, N. Ubags, Recent Advances in Fungal Infections: From Lung Ecology to Therapeutic Strategies With a Focus on *Aspergillus* spp., *Frontiers Medicine*. 9 (2022) 832510. <https://doi.org/10.3389/fmed.2022.832510>.
- [2] F. Bongomin, S. Gago, R. Oladele, D. Denning, Global and Multi-National Prevalence of Fungal Diseases—Estimate Precision, *J Fungi*. 3 (2017) 57. <https://doi.org/10.3390/jof3040057>.
- [3] S. Gago, D.W. Denning, P. Bowyer, Pathophysiological aspects of *Aspergillus* colonization in disease, *Med Mycol*. 57 (2018) S219–S227. <https://doi.org/10.1093/mmy/myy076>.
- [4] J.-P. Latgé, G. Chamilos, *Aspergillus fumigatus* and Aspergillosis in 2019, *Clin Microbiol Rev*. 33 (2019). <https://doi.org/10.1128/cmr.00140-18>.
- [5] C. Rundfeldt, H. Steckel, H. Scherliess, E. Wyska, P. Wlaź, Inhalable highly concentrated itraconazole nanosuspension for the treatment of bronchopulmonary aspergillosis, *European Journal of Pharmaceutics and Biopharmaceutics*. 83 (2013) 44–53. <https://doi.org/http://dx.doi.org/10.1016/j.ejpb.2012.09.018>.
- [6] S.N. Cheng, Z.G. Tan, M. Pandey, T. Srichana, M.R. Pichika, B. Gorain, H. Choudhury, A Critical Review on Emerging Trends in Dry Powder Inhaler Formulation for the Treatment of Pulmonary Aspergillosis, *Pharm*. 12 (2020) 1161. <https://doi.org/10.3390/pharmaceutics12121161>.
- [7] T.F. Patterson, G.R. Thompson, D.W. Denning, J.A. Fishman, S. Hadley, R. Herbrecht, D.P. Kontoyiannis, K.A. Marr, V.A. Morrison, M.H. Nguyen, B.H. Segal, W.J. Steinbach, D.A. Stevens, T.J. Walsh, J.R. Wingard, J.-A.H. Young, J.E. Bennett, Practice Guidelines for the Diagnosis and Management of Aspergillosis: 2016 Update by the Infectious Diseases Society of America, *Clin Infect Dis*. 63 (2016) e1–e60. <https://doi.org/10.1093/cid/ciw326>.
- [8] I. Sibum, P. Hagedoorn, A.H. de Boer, H.W. Frijlink, F. Grasmeijer, Challenges for pulmonary delivery of high powder doses, *Int. J. of Pharmaceutics*. 548 (2018) 325–336. <https://doi.org/https://doi.org/10.1016/j.ijpharm.2018.07.008>.
- [9] R. Scherließ, C. Etschmann, DPI formulations for high dose applications – Challenges and opportunities, *Int. J. of Pharmaceutics*. 548 (2018) 49–53. <https://doi.org/https://doi.org/10.1016/j.ijpharm.2018.06.038>.
- [10] S. Claus, C. Weiler, J. Schiewe, W. Friess, How can we bring high drug doses to the lung?, *European Journal of Pharmaceutics and Biopharmaceutics*. 86 (2014) 1–6. <https://doi.org/http://dx.doi.org/10.1016/j.ejpb.2013.11.005>.
- [11] A.D. Brunaugh, H.D.C. Smyth, Formulation techniques for high dose dry powders, *Int. J. of Pharmaceutics*. 547 (2018) 489–498. <https://doi.org/https://doi.org/10.1016/j.ijpharm.2018.05.036>.
- [12] A.H.L. Chow, H.H.Y. Tong, P. Chattopadhyay, B.Y. Shekunov, Particle Engineering for Pulmonary Drug Delivery, *Pharmaceut Res*. 24 (2007) 411–437. <https://doi.org/10.1007/s11095-006-9174-3>.

- [13] A.M. Healy, M.I. Amaro, K.J. Paluch, L. Tajber, Dry powders for oral inhalation free of lactose carrier particles, *Adv Drug Deliver Rev.* 75 (2014) 32–52. <https://doi.org/10.1016/j.addr.2014.04.005>.
- [14] A.H. de Boer, P. Hagedoorn, M. Hoppentocht, F. Buttini, F. Grasmeyer, H.W. Frijlink, Dry powder inhalation: past, present and future, *Expert Opin Drug Del.* 14 (2017) 499–512. <https://doi.org/10.1080/17425247.2016.1224846>.
- [15] W. Kaialy, A. Nokhodchi, Particle Engineering for Improved Pulmonary Drug Delivery Through Dry Powder Inhalers, in: John Wiley & Sons, Ltd, 2015: pp. 171–198. <https://doi.org/10.1002/9781118799536.ch8>.
- [16] J.G. Weers, D.P. Miller, Formulation Design of Dry Powders for Inhalation, *Journal of Pharmaceutical Sciences.* 104 (2015) 3259–3288. <https://doi.org/http://dx.doi.org/10.1002/jps.24574>.
- [17] D.E. Geller, J. Weers, S. Heurding, Development of an Inhaled Dry-Powder Formulation of Tobramycin Using PulmoSphere™ Technology, *J Aerosol Med Pulm D.* 24 (2011) 175–182. <https://doi.org/10.1089/jamp.2010.0855>.
- [18] K. Berkenfeld, A. Lamprecht, J.T. McConville, Devices for Dry Powder Drug Delivery to the Lung, *AAPS Pharmscitech.* 16 (2015) 479–490. <https://doi.org/10.1208/s12249-015-0317-x>.
- [19] D.A. Edwards, J. Hanes, G. Caponetti, J. Hrkach, A. Ben-Jebria, M.L. Eskew, J. Mintzes, D. Deaver, N. Lotan, R. Langer, Large Porous Particles for Pulmonary Drug Delivery, *Science.* 276 (1997) 1868–1872. <https://doi.org/10.1126/science.276.5320.1868>.
- [20] N. Anton, A. Jakhmola, T.F. Vandamme, Trojan Microparticles for Drug Delivery, *Pharm.* 4 (2012) 1–25. <https://doi.org/10.3390/pharmaceutics4010001>.
- [21] B.Y. Shekunov, P. Chattopadhyay, H.H.Y. Tong, A.H.L. Chow, Particle Size Analysis in Pharmaceuticals: Principles, Methods and Applications, *Pharmaceut Res.* 24 (2007) 203–227. <https://doi.org/10.1007/s11095-006-9146-7>.
- [22] R. Scherließ, S. Bock, N. Bungert, A. Neustock, L. Valentin, Particle engineering in dry powders for inhalation, *Eur J Pharm Sci.* 172 (2022) 106158. <https://doi.org/10.1016/j.ejps.2022.106158>.
- [23] M. Malamataris, A. Charisi, S. Malamataris, K. Kachrimanis, I. Nikolakakis, Spray Drying for the Preparation of Nanoparticle-Based Drug Formulations as Dry Powders for Inhalation, *Process.* 8 (2020) 788. <https://doi.org/10.3390/pr8070788>.
- [24] R.K. Verma, M. Ibrahim, L. Garcia-Contreras, Lung Anatomy and Physiology and Their Implications for Pulmonary Drug Delivery, in: John Wiley & Sons, Ltd, 2015: pp. 1–18. <https://doi.org/10.1002/9781118799536.ch1>.
- [25] A. Hickey, *Pharmaceutical Inhalation Aerosol Technology*, 2nd Edition, CRC Press, 2003. <https://doi.org/https://doi.org/10.1201/9780203912898>.

- [26] B. Olsson, E. Bondesson, L. Borgström, S. Edsbäcker, S. Eirefelt, K. Ekelund, L. Gustavsson, T. Hegelund-Myrbäck, Pulmonary Drug Metabolism, Clearance, and Absorption, in: *Controlled Pulmonary Drug Delivery*, Springer New York, New York, NY, 2011: pp. 21–50. https://doi.org/10.1007/978-1-4419-9745-6_2.
- [27] R. Vehring, Pharmaceutical Particle Engineering via Spray Drying, *Pharmaceut Res.* 25 (2008) 999–1022. <https://doi.org/10.1007/s11095-007-9475-1>.
- [28] N. Tsapis, D. Bennett, B. Jackson, D.A. Weitz, D.A. Edwards, Trojan particles: Large porous carriers of nanoparticles for drug delivery, *Proceedings of the National Academy of Sciences.* 99 (2002) 12001.
- [29] A.J. Hickey, *Fundamentals of Dry Powder Inhaler Technology*, in: Springer International Publishing, Cham, 2018: pp. 213–232. https://doi.org/10.1007/978-3-319-94174-5_5.
- [30] K. Berkenfeld, Particle engineered inhalable dry powders of rifampicin, University of Bonn, 2019.
- [31] W.C. Hinds, *Aerosol Technology: Properties, Behavior, and Measurement of Airborne Particles*, John Wiley & Sons, Inc, Somerset, USA, 1999.
- [32] M.J. Telko, A.J. Hickey, Dry Powder Inhaler Formulation, *Respiratory Care.* 50 (2005) 1209–1227.
- [33] Y. Ye, Y. Ma, J. Zhu, The future of dry powder inhaled therapy: Promising or Discouraging for systemic disorders?, *Int J Pharmaceut.* 614 (2022) 121457. <https://doi.org/10.1016/j.ijpharm.2022.121457>.
- [34] A.R. Clark, J.G. Weers, R. Dhand, The Confusing World of Dry Powder Inhalers: It Is All About Inspiratory Pressures, Not Inspiratory Flow Rates, *J Aerosol Med Pulm D.* 33 (2020) 1–11. <https://doi.org/10.1089/jamp.2019.1556>.
- [35] A.R. Clark, A.M. Hollingworth, The Relationship Between Powder Inhaler Resistance and Peak Inspiratory Conditions in Healthy Volunteers — Implications for In Vitro Testing, *J Aerosol Medicine.* 6 (1993) 99–110. <https://doi.org/10.1089/jam.1993.6.99>.
- [36] S. Chodosh, J.S. Flanders, S. Kesten, C.W. Serby, D. Hochrainer, T.J. Witek, Effective Delivery of Particles with the HandiHaler Dry Powder Inhalation System over a Range of Chronic Obstructive Pulmonary Disease Severity, *J Aerosol Medicine.* 14 (2001) 309–315. <https://doi.org/10.1089/089426801316970268>.
- [37] J.C. Virchow, T. Weuthen, Q.J. Harmer, S. Jones, Identifying the features of an easy-to-use and intuitive dry powder inhaler for asthma and chronic obstructive pulmonary disease therapy: Results from a 28-day device handling study, and an airflow resistance study, *Expert Opin Drug Del.* 11 (2014) 1849–1857. <https://doi.org/10.1517/17425247.2014.949236>.
- [38] H. Wachtel, *Respiratory Drug Delivery*, (2016) 257–274. https://doi.org/10.1007/978-3-319-26920-7_9.

- [39] M.P.A. Sveden, Public Assessment Report Scientific discussion, Airflusal Forspiro, (2013). https://docetp.mpa.se/LMF/Airflusal%20Forspiro,%20inhalation%20powder,%20pre-dispensed%20ENG%20PAR_09001be68046a13b.pdf (accessed May 7, 2022).
- [40] J. Weers, A. Clark, The Impact of Inspiratory Flow Rate on Drug Delivery to the Lungs with Dry Powder Inhalers, *Pharmaceut Res.* 34 (2017) 507–528. <https://doi.org/10.1007/s11095-016-2050-x>.
- [41] A.S. Barham, F. Tewes, A.M. Healy, Moisture diffusion and permeability characteristics of hydroxypropylmethylcellulose and hard gelatin capsules, *Int J Pharmaceut.* 478 (2015) 796–803. <https://doi.org/10.1016/j.ijpharm.2014.12.029>.
- [42] C. Weiler, M. Egen, M. Trunk, P. Langguth, Force control and powder dispersibility of spray dried particles for inhalation, *J Pharm Sci.* 99 (2010) 303–316. <https://doi.org/10.1002/jps.21849>.
- [43] J. Visser, Van der Waals and other cohesive forces affecting powder fluidization, *Powder Technol.* 58 (1989) 1–10. [https://doi.org/10.1016/0032-5910\(89\)80001-4](https://doi.org/10.1016/0032-5910(89)80001-4).
- [44] M. Becker, Experimentelle & numerische Untersuchung des Pulver- & Aerosolverhaltens in einer Luftströmung, TU Darmstadt, 2013.
- [45] A. Noyes, W.R. Whitney, The rate of solution of solid substances in their own solutions, *J Am Chem Soc.* 19 (1897) 930–934. <https://doi.org/10.1021/ja02086a003>.
- [46] M. Li, M. Azad, R. Davé, E. Bilgili, Nanomilling of Drugs for Bioavailability Enhancement: A Holistic Formulation-Process Perspective, *Pharm.* 8 (2016) 17. <https://doi.org/10.3390/pharmaceutics8020017>.
- [47] B.E. Rabinow, Nanosuspensions in drug delivery, *Nat Rev Drug Discov.* 3 (2004) 785–796. <https://doi.org/10.1038/nrd1494>.
- [48] W. Ostwald, Studien über die Bildung und Umwandlung fester Körper, *Zeitschrift Für Physikalische Chemie.* 22 (1897) 289–330. <https://doi.org/https://doi.org/10.1515/zpch-1897-2233>.
- [49] J. Li, Z. Wang, H. Zhang, J. Gao, A. Zheng, Progress in the development of stabilization strategies for nanocrystal preparations, *Drug Deliv.* 28 (2020) 19–36. <https://doi.org/10.1080/10717544.2020.1856224>.
- [50] S. Verma, S. Kumar, R. Gokhale, D.J. Burgess, Physical stability of nanosuspensions: Investigation of the role of stabilizers on Ostwald ripening, *Int. J. of Pharmaceutics.* 406 (2011) 145–152. <https://doi.org/https://doi.org/10.1016/j.ijpharm.2010.12.027>.
- [51] B.V. Derjaguin, L. Landau, Theory of the stability of strongly charged lyophobic sols and of the adhesion of strongly charged particles in solution of electrolytes, *Acta Physicochim: USSR.* 14 (1941) 633–662.
- [52] E.J.W. Verwey, Theory of the Stability of Lyophobic Colloids, *J Phys Colloid Chem.* 51 (1947) 631–636. <https://doi.org/10.1021/j150453a001>.

- [53] B.V. Eerdenbrugh, G.V. den Mooter, P. Augustijns, Top-down production of drug nanocrystals: Nanosuspension stabilization, miniaturization and transformation into solid products, *Int. J. of Pharmaceutics*. 364 (2008) 64–75. <https://doi.org/https://doi.org/10.1016/j.ijpharm.2008.07.023>.
- [54] K.J. Frank, G. Boeck, Development of a nanosuspension for iv administration: From miniscale screening to a freeze dried formulation, *Eur J Pharm Sci*. 87 (2016) 112–117. <https://doi.org/10.1016/j.ejps.2016.03.003>.
- [55] K. Masters, *Spray drying handbook*, 5th ed., Longman Scientific & Technical [u.a.], Harlow, 1991.
- [56] J. Elversson, *Spray-Dried Powders for Inhalation: Particle Formation and Formulation Concepts*, 2005.
- [57] S. Kooij, R. Sijs, M.M. Denn, E. Villermaux, D. Bonn, What Determines the Drop Size in Sprays?, *Phys Rev X*. 8 (2018) 031019. <https://doi.org/10.1103/physrevx.8.031019>.
- [58] E. Boel, R. Koekoekx, S. Dedroog, I. Babkin, M.R. Vetrano, C. Clasen, G.V. den Mooter, Unraveling Particle Formation: From Single Droplet Drying to Spray Drying and Electrospraying, *Pharm*. 12 (2020) 625. <https://doi.org/10.3390/pharmaceutics12070625>.
- [59] M. Mezhericher, A. Levy, I. Borde, Spray drying modelling based on advanced droplet drying kinetics, *Chem Eng Process Process Intensif*. 49 (2010) 1205–1213. <https://doi.org/10.1016/j.cep.2010.09.002>.
- [60] E.M. Littringer, R. Paus, A. Mescher, H. Schroettner, P. Walzel, N.A. Urbanetz, The morphology of spray dried mannitol particles — The vital importance of droplet size, *Powder Technology*. 239 (2013) 162–174. <https://doi.org/https://doi.org/10.1016/j.powtec.2013.01.065>.
- [61] R. Vehring, W.R. Foss, D. Lechuga-Ballesteros, Particle formation in spray drying, *Journal of Aerosol Science*. 38 (2007) 728–746. <https://doi.org/https://doi.org/10.1016/j.jaerosci.2007.04.005>.
- [62] K. Almansour, I.M. Alfagih, R. Ali, M.M.A. Elsayed, Inhalable microparticles containing terbinafine for management of pulmonary fungal infections: Spray drying process engineering using lactose vs. mannitol as excipients, *J Drug Deliv Sci Tec*. 60 (2020) 101991. <https://doi.org/10.1016/j.jddst.2020.101991>.
- [63] K. Six, T. Daems, J. de Hoon, A.V. Hecken, M. Depre, M.-P. Bouche, P. Prinsen, G. Verreck, J. Peeters, M.E. Brewster, G.V. den Mooter, Clinical study of solid dispersions of itraconazole prepared by hot-stage extrusion, *Eur J Pharm Sci*. 24 (2005) 179–186. <https://doi.org/10.1016/j.ejps.2004.10.005>.
- [64] S. Hou, J. Wu, X. Li, H. Shu, Practical, regulatory and clinical considerations for development of inhalation drug products, *Asian Journal of Pharmaceutical Sciences*. 10 (2015) 490–500. <https://doi.org/http://dx.doi.org/10.1016/j.ajps.2015.08.008>.
- [65] F. Martinelli, A.G. Balducci, A. Rossi, F. Sonvico, P. Colombo, F. Buttini, “Pierce and inhale” design in capsule based dry powder inhalers: Effect of capsule piercing and motion on aerodynamic

performance of drugs, *Int. J. of Pharmaceutics*. 487 (2015) 197–204.

<https://doi.org/https://doi.org/10.1016/j.ijpharm.2015.04.003>.

[66] J. Shur, S. Lee, W. Adams, R. Lionberger, J. Tibbatts, R. Price, Effect of Device Design on the In Vitro Performance and Comparability for Capsule-Based Dry Powder Inhalers, *AAPS J.* 14 (2012) 667–676. <https://doi.org/10.1208/s12248-012-9379-9>.

[67] M.J. Donovan, S.H. Kim, V. Raman, H.D. Smyth, Dry Powder Inhaler Device Influence on Carrier Particle Performance, *J Pharm Sci.* 101 (2012) 1097–1107. <https://doi.org/10.1002/jps.22824>.

[68] C. Reece, P. Swanbury, An Overview of the Design Verification Testing Process for the Gyro-Haler® Dry Powder Inhaler, in: MARY ANN LIEBERT, INC 140 HUGUENOT STREET, 3RD FL, NEW ROCHELLE, NY 10801 USA, 2015: pp. A24–A24. <https://ddl-conference.com/ddl25-2014/conference-papers/overview-design-verification-testing-process-gyrohaler-dry-powder-inhaler/>.

[69] H.W. Howe, J.J. Warriner, A.M. Cook, S.L. Coguille, L.C. Farrar, Method for resonant-vibratory mixing, US 7,866,878 B2, 2011.

[70] R. Tanaka, N. Takahashi, Y. Nakamura, Y. Hattori, K. Ashizawa, M. Otsuka, Verification of the mixing processes of the active pharmaceutical ingredient, excipient and lubricant in a pharmaceutical formulation using a resonant acoustic mixing technology, *Rsc Adv.* 6 (2016) 87049–87057. <https://doi.org/10.1039/c6ra16209f>.

[71] M. Hagedorn, A. Bögershausen, M. Rischer, R. Schubert, U. Massing, Dual centrifugation – A new technique for nanomilling of poorly soluble drugs and formulation screening by an DoE-approach, *Int. J. of Pharmaceutics*. 530 (2017) 79–88. <https://doi.org/https://doi.org/10.1016/j.ijpharm.2017.07.047>.

[72] M. Hagedorn, L. Liebich, A. Bögershausen, U. Massing, S. Hoffmann, S. Mende, M. Rischer, Rapid development of API nano-formulations from screening to production combining dual centrifugation and wet agitator bead milling, *Int. J. of Pharmaceutics*. 565 (2019) 187–198. <https://doi.org/https://doi.org/10.1016/j.ijpharm.2019.04.082>.

[73] F. Eskandar, M. Lejeune, S. Edge, Low powder mass filling of dry powder inhalation formulations, *Drug Dev Ind Pharm.* 37 (2010) 24–32. <https://doi.org/10.3109/03639045.2010.489561>.

[74] L. Peltonen, Practical guidelines for the characterization and quality control of pure drug nanoparticles and nano-cocrystals in the pharmaceutical industry, *Advanced Drug Delivery Reviews*. 131 (2018) 101–115. <https://doi.org/https://doi.org/10.1016/j.addr.2018.06.009>.

[75] C.M. Keck, Cyclosporine nanosuspensions: Optimised size characterisation & oral formulations, 2006.

[76] A. Burger, J.-O. Henck, S. Hetz, J.M. Rollinger, A.A. Weissnicht, H. Stöttner, Energy/Temperature Diagram and Compression Behavior of the Polymorphs of D-Mannitol, *J Pharm Sci.* 89 (2000) 457–468. [https://doi.org/10.1002/\(sici\)1520-6017\(200004\)89:4<457::aid-jps3>3.0.co;2-g](https://doi.org/10.1002/(sici)1520-6017(200004)89:4<457::aid-jps3>3.0.co;2-g).

- [77] U. Teipel, Problems in Characterizing Transparent Particles by Laser Light Diffraction Spectrometry, *Chem Eng Technol.* 25 (2002) 13–21. [https://doi.org/10.1002/1521-4125\(200201\)25:1<13::aid-ceat13>3.0.co;2-a](https://doi.org/10.1002/1521-4125(200201)25:1<13::aid-ceat13>3.0.co;2-a).
- [78] S. Jaffari, B. Forbes, E. Collins, D.J. Barlow, G.P. Martin, D. Murnane, Rapid characterisation of the inherent dispersibility of respirable powders using dry dispersion laser diffraction, *Int. J. of Pharmaceutics.* 447 (2013) 124–131. <https://doi.org/http://dx.doi.org/10.1016/j.ijpharm.2013.02.034>.
- [79] A.M. Cerdeira, M. Mazzotti, B. Gander, Formulation and drying of miconazole and itraconazole nanosuspensions, *Int. J. of Pharmaceutics.* 443 (2013) 209–220. <https://doi.org/https://doi.org/10.1016/j.ijpharm.2012.11.044>.
- [80] C. of Europe, *European Pharmacopoeia (Ph. Eur.), Supplement 10.1*, Strasbourg, 2020.
- [81] Boehringer Ingelheim Pharma GmbH & Co. KG, *Gebrauchsinformation: Information für Patienten Spiriva® 18 Mikrogramm*, (2017). <https://www.boehringer-interaktiv.de/basisinformation-spiriva-bei-copd> (accessed April 17, 2020).
- [82] Hexal AG, *Gebrauchsinformation: Information für Patienten Airflusal® Forspiro® 50 Mikrogramm/500 Mikrogramm/Dosis*, (2019). https://www.hexal.biz/praeparate/dokumente/gi/airflusal_forspiro_gi-1617796215.pdf (accessed April 22, 2020).
- [83] A.-C. Willmann, K. Berkenfeld, T. Faber, H. Wachtel, G. Boeck, K.G. Wagner, Itraconazole Nanosuspensions via Dual Centrifugation Media Milling: Impact of Formulation and Process Parameters on Particle Size and Solid-State Conversion as Well as Storage Stability, *Pharm.* 14 (2022) 1528. <https://doi.org/10.3390/pharmaceutics14081528>.
- [84] C. Knieke, M. Sommer, W. Peukert, Identifying the apparent and true grinding limit, *Powder Technology.* 195 (2009) 25–30. <https://doi.org/https://doi.org/10.1016/j.powtec.2009.05.007>.
- [85] S. Kumar, X. Xu, R. Gokhale, D.J. Burgess, Formulation parameters of crystalline nanosuspensions on spray drying processing: A DoE approach, *Int J Pharmaceut.* 464 (2014) 34–45. <https://doi.org/10.1016/j.ijpharm.2014.01.013>.
- [86] R.C. Rowe, P.J. Sheskey, P.J. Weller, *Handbook of Pharmaceutical Excipients*, 4th ed., Pharmaceutical Press, 2003.
- [87] L. Peltonen, J. Hirvonen, Pharmaceutical nanocrystals by nanomilling: critical process parameters, particle fracturing and stabilization methods, *J Pharm Pharmacol.* 62 (2010) 1569–1579. <https://doi.org/10.1111/j.2042-7158.2010.01022.x>.
- [88] A. Kwade, Determination of the most important grinding mechanism in stirred media mills by calculating stress intensity and stress number, *Powder Technol.* 105 (1999) 382–388. [https://doi.org/10.1016/s0032-5910\(99\)00162-x](https://doi.org/10.1016/s0032-5910(99)00162-x).
- [89] M. Gao, E. Forssberg, Prediction of product size distributions for a stirred ball mill, *Powder Technology.* 84 (1995) 101–106. [https://doi.org/http://dx.doi.org/10.1016/0032-5910\(95\)02990-J](https://doi.org/http://dx.doi.org/10.1016/0032-5910(95)02990-J).

- [90] A. Kwade, J. Schwedes, Wet Comminution in Stirred Media Mills, Kona Powder Part J. 15 (1997) 91–102. <https://doi.org/10.14356/kona.1997013>.
- [91] M. Li, P. Alvarez, E. Bilgili, A microhydrodynamic rationale for selection of bead size in preparation of drug nanosuspensions via wet stirred media milling, *Int. J. of Pharmaceutics*. 524 (2017) 178–192. <https://doi.org/https://doi.org/10.1016/j.ijpharm.2017.04.001>.
- [92] A. Kumar, C.K. Dixit, Methods for characterization of nanoparticles, *Advances in Nanomedicine for the Delivery of Therapeutic Nucleic Acids*. (2017) 43–58. <https://doi.org/10.1016/b978-0-08-100557-6.00003-1>.
- [93] J.W. Gibbs, A method of geometrical representation of the thermodynamic properties by means of surfaces, *Transactions of Connecticut Academy of Arts and Sciences*. (1873) 382–404.
- [94] A. Bitterlich, C. Laabs, I. Krautstrunk, M. Dengler, M. Juhnke, A. Grandeury, H. Bunjes, A. Kwade, Process parameter dependent growth phenomena of naproxen nanosuspension manufactured by wet media milling, *European Journal of Pharmaceutics and Biopharmaceutics*. 92 (2015) 171–179. <https://doi.org/https://doi.org/10.1016/j.ejpb.2015.02.031>.
- [95] S. Kumar, D.J. Burgess, Wet milling induced physical and chemical instabilities of naproxen nano-crystalline suspensions, *Int. J. of Pharmaceutics*. 466 (2014) 223–232. <https://doi.org/https://doi.org/10.1016/j.ijpharm.2014.03.021>.
- [96] I. Colombo, G. Grassi, M. Grassi, Drug mechanochemical activation, *J Pharm Sci*. 98 (2009) 3961–3986. <https://doi.org/10.1002/jps.21733>.
- [97] Z. Deng, S. Xu, S. Li, Understanding a relaxation behavior in a nanoparticle suspension for drug delivery applications, *Int. J. of Pharmaceutics*. 351 (2008) 236–243. <https://doi.org/https://doi.org/10.1016/j.ijpharm.2007.10.001>.
- [98] G. Verreck, K. Six, G.V. den Mooter, L. Baert, J. Peeters, M.E. Brewster, Characterization of solid dispersions of itraconazole and hydroxypropylmethylcellulose prepared by melt extrusion—part I, *Int. J. of Pharmaceutics*. 251 (2003) 165–174. [https://doi.org/https://doi.org/10.1016/S0378-5173\(02\)00591-4](https://doi.org/https://doi.org/10.1016/S0378-5173(02)00591-4).
- [99] K. Six, G. Verreck, J. Peeters, K. Binnemans, H. Berghmans, P. Augustijns, R. Kinget, G.V. den Mooter, Investigation of thermal properties of glassy itraconazole: identification of a monotropic mesophase, *Thermochimica Acta*. 376 (2001) 175–181. [https://doi.org/https://doi.org/10.1016/S0040-6031\(01\)00563-9](https://doi.org/https://doi.org/10.1016/S0040-6031(01)00563-9).
- [100] W. Yang, K.P. Johnston, R.O. Williams, Comparison of bioavailability of amorphous versus crystalline itraconazole nanoparticles via pulmonary administration in rats, *European Journal of Pharmaceutics and Biopharmaceutics*. 75 (2010) 33–41. <https://doi.org/https://doi.org/10.1016/j.ejpb.2010.01.011>.
- [101] P. Sharma, W.A. Denny, S. Garg, Effect of wet milling process on the solid state of indomethacin and simvastatin, *Int. J. of Pharmaceutics*. 380 (2009) 40–48. <https://doi.org/https://doi.org/10.1016/j.ijpharm.2009.06.029>.

- [102] M. Azad, C. Arteaga, B. Abdelmalek, R. Davé, E. Bilgili, Spray drying of drug-swellable dispersant suspensions for preparation of fast-dissolving, high drug-loaded, surfactant-free nanocomposites, *Drug Dev Ind Pharm.* 41 (2014) 1617–1631. <https://doi.org/10.3109/03639045.2014.976574>.
- [103] M. Li, I. Suriel, J. Vekaria, J. Proske, P. Orbe, M. Armani, R.N. Dave, E. Bilgili, Impact of dispersants on dissolution of itraconazole from drug-loaded, surfactant-free, spray-dried nanocomposites, *Powder Technology.* 339 (2018) 281–295. <https://doi.org/https://doi.org/10.1016/j.powtec.2018.08.014>.
- [104] N. Shetty, H. Park, D. Zemlyanov, S. Mangal, S. Bhujbal, Q. Zhou, Influence of excipients on physical and aerosolization stability of spray dried high-dose powder formulations for inhalation, *Int. J. of Pharmaceutics.* 544 (2018) 222–234. <https://doi.org/https://doi.org/10.1016/j.ijpharm.2018.04.034>.
- [105] A. Torge, P. Grützmacher, F. Mücklich, M. Schneider, The influence of mannitol on morphology and disintegration of spray-dried nano-embedded microparticles, *Europ. J. of Pharm. Sciences.* 104 (2017) 171–179. <https://doi.org/https://doi.org/10.1016/j.ejps.2017.04.003>.
- [106] R.L. Carr, Evaluating flow properties of solids, *Chemical Engineering.* 72 (1965) 163–168.
- [107] R.B. Shah, M.A. Tawakkul, M.A. Khan, Comparative Evaluation of Flow for Pharmaceutical Powders and Granules, *AAPS Pharmscitech.* 9 (2008) 250–258. <https://doi.org/10.1208/s12249-008-9046-8>.
- [108] U.S.P. (USP-NF), (1174) Powder Flow, General Chapter, Rockville, MD, 2020. https://doi.org/https://doi.org/10.31003/USPNF_M99885_01_01.
- [109] A. Lechanteur, B. Evrard, Influence of Composition and Spray-Drying Process Parameters on Carrier-Free DPI Properties and Behaviors in the Lung: A review, *Pharm.* 12 (2020) 55. <https://doi.org/10.3390/pharmaceutics12010055>.
- [110] L. Walter-Levy, Sur les variétés cristallines du D-mannitol, *C. R. Acad. Sci. Paris.* 267 (1968) 1779–82.
- [111] W. Su, J. Liu, H. Wang, C. Li, N. Jia, Thermodynamic study of three anhydrous polymorphs of d-mannitol in different binary solvent mixtures from T = (258.15 to 278.15) K, *J Chem Thermodyn.* 141 (2020) 105680. <https://doi.org/10.1016/j.jct.2019.01.005>.
- [112] S.G. Maas, G. Schaldach, E.M. Littringer, A. Mescher, U.J. Griesser, D.E. Braun, P.E. Walzel, N.A. Urbanetz, The impact of spray drying outlet temperature on the particle morphology of mannitol, *Powder Technology.* 213 (2011) 27–35. <https://doi.org/https://doi.org/10.1016/j.powtec.2011.06.024>.
- [113] I. Atsutoshi, Y. Shuichi, T. Mitsuhide, K. Michiko, Selective production method for D-mannitol alpha-form crystal using spray-drying method, 2016.
- [114] M. Mönckedieck, J. Kamplade, P. Fakner, N.A. Urbanetz, P. Walzel, H. Steckel, R. Scherließ, Spray drying of mannitol carrier particles with defined morphology and flow characteristics for dry

- powder inhalation, *Dry Technol.* 35 (2017) 1843–1857.
<https://doi.org/10.1080/07373937.2017.1281291>.
- [115] B.-M. Kwak, J.E. Lee, J.-H. Ahn, T.-H. Jeon, Laser diffraction particle sizing by wet dispersion method for spray-dried infant formula, *J Food Eng.* 92 (2009) 324–330.
<https://doi.org/10.1016/j.jfoodeng.2008.12.005>.
- [116] A. Baldelli, R.M. Power, R.E.H. Miles, J.P. Reid, R. Vehring, Effect of crystallization kinetics on the properties of spray dried microparticles, *Aerosol Sci Tech.* 50 (2016) 693–704.
<https://doi.org/10.1080/02786826.2016.1177163>.
- [117] C. Duret, N. Wauthoz, T. Sebti, F. Vanderbist, K. Amighi, New inhalation-optimized itraconazole nanoparticle-based dry powders for the treatment of invasive pulmonary aspergillosis, *Int J Nanomed.* 7 (2012) 5475–5489. <https://doi.org/10.2147/ijn.s34091>.
- [118] B.V. Eerdenbrugh, L. Froyen, J.V. Humbeeck, J.A. Martens, P. Augustijns, G.V. den Mooter, Drying of crystalline drug nanosuspensions—The importance of surface hydrophobicity on dissolution behavior upon redispersion, *Europ. J. of Pharm. Sciences.* 35 (2008) 127–135.
<https://doi.org/https://doi.org/10.1016/j.ejps.2008.06.009>.
- [119] K.Y. Wan, J. Weng, S.N. Wong, P.C.L. Kwok, S.F. Chow, A.H.L. Chow, Converting nanosuspension into inhalable and redispersible nanoparticles by combined in-situ thermal gelation and spray drying, *European Journal of Pharmaceutics and Biopharmaceutics.* 149 (2020) 238–247.
<https://doi.org/https://doi.org/10.1016/j.ejpb.2020.02.010>.
- [120] M.A. Boraey, R. Vehring, Diffusion controlled formation of microparticles, *J Aerosol Sci.* 67 (2014) 131–143. <https://doi.org/10.1016/j.jaerosci.2013.10.002>.
- [121] J. Lee, Drug nano- and microparticles processed into solid dosage forms: Physical properties, *J Pharm Sci.* 92 (2003) 2057–2068. <https://doi.org/10.1002/jps.10471>.
- [122] F. Iskandar, L. Gradon, K. Okuyama, Control of the morphology of nanostructured particles prepared by the spray drying of a nanoparticle sol, *J Colloid Interf Sci.* 265 (2003) 296–303.
[https://doi.org/10.1016/s0021-9797\(03\)00519-8](https://doi.org/10.1016/s0021-9797(03)00519-8).
- [123] W.L. Hulse, R.T. Forbes, M.C. Bonner, M. Getrost, The characterization and comparison of spray-dried mannitol samples, *Drug Dev Ind Pharm.* 35 (2009) 712–718.
<https://doi.org/10.1080/03639040802516491>.
- [124] Y.-Y. Lee, J.X. Wu, M. Yang, P.M. Young, F. van den Berg, J. Rantanen, Particle size dependence of polymorphism in spray-dried mannitol, *Europ. J. of Pharm. Sciences.* 44 (2011) 41–48.
<https://doi.org/https://doi.org/10.1016/j.ejps.2011.06.002>.
- [125] A. Buanz, M. Gurung, S. Gaisford, Crystallisation in printed droplets: understanding crystallisation of d-mannitol polymorphs, *Crystengcomm.* 21 (2019) 2212–2219.
<https://doi.org/10.1039/c8ce01780h>.

- [126] K. Brodka-Pfeiffer, Einfluss von Mikronisierungsprozessen auf die physikochemische Stabilität von Pulvern für Inhalationszwecke: Kriterien für die Auswahl von Konditionierungsverfahren, 2003.
- [127] S. Czyz, M. Wewers, J.H. Finke, A. Kwade, B. van Eerdenbrugh, M. Juhnke, H. Bunjes, Spray drying of API nanosuspensions: Importance of drying temperature, type and content of matrix former and particle size for successful formulation and process development, *European Journal of Pharmaceutics and Biopharmaceutics*. 152 (2020) 63–71. <https://doi.org/https://doi.org/10.1016/j.ejpb.2020.04.021>.
- [128] E. Bilgili, M. Rahman, D. Palacios, F. Arevalo, Impact of polymers on the aggregation of wet-milled itraconazole particles and their dissolution from spray-dried nanocomposites, *Advanced Powder Technology*. 29 (2018) 2941–2956. <https://doi.org/https://doi.org/10.1016/j.apt.2018.09.039>.
- [129] K. Yamasaki, P.C.L. Kwok, K. Fukushige, R.K. Prud'homme, H.-K. Chan, Enhanced dissolution of inhalable cyclosporine nano-matrix particles with mannitol as matrix former, *Int. J. of Pharmaceutics*. 420 (2011) 34–42. <https://doi.org/https://doi.org/10.1016/j.ijpharm.2011.08.010>.
- [130] M. Malamatarı, S. Somavarapu, M. Bloxham, G. Buckton, Nanoparticle agglomerates of indomethacin: The role of poloxamers and matrix former on their dissolution and aerosolisation efficiency, *Int. J. of Pharmaceutics*. 495 (2015) 516–526. <https://doi.org/http://dx.doi.org/10.1016/j.ijpharm.2015.09.013>.
- [131] M. Malamatarı, S. Somavarapu, K. Kachrimanis, G. Buckton, K.M.G. Taylor, Preparation of respirable nanoparticle agglomerates of the low melting and ductile drug ibuprofen: Impact of formulation parameters, *Powder Technol.* 308 (2017) 123–134. <https://doi.org/10.1016/j.powtec.2016.12.007>.
- [132] Z. Huang, L. Lin, C. McGoverin, H. Liu, L. Wang, Q. Zhou, M. Lu, C. Wu, Dry powder inhaler formulations of poorly water-soluble itraconazole: A balance between in-vitro dissolution and in-vivo distribution is necessary, *Int. J. of Pharmaceutics*. 551 (2018) 103–110. <https://doi.org/https://doi.org/10.1016/j.ijpharm.2018.09.018>.
- [133] E. Fröhlich, A. Mercuri, S. Wu, S. Salar-Behzadi, Measurements of Deposition, Lung Surface Area and Lung Fluid for Simulation of Inhaled Compounds, *Front Pharmacol.* 7 (2016) 181. <https://doi.org/10.3389/fphar.2016.00181>.
- [134] I. Sibum, P. Hagedoorn, C.O. Botterman, H.W. Frijlink, F. Grasmeijer, Automated Filling Equipment Allows Increase in the Maximum Dose to Be Filled in the Cyclops® High Dose Dry Powder Inhalation Device While Maintaining Dispersibility, *Pharm.* 12 (2020) 645. <https://doi.org/10.3390/pharmaceutics12070645>.
- [135] A. Jüptner, R. Scherließ, Spray Dried Formulations for Inhalation—Meaningful Characterisation of Powder Properties, *Pharm.* 12 (2019) 14. <https://doi.org/10.3390/pharmaceutics12010014>.
- [136] S.B. Tan, J.M. Newton, Powder flowability as an indication of capsule filling performance, *Int J Pharmaceut.* 61 (1990) 145–155. [https://doi.org/10.1016/0378-5173\(90\)90053-7](https://doi.org/10.1016/0378-5173(90)90053-7).

- [137] S. Stegemann, E. Faulhammer, J.T. Pinto, A. Paudel, Focusing on powder processing in Dry Powder Inhalation product development, manufacturing and performance, *Int J Pharmaceut.* 614 (2022) 121445. <https://doi.org/10.1016/j.ijpharm.2021.121445>.
- [138] C. Weiler, *Generierung leicht dispergierbarer Inhalationspulver mittels Sprühtrocknung*, 2008.
- [139] S.C. Das, P.J. Stewart, I.G. Tucker, The respiratory delivery of high dose dry powders, *Int. J. of Pharmaceutics.* 550 (2018) 486–487. <https://doi.org/https://doi.org/10.1016/j.ijpharm.2018.09.014>.
- [140] S. Jafarinejad, K. Gilani, E. Moazeni, M. Ghazi-Khansari, A.R. Najafabadi, N. Mohajel, Development of chitosan-based nanoparticles for pulmonary delivery of itraconazole as dry powder formulation, *Powder Technology.* 222 (2012) 65–70. <https://doi.org/https://doi.org/10.1016/j.powtec.2012.01.045>.
- [141] R. Scherließ, Future of nanomedicines for treating respiratory diseases, *Expert Opin Drug Del.* 16 (2019) 59–68. <https://doi.org/10.1080/17425247.2019.1553955>.
- [142] D.P. Miller, T. Tan, T.E. Tarara, J. Nakamura, R.J. Malcolmson, J.G. Weers, Physical Characterization of Tobramycin Inhalation Powder: I. Rational Design of a Stable Engineered-Particle Formulation for Delivery to the Lungs, *Mol Pharmaceut.* 12 (2015) 2582–2593. <https://doi.org/10.1021/acs.molpharmaceut.5b00147>.
- [143] A.G.-T.G. Administration, Australian Public Assessment Report for Mannitol, Australian Government - Therapeutic Goods Administration, 2011. <https://www.tga.gov.au/sites/default/files/auspar-bronchitol.pdf>.
- [144] M.S. Hassan, R.W.M. Lau, Effect of Particle Shape on Dry Particle Inhalation: Study of Flowability, Aerosolization, and Deposition Properties, *AAPS Pharmscitech.* 10 (2009) 1252. <https://doi.org/10.1208/s12249-009-9313-3>.
- [145] H. Adi, D. Traini, H.-K. Chan, P.M. Young, The Influence of Drug Morphology on Aerosolisation Efficiency of Dry Powder Inhaler Formulations, *Journal of Pharmaceutical Sciences.* 97 (2008) 2780–2788. <https://doi.org/https://doi.org/10.1002/jps.21195>.
- [146] S. Das, I. Larson, P. Young, P. Stewart, Surface energy changes and their relationship with the dispersibility of salmeterol xinafoate powders for inhalation after storage at high RH, *Eur J Pharm Sci.* 38 (2009) 347–354. <https://doi.org/10.1016/j.ejps.2009.08.007>.
- [147] H. Adi, P.M. Young, H.-K. Chan, H. Agus, D. Traini, Co-spray-dried mannitol–ciprofloxacin dry powder inhaler formulation for cystic fibrosis and chronic obstructive pulmonary disease, *Europ. J. of Pharm. Sciences.* 40 (2010) 239–247. <https://doi.org/https://doi.org/10.1016/j.ejps.2010.03.020>.
- [148] K. Brunet, J.-P. Martellosio, F. Tewes, S. Marchand, B. Rammaert, Inhaled Antifungal Agents for Treatment and Prophylaxis of Bronchopulmonary Invasive Mold Infections, *Pharm.* 14 (2022) 641. <https://doi.org/10.3390/pharmaceutics14030641>.
- [149] M. Pozzoli, P. Rogueda, B. Zhu, T. Smith, P.M. Young, D. Traini, F. Sonvico, Dry powder nasal drug delivery: challenges, opportunities and a study of the commercial Teijin Puvlizer Rhinocort

- device and formulation, *Drug Dev Ind Pharm.* 42 (2016) 1–9.
<https://doi.org/10.3109/03639045.2016.1160110>.
- [150] U.S.F.& D. Administration, *Inactive Ingredients in Approved Drug Products*, (2022).
<https://www.accessdata.fda.gov/scripts/cder/iig/index.cfm> (accessed March 13, 2018).
- [151] J. Welch, J. Wallace, A.B. Lansley, C. Roper, Evaluation of the toxicity of sodium dodecyl sulphate (SDS) in the MucilAir™ human airway model in vitro, *Regul Toxicol Pharm.* 125 (2021) 105022. <https://doi.org/10.1016/j.yrtph.2021.105022>.
- [152] ICH, *ICH Q1A (R2) Stability testing of new drug substances and drug products*, (2003).
<https://www.ema.europa.eu/en/ich-q1a-r2-stability-testing-new-drug-substances-drug-products> (accessed May 28, 2022).
- [153] K. Simkova, B. Joost, G. Imanidis, Production of fast-dissolving low-density powders for improved lung deposition by spray drying of a nanosuspension, *European Journal of Pharmaceutics and Biopharmaceutics.* 146 (2020) 19–31.
<https://doi.org/https://doi.org/10.1016/j.ejpb.2019.11.003>.
- [154] F. Buttini, A.G. Balducci, G. Colombo, F. Sonvico, S. Montanari, G. Pisi, A. Rossi, P. Colombo, R. Bettini, Dose administration manoeuvres and patient care in tobramycin dry powder inhalation therapy, *Int J Pharmaceut.* 548 (2018) 182–191. <https://doi.org/10.1016/j.ijpharm.2018.06.006>.
- [155] S. Yeung, D. Traini, D. Lewis, P.M. Young, Dosing challenges in respiratory therapies, *Int J Pharmaceut.* 548 (2018) 659–671. <https://doi.org/10.1016/j.ijpharm.2018.07.007>.
- [156] T. Parumasivam, S.S.Y. Leung, P. Tang, C. Mauro, W. Britton, H.-K. Chan, The Delivery of High-Dose Dry Powder Antibiotics by a Low-Cost Generic Inhaler, *AAPS J.* 19 (2017) 191–202.
<https://doi.org/10.1208/s12248-016-9988-9>.
- [157] C.A. Ruge, A. Bohr, M. Beck-Broichsitter, V. Nicolas, N. Tsapis, E. Fattal, Disintegration of nano-embedded microparticles after deposition on mucus: A mechanistic study, *Colloids and Surfaces B: Biointerfaces.* 139 (2016) 219–227.
<https://doi.org/https://doi.org/10.1016/j.colsurfb.2015.12.017>.

8 Appendix

8.1 Additional figures

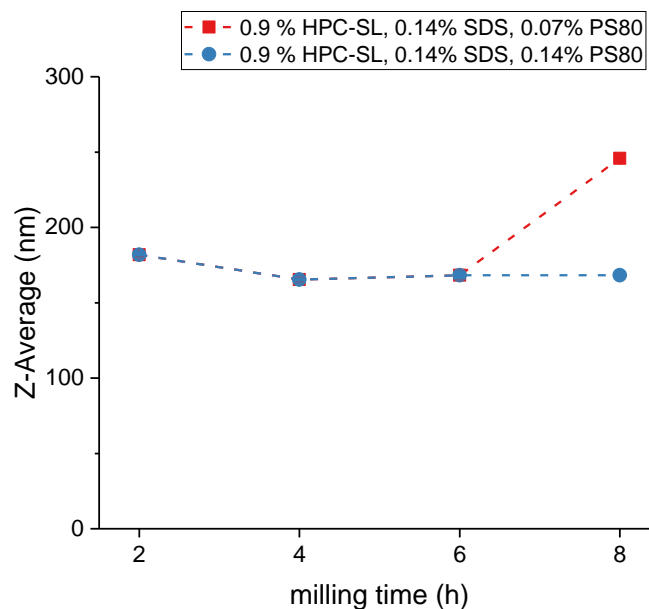


Figure 47: Effect of higher ITZ concentrations (9% w/w throughout 8 h milling) on the particle size in relation to the stabilizer medium. As stabilizers hydroxy propyl cellulose SL (HPC-SL), sodium dodecyl sulfate (SDS) and polysorbate 80 (PS80) were used. Milling was carried out at 4°C with 1500 rpm

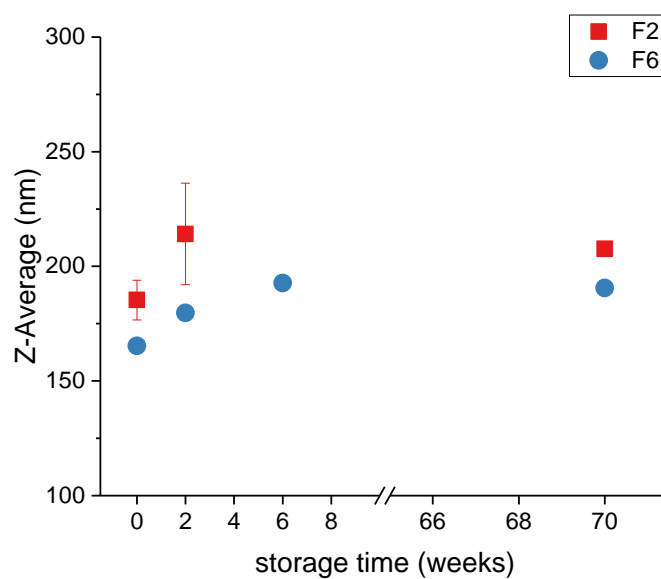


Figure 48: Particle size of formulations F2 and F6 (milled for 3 h) investigated for long-term storage. Milling was carried out at 4°C with 1500 rpm. Values are expressed as mean \pm SD.

8.2 List of Abbreviations and Acronyms

Descriptor	Explanation	Unit
100:0	Nano-in-microparticles, ITZ:MAN ratio 100:0 (w/w)	
25:75	Nano-in-microparticles, ITZ:MAN ratio 25:75 (w/w)	
50:50	Nano-in-microparticles, ITZ:MAN ratio 50:50 (w/w)	
75:25	Nano-in-microparticles, ITZ:MAN ratio 75:25 (w/w)	
ABPA	Allergic bronchopulmonary aspergillosis	
API	Active pharmaceutical ingredient	
AV	Acceptance value (for test of uniformity of dosage units)	
BCS	Biopharmaceutics classification system	
COPD	Chronic obstructive pulmonary disease	
d_{50}	Median geometric diameter obtained by laser diffraction, volume-based	[μm]
d_{ae}	<i>Aerodynamic diameter</i>	[μm]
d_g	<i>Geometric diameter obtained by laser diffraction, volume-based</i>	[μm]
D_i	<i>Diffusion coefficient</i>	
DL	Drug load (API concentration in formulation in % w/w)	
DLS	Dynamic light scattering	
DLVO	Theory according to Derjaguin, Landau, Verwey and Overbeek	
DMSO	Dimethyl sulfoxide	
DoE	Design of experiments	
DPI(s)	Dry powder inhaler(s)	
DSC	Differential scanning calorimetry	
DVS	Dynamic vapor sorption	
ED	Emitted dose (also called delivered dose)	
FPD(s)	Fine particle dose(s) (particles with an aerodynamic diameter < 5 μm)	[mg]

Appendix

FPF(s)	Fine particle fraction(s) (fraction of particles with an aerodynamic diameter < 5 µm)	[%]
GSD	Geometric standard deviation	[-]
H ₂ O 100 °C	Sample: Mannitol particles spray dried at 100°C outlet temperature using water as solvent	
H ₂ O 60 °C	Sample: Mannitol particles spray dried at 60°C outlet temperature using water as solvent	
H ₂ O 80 °C	Sample: Mannitol particles spray dried at 80°C outlet temperature using water as solvent	
HPC-SL	Hydroxypropyl cellulose, type SL	
HPLC	High performance liquid chromatography	
HPMC	Hydroxy propyl methylcellulose	
ICH	International Council for Harmonisation of Technical Requirements for Pharmaceuticals for Human Use	
IPA	Invasive pulmonary aspergillosis	
ITZ	Itraconazole	
JM	Sample: Itraconazole jet-milled	
JM SD	Sample: Itraconazole jet-milled and spray dried using stabilizer medium	
κ	<i>Evaporation constant</i>	
LoD	Loss on drying	
m	<i>mass</i>	[g]
MAN	Mannitol	
Med 100 °C	Sample: Mannitol particles spray dried at 100°C outlet temperature using water + stabilizers as solvent	
Med 60 °C	Sample: Mannitol particles spray dried at 60°C outlet temperature using water as + stabilizers solvent	
Med 80 °C	Sample: Mannitol particles spray dried at 80°C outlet temperature using water as + stabilizers solvent	
MMAD	Mass median aerodynamic diameter	
MOC	Micro orifice collector	
N/A	Not applicable	

NGI	Next generation impactor	
Δp	<i>Pressure drop</i>	[kPa]
PDI	Polydispersity index	[-]
Pe	<i>Peclet number</i>	[-]
Ph. Eur.	European Pharmacopoeia	
pMDI(s)	Pressurized metered dose inhaler(s)	
PP	Polypropylene	
PS80	Polysorbate 80	
ρ_p	<i>Particle density</i>	[g/cm ³]
ρ_o	<i>Bulk density</i>	[g/cm ³]
ρ_f	<i>Tapped density</i>	[g/cm ³]
ρ^*	<i>Unit density (= 1 g/cm³)</i>	[g/cm ³]
Q	<i>Flow rate</i>	[l/min]
R	<i>Intrinsic device resistance</i>	[kPa ^{1/2} /L*min ⁻¹]
rH	Relative humidity	[%]
RPM	Revolutions per minute	
SX	Stage X of the NGI	
SDS	Sodium dodecyl sulfate	
SEM	Scanning electron microscopy	
SIP	Standard induction port	
SL/min	Standard liters per minute (obtained at standard conditions)	
T_{out}	Outlet temperature	[°C]
V_f	<i>Tapped volume</i>	[ml]
V_o	<i>Bulk volume</i>	[ml]
χ	<i>Dynamic shape factor</i>	[-]

Appendix

XRPD	X-ray powder diffraction	
Z-AV	Z-average (particle size obtained by dynamic light scattering)	[nm]

8.3 List of Figures

- Figure 1: Schematic illustration of examples of (engineered) dry powder particles. ■ API, ■ matrix former..... 3
- Figure 2: Schematic illustration of the respiratory tract, the aerodynamic diameters (d_{ae}) and the related main impaction mechanisms. Modified from [30]..... 5
- Figure 3: Classification of DPIs (dry powder inhalers) with regard to number of doses and dosing principle..... 7
- Figure 4: Schematic illustration of a laboratory-scale spray dryer. The feed solution/suspension (3) is pumped with a peristaltic pump (4) into the nozzle (2). The feed liquid is atomized into droplets by the nozzle gas (6). The droplets are dried in the hot gas stream (1) in the drying chamber (5). The dried particles follow the gas stream into the connection (9) of drying chamber and cyclone (10). The particles are then collected in a glass (11), whereas the process gas stream with residual small particles enters the connection (12) to the exhaust filter. Particles, which are too large to follow the process gas stream will get deposited in a glass below the drying chamber (7). The outlet temperature is measured (8) in the connection between the drying chamber and the cyclone..... 11
- Figure 5: HandiHaler® closed (A) and opened (B). This capsule-based device consists of a mouthpiece (1), a capsule-piercing element (2) and a capsule compartment (3). It was developed by Boehringer Ingelheim. © Boehringer Ingelheim 16
- Figure 6: Multi dose inhalation device developed by Vectura Group Ltd. It consists of a mouthpiece (1), a blister piercing element (2) and the blister cavity (3). After inhalation the empty blister cavities are released (4). The used blister-based device is licensed to Novartis and marketed as Forspiro® (© Boehringer Ingelheim)..... 17
- Figure 7: Schematic illustration of nano milling with the ZentriMix. The rotor enables both a rotation around the longitudinal axis (big black arrow) and a secondary rotation around each vial holder (small black arrows). The combined dual rotation facilitates the creation of a high kinetic energy with four vials being milled at the same time. 18
- Figure 8: BI drum filler. From right to left: Foil holder (1), blister former (2), filling element (3), sealing element (4), cutting element (5). © Boehringer Ingelheim..... 22
- Figure 9: Filling element of in-house made blister machine in detail. (1) Powder reservoir, (2) Powder feeding impeller, (3) drum with powder cavities, (4) blister foil with preformed cavities. Image was created with SolidWorks® 22
- Figure 10: Experimental set-up for the assessment of fine particles according to the Ph. Eur. The vacuum pump is connected by vacuum tubing (1) with the impactor. A timer controls the two-way solenoid valve (2) which is attached to the flow control valve

(4) with a metal coupling (3). Pressure before and after the flow control valve is determined with two pressure gauges (5). The scheme was modified from [80]	28
Figure 11: NGI (Apparatus E) for the assessment of fine particles according to the Ph. Eur [80]. The lid consists of a steel body with nozzles of a defined number and diameter (e.g., Stage 1 nozzle (1) or micro-orifice collector (MOC) (4)) and interstage pathways. The bottom frame comprises a tray with removable impaction cups (e.g., 2) and a connection to the vacuum pump (3). © Boehringer Ingelheim	28
Figure 12: Z-average after 8 h of milling with different stabilizer solutions. Composition is given in % (w/w), and HPC-SL concentration was kept constant at 0.9%. Milling was carried out at 4°C with 1500 rpm and milling beads sized 0.3 – 0.4 mm. Hatched area: No stable nanosuspension was obtained. Value ranges are given as mean of three measurements.....	33
Figure 13: Impact of milling speed on the particle size of the ITZ nanosuspensions. Values are given as mean ± SD, n = 3.....	36
Figure 14: Effect of milling bead size on the ITZ particle size. Values are expressed as mean ± SD, n = 3. Milling was carried out at 4°C with 1500 rpm. *Bead size 0.1 - 0.2 mm: stabilizer amount had to be changed to 0.9 % HPC-SL, 0.28 % PS and 0.28 % SDS	38
Figure 15: Effect of milling bead size on the polydispersity index (PDI) of ITZ particles (relating to F6). Values are expressed as mean ± SD, n = 3. Milling was carried out at 4°C with 1500 rpm. *Bead size 0.1 - 0.2 mm: stabilizer concentration had to be changed to 0.9% (w/w) HPC-SL, 0.28% (w/w) PS80 and 0.28% (w/w) SDS. Data are shown in two figures (A & B) for better readability.....	39
Figure 16: Z-Average (A), PDI (B) and zeta potential (C) of F2 (red squares) and F6 (blue dots) in relation to the milling time. Milling was carried out at 4°C with 1500 rpm and milling beads sized 0.3 – 0.4 mm. Values expressed as mean ± SD, n = 3.....	41
Figure 17: XRPD pattern of F2 in relation to grinding time. Milling was carried out at 4°C with 1500 rpm and milling beads sized 0.3 – 0.4 mm. ITZ Start: starting material of ITZ. Plots are shifted for a better illustration.....	43
Figure 18: XRPD pattern of F6 in relation to grinding time. Milling was carried out at 4°C with 1500 rpm and milling beads sized 0.3 – 0.4 mm. ITZ Start: starting material of ITZ. Plots are shifted for a better illustration.....	44
Figure 19: DSC-thermograms of F2 ITZ nanosuspension. Milling was carried out at 4°C with 1500 rpm and milling beads sized 0.3 – 0.4 mm. ITZ Start: starting material of ITZ. Event marked with arrow 1: glass transition and relaxation, marked with arrow 2: recrystallization. Plots are shifted for a better illustration.....	45
Figure 20: DSC-thermograms of F6 ITZ nanosuspension. Milling was carried out at 4°C with 1500 rpm and milling beads sized 0.3 – 0.4 mm. ITZ Start: starting material of ITZ. Plots are shifted for a better illustration.....	46

Figure 21: SEM images of F2 ITZ nanosuspension after different milling periods (indicated in the left upper corner of each image). Milling was carried out at 4°C with 1500 rpm and milling beads sized 0.3 – 0.4 mm.	47
Figure 22: SEM images of F2 ITZ nanosuspension after different milling periods (indicated in the left upper corner of each image). Milling was carried out at 4°C with 1500 rpm and milling beads sized 0.3 – 0.4 mm.	48
Figure 23: Particle sizes of formulation F2 stored at refrigerated conditions (A) and at room temperature (B) for different storage periods. Values are expressed as mean ± SD, n = 3. Milling was carried out at 4°C with 1500 rpm and milling beads sized 0.3 – 0.4 mm.	49
Figure 24: Particle sizes of formulation F6 stored at refrigerated conditions (A) and at room temperature (B) for different storage periods. Values are expressed as mean ± SD, n = 3. Milling was carried out at 4°C with 1500 rpm and milling beads sized 0.3 – 0.4 mm.	50
Figure 25: XRPD patterns of F2 ITZ nanosuspension after storage for storage periods of 0, 7, and 14 days at refrigerated conditions. Milling was carried out at 4°C with 1500 rpm and milling beads sized 0.3 – 0.4 mm. Milling time is indicated in the upper left corner of each figure. Marked area: Increase in peak intensity. Plots are shifted for better a illustration.	51
Figure 26: XRPD patterns of the F6 ITZ nanosuspension after storage for storage periods of 0, 7, and 14 days at refrigerated conditions. Milling was carried out at 4°C with 1500 rpm and milling beads sized 0.3 – 0.4 mm. Milling time is indicated in the upper left corner of each figure. Plots are shifted for a better illustration.	52
Figure 27: DSC thermograms of F2 ITZ nanosuspension after storage at refrigerated conditions for storage periods of 0, 7, and 14 days. Milling was carried out at 4°C with 1500 rpm and milling beads sized 0.3 – 0.4 mm. Milling time is indicated in the lower left corner of each figure. Event marked with arrow 1: recrystallization, event marked with arrow 2: glass transition. Plots are shifted for a better illustration.	53
Figure 28: DSC thermograms of F6 ITZ nanosuspension after storage at refrigerated conditions for storage periods of 0, 7, and 14 days. Milling was carried out at 4°C with 1500 rpm and milling beads sized 0.3 – 0.4 mm. Milling time is indicated in the lower left corner of each figure. Plots are shifted for a better illustration.	54
Figure 29: Droplet size of mannitol dissolved in stabilizer medium depending on feed rate and nozzle gas flow. Values are given as mean ± SD (n = 3), measured by Helos H1411.	58
Figure 30: Spray drying results of MAN obtained from water (H ₂ O) and water with stabilizers (Med). The d ₅₀ at 0.1 bar dispersion pressure (A), the LoD (B) and yield (C) are displayed. Values are given as mean ± SD, if applicable.	60

Figure 31: XRPD patterns of mannitol powders spray dried at different outlet temperatures, (A) using water, (B) using stabilizer medium. MAN α : α -modification of mannitol. MAN β : β -modification of mannitol MAN δ : δ -modification of mannitol. Plots are shifted for better illustration.	62
Figure 32: SEM images of MAN samples spray dried at different outlet temperatures without (sample named H ₂ O, first row) and with stabilizers (sample named Med, second row).....	63
Figure 33: Impact of outlet temperature and stabilizers on the dispersibility of spray dried MAN particles determined by pressure titration. The mean particle size is displayed as a function of the dispersion pressure. Values are given as mean \pm SD (n = 3).....	65
Figure 34: SEM images of nano-in-microparticles, the jet-milled sample (JM) and the jet-milled and spray dried sample (JM SD). Number in sample name describes the ratio of ITZ:MAN [%w/w].....	69
Figure 35: SEM images of the nano-in-microparticles, the jet-milled sample (JM) and the jet-milled and spray dried sample (JM SD). Number in sample name describes the ratio of ITZ:MAN [%w/w].....	70
Figure 36: XRPD patterns of the powder samples. Sample name is indicated at the top of each figure. Number in sample name describes the ratio of ITZ:MAN [%w/w]. Plots are shifted for better illustration. JM: jet-milled, JM SD: je-milled and spray dried.....	72
Figure 37: Adsorption (A) and desorption (D) curves for the powder samples and starting materials measured by DVS. Sample name is indicated on the top of each plot. JM: jet-milled, JM SD: jet-milled and spray dried.	74
Figure 38: Adsorption (A) and desorption (D) curves for the nano-in-microparticles measured by DVS. Sample name is indicated on the top of each plot (number: ratio of ITZ:MAN [%w/w]).....	75
Figure 39: XRPD patterns of the powder samples before and after one DVS cycle. Plots are shifted for better illustration. Number in sample name describes the ratio of ITZ:MAN [%w/w].	76
Figure 40: Mean particle size (d ₅₀) of ITZ powder samples in relation to the dispersion pressure (pressure titration). Number in sample name describes the ratio of ITZ:MAN [%w/w]. JM: jet-milled, JM SD: jet-milled and spray dried. Values are expressed as mean \pm SD (n = 3).....	77
Figure 41: Particle size (A) and PDI (B) of the reconstituted nano-in-microparticles in relation to the stirring time. Dashed line indicates value before spray drying (nanosuspension). Values are expressed as mean \pm SD, n =3. Sample names indicate the ITZ:MAN ratio (% w/w).	79

- Figure 42: Comparison of FPD (red) and FPF (blue) for the HandiHaler® (A) and the GyroHaler® (B). Values are given as mean \pm SD. Number in sample name describes the ratio of ITZ:MAN [%w/w]. JM: jet-milled, JM SD: jet-milled and spray dried. 85
- Figure 43: Results of the impaction measurements with the GyroHaler®. Values are expressed as mean \pm SD, n = 3. Mass is related to the recovered (=emitted from the device) mass of the NGI including SIP and preseparator. Number in sample name describes the ratio of ITZ:MAN [%w/w]. JM: jet-milled, JM SD: jet-milled and spray dried. 87
- Figure 44: Results of the impaction measurements with the HandiHaler®. Values are expressed as mean \pm SD, n = 3. Mass is related to the recovered (=emitted from the device) mass of the NGI including SIP and preseparator. Number in sample name describes the ratio of ITZ:MAN [%w/w]. JM: jet-milled, JM SD: jet-milled and spray dried..... 88
- Figure 45: Overview of calculated residual ITZ dose in the device and emitted (= recovered from NGI) ITZ mass for the HandiHaler® (A) and the GyroHaler® (B). Number in sample name describes the ratio of ITZ:MAN [%w/w]. JM: jet-milled, JM SD: jet-milled and spray dried. The total dose of ITZ varies dependent on the drug loading of the filled 13.5 mg powder formulation..... 89
- Figure 46: Results of the impaction measurements with the HandiHaler® and the GyroHaler®. Values are expressed as mean \pm SD, n = 3. Mass is related to the recovered mass of the NGI stages (S1-MOC). Number in sample name describes the ratio of ITZ:MAN [%w/w]. JM: jet-milled, JM SD: jet-milled and spray dried. 90
- Figure 47: Effect of higher ITZ concentrations (9% w/w throughout 8 h milling) on the particle size in relation to the stabilizer medium. As stabilizers hydroxy propyl cellulose SL (HPC-SL), sodium dodecyl sulfate (SDS) and polysorbate 80 (PS80) were used. Milling was carried out at 4°C with 1500 rpm..... 116
- Figure 48: Particle size of formulations F2 and F6 (milled for 3 h) investigated for long-term storage. Milling was carried out at 4°C with 1500 rpm. Values are expressed as mean \pm SD..... 116

8.4 List of Tables

Table 1:	Overview of used API and excipients. BCS: Biopharmaceutics classification system	15
Table 2:	Overview of the parameters during evaluation of the milling process	19
Table 3:	Overview of the spray drying parameters used for process evaluation and for the manufacturing of engineered ITZ particles. Nozzle gas flow rate is given in standard liters per minute (SL/min, flow rate at standard conditions for pressure and temperature: 1 bar and 0°C).....	20
Table 4:	Overview of samples with regard to preparation method and ITZ:MAN ratio [% w/w]	21
Table 5:	Cut-off diameters for the devices at the respective flow rates for 4 kPa pressure drop.....	29
Table 6:	Overview of the parameters during evaluation of the milling process	31
Table 7:	Input variables and response parameters of the statistical evaluation of the stabilizer concentrations after 8 h of milling. HPC-SL concentration was kept constant in all experiments (0.9% (w/w)).....	32
Table 8:	Summary of fit for the applied model. R ² : measure of fit, Q ² : estimation of precision for the prediction.....	34
Table 9:	Overview of the bead diameters and theoretical number of 5 g beads, assuming a bead density of 6 g/cm ³ and a bead volume 0.83 cm ³	37
Table 10:	Overview of the spray drying parameters used for process evaluation. Nozzle gas flow rate is given in standard liters per minute (SL/min, flow rate at standard conditions for pressure and temperature: 1 bar and 0°C).....	57
Table 11:	Overview of the physicochemical properties of the generated MAN particles. Values are given as mean ± SD. Med: H ₂ O + stabilizers (simulating stabilizer medium for ITZ nanosuspension)	59
Table 12:	Overview of ITZ samples with regard to preparation method. Number in sample name indicates the ITZ:MAN ratio [% w/w]. JM: jet-milled, JM SD: jet-milled and spray dried.....	67
Table 13:	Characterization results of the nano-in-microparticles, in comparison sample JM SD (jet-milled and spray dried) and sample JM (jet-milled). Number in sample name describes the ratio of ITZ:MAN [%w/w]. Values are expressed as mean ± SD, if applicable.....	68
Table 14:	Physicochemical properties of nano-in-microparticles, sample JM SD and sample JM. Number in the sample name indicates the ratio of ITZ:MAN [% w/w]. Samples JM and JM SD (marked with *) were filled manually. Values are expressed as mean ± SD.....	83

-
- Table 15: Results of the aerodynamic assessment of the formulations in relation to the device. Values are expressed as mean \pm SD, n = 3. Formulation JM and JM SD (marked with *) were filled manually. Number in sample name describes the ratio of ITZ:MAN [%w/w]. JM: jet-milled, JM SD: jet-milled and spray dried..... 86
- Table 16: Performance criteria and rating for the ITZ dry powder formulations. Number in sample name describes the ratio of ITZ:MAN [%w/w]. JM: jet-milled, JM SD: jet-milled and spray dried. N/A: not applicable. Color coding: ■ critical issue, ■ challenge, ■ uncritical 96

9 Acknowledgements

This work was conducted under the supervision of Prof. Dr. Karl G. Wagner at the Department of Pharmaceutical Technology, Rheinische Friedrich-Wilhelms-Universität Bonn, Germany. Practical work has been performed at Boehringer Ingelheim Pharma GmbH & Co. KG, Biberach an der Riss, Germany under the supervision of Dr. Georg Böck.

I would like to express my gratitude to my supervising professor Karl Wagner, for giving me the opportunity to take over this project of fascinating and challenging topic. Thank you for the valuable guidance, consistent support and scientific discussions. Also, I would like to thank Georg Böck, for providing me the opportunity to work on this topic, for supervision and the appreciated input. The scientific discussions providing new perspectives were very helpful. I would like to thank Herbert Wachtel, for the co-supervision at BI, the appreciated advice any time and for preparing the review. A big thank you to Kai Berkenfeld for having a sympathetic ear any time, for interesting scientific discussions, brainstorming and for the proof-read. I would also like to thank Kerstin Schäfer for the constant support and unlimited motivation. Thank you as well for the possibility to continue and finalize this PhD thesis as well as for proof-reading of the manuscript.

I would like to thank my colleagues from the group *Liquids and Early Development*, especially Olaf Behrend, Verena Bialecki, Sebastian Kauschka, Birgit Luckner, Kathrin Schlanser and Holger Weil: thanks a lot for good discussions, the excellent explanations and constantly helping me with question regarding lab work. Thank you also for the time we spent together, not only in the lab. I wish to thank Ingo Presser for giving me the possibility to stay in the group LED and for the great support (not only regarding sweets). I would like to thank Andree Jung for his support with the drum filler and the helpful talks and discussions as well as the former *RDD department*, especially Claudius Weiler, for the supportive discussions and the valuable input. Also, thanks to my intern Judith Möller for the contribution and excellent support in the lab. A big thank you to the whole team from the BI workshop, especially Robert Schüller and Marco Kasack for their great support whenever a new construction was necessary or something needed to be repaired, and Wolfgang Schwarzkopf for his support concerning calibration and technical discussions. Furthermore, I would like to thank the CMC group from *Drug Discovery Sciences* for support in the lab and especially Ralf Dukeck and Ulrike Werthmann, for the help regarding solid-state characterization and vapor sorption. Thanks to the team from the lab LPA1 in *Analytical Development*, for the unlimited support in HPLC analysis and troubleshooting.

Thank you to many other people for supporting me and facilitating everyday work, especially Teresa Bluhmki, Judith Menth, Katrin Schmid, Elena Stiller, Patrick Strack, Eduard Trenkenschuh and Ines Truebenbach.

I would like to thank Thilo Faber, for the support in SEM measurements as well as the whole research group in Bonn, for interesting scientific discussions, for the support whenever I was in Bonn and the great time we had during conferences.

Finally, I would like to express my gratitude to my friends, who always supported and encouraged me, and my family, especially my mother, who constantly supported me not only throughout the last years.